YOUNG PLANETARY NEBULAE: HUBBLE SPACE TELESCOPE IMAGING AND A NEW MORPHOLOGICAL CLASSIFICATION SYSTEM

Raghvendra Sahai[1], Mark Morris[2], Gregory Villar[3]

arXiv:1101.2214v1 [astro-ph.GA] 11 Jan 2011

[1]Jet Propulsion Laboratory, MS 183-900, California Institute of Technology, Pasadena, CA 91109

[2]Division of Astronomy, Department of Physics and Astrophysics, UCLA, Los Angeles, CA 90095

[3]Cal Poly, Pomona

ABSTRACT

Using Hubble Space Telescope images of 119 young planetary nebulae, most of which have not previously been published, we have devised a comprehensive morphological classification system for these objects. This system generalizes a recently devised system for pre-planetary nebulae, which are the immediate progenitors of planetary nebulae (PNs). Unlike previous classification studies, we have focussed primarily on young PNs rather than all PNs, because the former best show the influences or symmetries imposed on them by the dominant physical processes operating at the first and primary stage of the shaping process. Older PNs develop instabilities, interact with the ambient interstellar medium, and are subject to the passage of photoionization fronts, all of which obscure the underlying symmetries and geometries imposed early on. Our classification system is designed to suffer minimal prejudice regarding the underlying physical causes of the different shapes and structures seen in our PN sample, however, in many cases, physical causes are readily suggested by the geometry, along with the kinematics that have been measured in some systems. Secondary characteristics in our system such as ansae indicate the impact of a jet upon a slower-moving, prior wind; a waist is the signature of a strong equatorial concentration of matter, whether it be outflowing or in a bound Keplerian disk, and point symmetry indicates a secular trend, presumably precession, in the orientation of the central driver of a rapid, collimated outflow. [**The quality of the figures as it appears in the arXiv pdf output is not up-to-par; the full ms with high-quality figures is available by anonymous FTP at ftp://ftp.astro.ucla.edu/pub/morris/AJ-360163-sahai.pdf**].

Subject headings: planetary nebulae, stars: AGB and post–AGB, stars: mass–loss,

circumstellar matter

1. Introduction

Although preplanetary nebulae (PPNs) & planetary nebulae (PNs) evolve from initially spherically–symmetric mass-loss envelopes around AGB stars, modern ground-based imaging surveys have shown that the vast majority of the former deviate strongly from spherical symmetry (e.g., Schwarz, Corradi & Melnick 1992, Manchado et al. 1996a). In a morphologically unbiased survey of young PNs with the Hubble Space Telescope (HST), Sahai & Trauger (1998, ST98) found no round objects, but a variety of bipolar and multipolar morphologies. The significant changes in the circumstellar envelope (CSE) morphology during the evolutionary transition from the AGB to the post-AGB (pAGB) phase require a primary physical agent or agents which can break the spherical symmetry of the radiatively-driven, dusty mass-loss phase. In the "generalised interacting-stellar-winds" (GISW) model, the AGB CSE is assumed to be equatorially dense, and the expansion of a fast ($> 1000\,\mathrm{km\ s^{-1}}$) isotropic wind from the PN central star produces an aspherical PN (Balick 1987). Hydrodynamic simulations based on this model could reproduce a variety of axisymmetric shapes (e.g., review by Balick & Frank 2002). However, Soker (1997, 1990) pointed out that the GISW model could not explain the presence of point symmetry or collimated flows and ansae in PNs. Jet-like outflows were first used to explain bipolar morphology in a small sample of nebulae around evolved stars (Morris 1987, 1990), and the presence of ansae in PNs (Soker 1990). Faced with the complexity, organization and frequent presence of point-symmetry in the morphologies of their survey PNs, ST98 proposed that the primary agent for breaking spherical symmetry is a jet or collimated, fast wind (CFW) operating during the early post-AGB or late AGB evolutionary phase. The CFWs are likely to be episodic, and either change their directionality (i.e., wobbling of axis, or precession) or have multiple components operating in different directions (quasi)simultaneously (Sahai 2004). In the ST98 model, primary shaping begins *prior* to the PN phase, and the variety of PN shapes and structure depends in detail on the CFW characteristics (direction, strength,

opening angle, temporal history).

Direct evidence for CFWs during the pre-PN phase has come from sensitive molecular line observations which reveal the presence of very fast (few$\times$100 km s^{-1}) molecular outflows in PPNs and a few very late AGB stars, with huge momentum-excesses showing that these winds cannot be radiatively driven (e.g., Bujarrabal et al. 2001, Sahai et al. 2006). Using STIS/HST, a carbon star, V Hya, has been "caught in the act" of ejecting a very fast (250 km s^{-1}), highly collimated blobby outflow (Sahai et al. 2003a). Strong support for the ST98 model was recently provided by a (morphologically) unbiased HST imaging survey of young PPNs which shows very close similarities in morphology between these objects and young PNs (Sahai et al. 2007a: SMSC07). If the ST98 model is correct, then the question arises: what is the engine for producing CFW's? If point-symmetric shapes result from the flow collimator precessing or becoming unstable, then what causes the destabilization? Can CFW's be produced by single stars or is a binary companion essential? Single-star models have invoked stellar rotation, strong magnetic fields, or both (e.g., Garcia-Segura et al 1999, Blackman et al. 2001), and binary models have invoked the angular momentum and/or the gravitational influence of a companion (e.g., Morris 1981, 1987, Soker & Livio 1994, Livio & Pringle 1997). Yet, in spite of vigorous debate (e.g., Bujarrabal et al. 2000), no consensus has yet emerged even as to which of the above two broad classes of models is correct (Balick & Frank 2002)!

Morphological classification schemes can play an important role in constraining the physical mechanism or mechanisms that influence the mass loss process. Several PN classification schemes have been presented previously. The major themes of the earliest classifications were based on whether objects were round or elliptical (Zuckerman & Aller 1986). These were refined with the inclusion of bipolar objects and recognition of objects with point symmetry. The most detailed of such schemes has been presented in papers

by Schwarz et al. (1992), Schwarz, Corradi & Stanghellini (1993: SCS93), and Corradi & Schwarz (1995: CS95), based on a sample of 400 objects, with four morphological classes: elliptical (includes round objects), bipolar, point-symmetrical, and irregular. Manchado et al. (1996a: Metal96) have published an atlas of 243 PNs (non-refereed), and presented a morphological classification which is similar to the one described by CS95.

However, all of these earlier schemes are based on ground-based imaging, which gives a typical angular resolution of $\gtrsim 1''$. This resolution precludes recognition of the important morphological traits of most PNs, especially if they are young and therefore physically small. But even for larger and well-resolved objects, a major difficulty arises due to the typical brightness distribution of a bipolar or multipolar PN – such PNs have waists[1] that are very bright, compared to their extended lobes, and the convolution of such a distribution with a seeing Gaussian function whose size is comparable to the size of the waist, can result in a shape which looks roughly elliptical. But profiting from the capabilities of HST, several PN surveys have been carried out, revealing the structures of PNs with unprecedented detail – these cannot be adequately described by the previous classification schemes. Now is an appropriate time for undertaking a new classification scheme that is more detailed, inclusive, and precise than the previous ones, and that can best elucidate the predominant physical processes that contribute to the observed morphologies.

In this paper, we propose a comprehensive morphological classification system for these objects, based on such a system for PPNs devised using their unbiased HST imaging survey of the latter (SMSC07). SMSC07 found a wide variety of morphologies in PPNs, qualitatively similar to those found for young PNs, which is physically intuitive, since young PNs represent the immediate evolutionary phase after the PPN phase. We have

---

[1]an equatorially-flattened central region separating extended lobes oriented near/along a polar axis

therefore extended the SMSC07 PPN classification system to *young* PNs (for an operational definition of "young PNs", see § 2). Unlike previous classification studies, we have focussed primarily on young PNs rather than all PNs, because the former best show the influences or symmetries imposed on them by the dominant physical processes operating at an earlier stage of the shaping process. Older PNs lose these characteristics due to the continued operation of the very fast central star wind and photoionization, and associated dynamical instabilities. Further, interaction with the ISM becomes important for old PNs, and can introduce a new set of morphological features in these objects (Dgani & Soker 1998). We show that the morphological system for PPNs can be adapted for young PNs directly, but with modifications and extensions.

The plan of our paper is as follows. In § 2, we summarise the selection criteria of our sample, and the various HST surveys and other GO programs from which the images have been taken; in § 3, we describe the primary classes (§ 3.1), the secondary characteristics (§ 3.2), the determination of nebular expansion ages (§ 3.3), classification statistics (§ 3.4), the limitations imposed by imaging resolution, sensitivity and nebular orientation effects (§ 3.6, application of our classification scheme to a new PN sample(§ 3.5), and in § 4, we conclude with a discussion on how our classification scheme is relevant for understanding the formation and shaping of planetary nebulae.

2. Observations

The objects included in this work mostly come from several surveys with HST/WFPC2, most of them fitting the selection criterion of ST98, namely that the [OIII]λ5007/Hα

flux ratio, R_{exc}, be less than about unity[2], used to select young PNs. ST98 argue that R_{exc} is expected to be low in young PNs because (1) the central stars have low effective temperatures (25,000-40,000 K), resulting in a low state of nebular excitation and therefore a low [OIII] flux for the bulk of the nebular gas, and (2) young PNs are compact, with large dust optical depths towards their central regions, resulting in a large selective extinction of the shorter wavelength [OIII] line compared with Hα, since [OIII] is more centrally distributed.

Two of the major surveys used in our study, GO 6353 and 8345, (PI: Sahai) were specifically carried out using $R_{exc} \leq 1$ as the selection criterion, with the goal of studying young PN morphologies. The third major survey from which we have selected young PNs meeting the ST98 criterion is GO 9356 (PI: A. Zijlstra), which covered Galactic Bulge PNs. Smaller numbers of objects which fit the ST98 criterion were taken from GTO 6221 (PI: J. Trauger), GO 8307 (PI: S. Kwok) and GO 6347 (PI: K. Borkowski). For five objects (PNG051.5+00.2, PNG061.3+03.6, PNG067.9-002.2, PNG110.1+01.9, PNG332.9-09.9), that were imaged as part of SNAPshot surveys for PPNs (GO 9463 & GO 10536, PI: Sahai), we used the broad-band filter images (at $0.6\,\mu$m and $0.8\,\mu$m) available. We supplemented our sample further with additional objects as follows (i) 1 PN, with R_{exc} formally larger than, but within measurement errors, not significantly different from unity, and (ii) 23 PNs with $R_{exc} > 1$ (generally small-sized, and therefore likely to be young as confirmed by our age estimates, see § 3.3).

Most of these images were obtained in HST's SNAPshot mode, with relatively modest integration times. The total number of objects that are included in this study is 119. A log of the observations is provided in Table 1. The objects in the table are listed in order

---

[2]ST98 use $R_{exc} < 1/1.5$; we have relaxed this a bit, $R_{exc} \leq 1$, in order to include a larger PN sample

of increasing galactic longitude (first number in the PK or PNG designation); when the longitude is the same, then in order of decreasing galactic latitude (second number including sign, in the PK or PNG designation). The table first lists all objects with $R_{exc} \leq 1$ (from PK000+17D1 to PNG359.2+04.7) followed by all objects where this ratio is greater than unity (Table 1). The last column in the table lists the name of the dataset in the HST archive.

A significant fraction of an ongoing new large SNAPshot survey of PNs with the WFC3/HST instrument (GO 11657, PI: Stanghellini) has recently been completely and the results are in the public domain. This survey utilises one narrow-band filter (F502N, covering the [OIII]λ5007 line), and 3 broad band filters (F200LP, F350LP, and F814W). Inspection of the images from this survey shows that the F200LP and F350LP bandpasses, which are extremely wide, and cover all major nebular emission lines, including [OIII], [NII] and Hα, show the morphology most sensitively. We use the images from this survey to demonstrate that our new morphological classification scheme is comprehensive, as it can adequately describe all the morphologies seen so far in this survey.

All images discussed in this paper which were taken with WFPC2 were downloaded from the HST archive of pipeline-calibrated images maintained at the Canadian Astronomy Data Centre (CADC). The images taken with ACS or WFC3 are pipeline-calibrated images downloaded from the StScI/MAST archive.

3. Results

We present the images of all the objects in our sample, with the exception of MyCn 18 (PNG307.5−04.9)[3], in Figs. 1–116. For most of our objects, we have used the Hα (F656N)

---

[3]images in Sahai et al. (1999)

images, since these are best suited to showing the overall nebular structure. In a few cases, Hα images are not available so [NII] (F658N) images have been used. A comparison of the morphologies seen in Hα and [NII] images, when both are available, shows that there is very little difference between these in determining their morphological classifications. For the 4 objects imaged in the GO 9463 & GO 10536 programs, we only have images in two broad-band filters (i.e., taken with either the F435W & F606W, or the F606W & F814 filters). With the exception of one of these (PNG332.9-09.9, in which the F606W image is a relatively short exposure one and so the F435W image is used), we present the F606W images, since this filter includes the Hα line, which most likely represents the dominant contribution to the emission seen in the images. For the PNs imaged in emission-lines, the intensity is proportional to the square of the density, hence the dynamic range is quite large. Therefore, in order to show the nebular structure optimally, we have used a log-stretch black-and-white image in reverse grey-scale, as well as a false-color one in which the intensity has been processed in order to enhance sharp features[4]. For the 4 PNs observed in broad-band filters, the log-stretch black-and-white images show all features of the nebulae adequately, hence only these are shown. All figures and tabulated results form this paper will be made available to the community via the Vizier service of the Centre de Donnes astronomiques de Strasbourg (CDS).

3.1. Primary Classes

The PPN classification system of SMSC07 consisted of 4 primary classes based on the overall nebular shape, and several categories of secondary characteristics related to specific

---

[4]The processed image, $Im_P = Im_O/(Im_O + 0.04 Im_S)$, where Im_O is the original image, and Im_S is obtained by smoothing Im_O, as in ST98, Fig. 1

properties of the lobes, waist, and haloes, and the presence of point-symmetry. This scheme is summarised in Table 2 (non-italicised text). The four existing primary classes, and the ones that we extend to PNs as well, are: B (bipolar), M (multipolar), E (elongated), and I (irregular). The B class (illustrated for PNs in Figs. 1–30) represents objects which show two primary, diametrically opposed lobes, centered on the central star or its expected location. The pair of lobes must have a "pinched in" shape in the region around the center from where they emanate, and/or the lobes should be visible on both sides of a minimum-light-intensity central region (due to an obscuring dust lane). The M class (Figs. 31–51) represents objects having two or more primary lobe pairs whose axes are not aligned. The E class (Figs. 52–86) is simply one in which objects are elongated along a specific axis, i.e., are not round. The I class (Fig. 87–93) represents objects in which extended circumstellar structure can be seen, but where no obvious lobe or shell-like structures can be identified, and which therefore do not fit in any of the previous categories. As the name implies, class-I objects usually do not display any obvious geometrical symmetry such as axial or point-symmetry.

We extend the SMSC07 system to young PNs, by adding new primary classes as well as secondary characteristics (italicised text in Table 2). An additional three primary classes have been added. The first is R (Figs. 94–97), which describes round objects. The maximum asymmetry for an object to be classified as R (rather than E) is $< 10\%$, i.e., the widest extent of the object should be a factor < 1.1 times its average extent. Round objects are rare: of a total of 119 PNs, we only find 4. Note that in the PPN study, SMSC07 did not find a single round object. The second is L (Figs. 98–107), which describes objects having collimated lobes, but which show no constriction in the central, waist region – i.e., the lobes are not pinched-in towards the waist region, which is a requirement for being classified as B, so we do not include them in the B class even though they may be closely related (see §4.1). In order for an object to have an L, rather than an E classification, we require the collimation factor (defined as the ratio of the total tip-to-tip extent of the lobes to their

lateral width) to be 3 or larger.

The third new primary class is designated S (Figs. 108–111), which describes a small set of objects in which the projection on the sky of the most prominent nebular structure has a two-armed spiral shape. The apparent spiral structure first becomes evident at some finite radius out from the center, i.e., the spiral-shaped features do not go all the way in to the center. No lobe or shell structures can be seen, although diffuse nebulosity may be present. PNG 356.8+03.3 and PK032+07#2 are the best examples (Figs. 111, 110). Two other examples, PNG 002.9-03.9 and PNG 008.6-02.6 (Figs. 108, 109), show additional structures. PNG357.1-04.7 (Fig. 29), also shows a bright, two-armed spiral feature, but each arm is part of the opposing peripheries of a pair of lobes. This object, classified as B, appears therefore to be a connecting link between the S and the B or L classes.

The well-known, nearby PN, NGC 7293 (the Helix Nebula), with its two spiral-arm like structures observed in molecular-line (CO) emission (Young et al. 1999), shows considerable similarity to our class S objects. Two additional well-resolved examples of the S shape are NGC6309 (ground-based images in SCM92, Vázquez et al. 2008), and K4-55 (ground-based image in the IAC catalog: Metal96)[5]. In each of these two cases, one can discern that the spiral-shaped features are the highly brightened sides of very faint lobes. So it is not entirely clear whether S represents a new primary morphological class, or whether it should be regarded as a special case of bipolar with point-symmetric shape, B, $ps(s)$ (see § 3.2). While we suspect the latter to be plausible, we retain S as a separate class in view of the fact that some of the S objects show no signs of bipolar lobes. Deeper observations of the S systems can in principle resolve this question.

---

[5]also recently imaged with HST as the last image taken with the WFPC2 instrument before it was returned to Earth

In the PPN classification study by SMSC07, the morphologies are those of the optical continuum, resulting from dust-scattered light, whereas in this study, the morphologies that we are examining and classifying are dominated by Hα emission, and are therefore indicative of the ionized gas. This difference should be kept in mind when comparing the two studies. However, as discussed by SMSC07, the observed morphologies in both cases are a very good indicator of the geometric shapes of the lobe walls and other nebular structures.

3.2. Secondary Characteristics

The presence of secondary structural features in the nebulae is denoted with lower-case letters following the capital letter representing the major class. Below, we provide a brief summary of the secondary descriptors used for our PPN scheme, and introduce new ones which have had to be added in order to accommodate new features seen in PN morphologies. In general, the features to which we have chosen to assign descriptors, are those that appear to be common to multiple PNs, and which display some geometric symmetry or order.

For PPN, we first added secondary characeristics related to the lobes in the B, M, or E classes; if the lobes are open (i.e., like a vase) or closed at their outer ends (i.e., have a bubble-structure) they are denoted by o or c, respectively. We then characterised the central region of PPNs, where the presence of a dark obscuring band along the short axis of the nebula (i.e., a minimum in an intensity cut taken along the primary long axis of the nebula, and usually described as the "waist" of the nebula) was denoted by w. Evidence for point-symmetry in the nebular structure was denoted by ps. This classification was not applied to axially symmetric objects, even though axial symmetry is a special case of point-symmetry. The point-symmetry could be of three general types, resulting from (i) the presence of 2 or more pairs of diametrically-opposed lobes, denoted as $ps(m)$, (ii) the

distribution of ansae point-symmetrically about the center, denoted as $ps(an)$, and (iii) the overall geometrical shape of the lobes being point-symmetric, denoted as $ps(s)$.

Three additional nebular characteristics were included: (i) bright, compact knots in diametrically-opposed pairs, normally referred to as ansae, were denoted by an[6]; (ii) the presence of minor lobes as, for example, seen in the Frosty Leo Nebula (Sahai et al. 2000a), was denoted by ml, and (iii) a skirt-like structure around the primary lobes was denoted by sk. We define minor lobes as being distinctly smaller and thinner than the main lobes, noting that lobes whose lengths are significantly smaller but whose widths are comparable to those of the major lobes, are likely being foreshortened by projection – in such cases the object is classified as M (e.g., PK019-05#1, Fig. 36, and PK300-02#1, Fig. 44).

The presence of a halo[7] was denoted with h, with a qualifier e if it had an elongated shape, i.e., as $h(e)$. If the halo shape could not be determined reasonably, we added i, meaning that the shape was indeterminate, that is, as $h(i)$. The presence of arc-like structures in the halo, as for example seen in the Egg Nebula (Sahai et al. 1998b), was denoted by a: $h(a)$. Note that it is possible for a halo to have a smaller visible radial extent than the nebular lobes in the images shown. However, this does not necessarily imply that the physical radius to which the halo extends is smaller than the lobes, since halo sizes are likely to be brightness limited.

All of these secondary characteristic descriptors have been retained in our PN

---

[6]sometimes only one bright ansa-like knot (instead of a pair) is seen, we designate this as an?

[7]a diffuse structure which lies outside the bright primary nebular structure, and that can be clearly seen above the background sky; the halo surface brightness is typically a factor 10 or more less than that of the bright primary structure

scheme; but we have had to add new ones in order to account for the greater diversity of morphological features in PNs. These are described below.

3.2.1. Equatorial Waist & Central Region

The most important distinction between the PPN and PN secondary classifications is related to the appearance of the waist region. Since most surveys of PNs have been carried out in emission-line filters covering lines such as Hα, [NII]6583 and [OIII]5007, the waist almost always appears as a bright feature, rather than a dark feature. Indeed, for a bipolar, multipolar or collimated lobe planetary nebula, the waist is often the brightest structural component, which is understandable since the waist region is much more dense than the lobes. Note also that if the waist region is in expansion, then it will continue to flow radially outward from the star as a PPN evolves into a PN. The central regions of PNs with waists are thus, in general, expected to be more exposed and visible than those of the PPNs from which they evolve. Consequently, the region between the central star and the periphery of the waist is quite often well-resolved and is usually fainter than the periphery, giving the waist the appearance of a belt or toroid. Hence, we denote the presence of a bright waist region with t (for torus). Quite often, the torus region shows significant structure – if this is point-symmetric, as first found in PK285-02#1 (Fig. 43) by Sahai (2000; see his Fig. 1), we add the qualifier t, to the ps descriptor, i.e., as $ps(t)$. Additional examples of PNs which have point-symmetric torii are seen in Figures 38, 59, and 101.

Of course, very young PNs such as NGC 6302 (Matsuura et al. 2005) may still have optically thick waists fully or partially obscuring their central stars, and we retain the w descriptor for these. However, we exclude the b qualifier for the waist descriptor, which, in the case of PPNs, was used to denote a waist region with a sharp radial boundary, because in PNs, an abrupt, outer radial boundary is naturally generated in an ionization-bounded

medium and therefore does not represent the physical boundary of a radial density distribution.

In many bipolar (B), multipolar (M) or collimated-lobe (L) PNs, the bright central region departs significantly from the geometry of a torus, i.e., its extent along the long axis of the nebula is equal to or larger than its extent in the equatorial plane, and quite often has a barrel-shaped appearance. In these cases, the w or t descriptor is inadequate for describing this region; we therefore define a new descriptor called "barrel-shaped central region" or bcr – Figs. 119 and 120 show a collection of twelve such objects from our sample. If the ends of the barrel clearly appear to be closed or open, we add the qualifier c or o, respectively, to this descriptor, i.e., $bcr(c)$ (Fig. 119) or $bcr(o)$ (Fig. 120); if no judgment can be made, this qualifier is excluded. If the brightness distribution inside the central region has significant structure that appears irregular, we add the qualifier i: $bcr(i)$ (e.g., PK 002-09#1, PK 024+03#1, and PK 003+02#1: Figs. 3, 10, and 33). If the bcr shows point-symmetry (e.g., PK 235-03#1 and PK 356-03#3: Figs. 106, and 107), we denote this by adding the qualifier bcr to the point-symmetry descriptor: $ps(bcr)$.

Athough (i) a torus seen with its axis at some large angle to the sky plane and (ii) a barrel-shaped region seen with its axis nearly in the sky plane will both appear elliptical and thus superficially similar in shape, it is usually possible to distingush between these because for case i the major axis of the ellipse will be oriented orthogonally to the long axis of the nebula, whereas in case ii it will be oriented along the long axis. Thus, for example, PNG 001.7-04.4 (Fig. 98) is classified as $bcr(o)$, because the long axis of its bright central region lies along the long axis of the nebula.

The full set of descriptors for the central region (comprised of the bcr, w and t descriptors) is collected under the title "structured central region", replacing the phrase "obscuring waist" which was used in our PPN morphological scheme.

The torus in PK 331-02#2 (Fig. 81) shows a remarkable knotty appearance, giving it a necklace-like appearance, similar to that seen in the ground-based image of the newly discovered PN IPHASXJ194359.5+170901 (Corradi et al. 2010). These authors suggest that this torus results from a common envelope (CE) ejection episode (the central star in this PN is a known binary), and the knotty appearance may be either due to density fluctuations created during CE ejection and later exacerbated by the action of the expanding ionization front or the post-AGB fast wind, or fragmentation of the ejecta due to radiative shocks. Another example of a knotty torus is found in PNG097.6-02.4 (Fig. 128), which belongs to a new sample of compact PN recently imaged with HST (see § 3.5). If several additional objects with such knotty torii are found, we would recommend adding a qualifier to the t descriptor to capture this feature.

3.2.2. Other Nebular Characteristics

Inner Bubbles

Some PNs show the presence of small inner bubble structures which appear to lie entirely within the defining primary geometric structure characterised by the primary class. These are addressed by adding a new descriptor, *ib*, to the set of "other nebular characteristics". Some examples of PNs with inner bubbles are PK215-24#1, PK258-00#1, PK352-07#1, PK051-03#1, PK007-04#1, PK082+07#1 (Fig. 121), the Southern Crab (Corradi & Schwarz 1993), and MyCn18 (Sahai et al. 1999). The walls of these inner bubbles appear to contain much more highly-excited gas than the primary nebular shell, as indicated by a comparison of the [OIII] and Hα images for PK215-24°1 (Fig. 122): the average surface brightness of the inner bubble, as a fraction of the surface brightness of the primary shell, is much larger in the [OIII] image than in the Hα image. The inner bubble often has a pronounced point-symmetric shape (e.g., PK258-00#1, PK082+07#1), which is denoted by

adding the qualifier *ib* to the point-symmetry descriptor: *ps(ib)*.

Rings, Arcs, Radial Rays and Microstructure

Some PNs show ring-like features projected onto the lobes, e.g., the Etched Hourglass Nebula, MyCn18 (Sahai et al. 1999), NGC 6881 (Kwok & Su 2005), and Hb 12 (Kwok & Hsia 2007), which we denote with the descriptor *rg*. Both NGC 6881 (PK074+02#1: Fig 14) and Hb 12 (PK 111-02#1: Fig. 15) are included in our survey. However, the above studies show that the ring structures are generally less prominent in the Hα images compared to the [NII] images; and Hb 12 is the only object in our sample where the Hα image also shows these rings very faintly. There are two PPNs, the Red Rectangle (Cohen et al. 2004), and CRL 618 (Trammell & Goodrich 2002), which also show such rings. The 2-dimensional rings, which are generally co-axial with the long axis of the lobes in which they are found, appear to be structures which girdle the walls of the nebular lobes, like etchings on a wine glass. These are to be distinguished from the circular arcs seen in some PPNs and PNs, which are limb-brightened projections of 3-dimensional, geometrically-thin shell structures around the nebular center (denoted by the *a* qualifier of the *h* descriptor, i.e., as *h(a)*). Not many objects in our sample show arcs or rings in their halo. Deep imaging of the low surface brightness haloes by Corradi et al (2004) revealed several PNs having arcs; those authors summarise the new results from their work as well as objects already known to have these from earlier studies (NGC 6543, NGC 7027, NGC 3918, and Hb 5).

Other PNs show distinct microstructure, i.e. small-scale patterns of surface brightness variations, possibly weave-like in their appearance, over the body of their primary shell structure. For example, PK215-24#1 and PK258-00#1 (Figs. 71,75) show a weave-like pattern with large-scale order; the Etched Hourglass nebula shows a mottled pattern in the outer parts of the hourglass (Figs. 1 & 4, Sahai et al. 1999) – these are denoted by the

descriptor wv.

Some PNs show radial rays which, when projected inwards, appear to emanate from the central star. The best example of such features is NGC 6543. Balick (2004) finds that these features appear dark in an [OIII]/Hα ratio image, and have bright counterparts in [NII]λ6584 and other low-ionization lines. Balick infers that these rays are low-ionization structures, and most likely caused by "ionization-shadows" produced by dense knots opaque to stellar ionizing photons, and their ionization is the result of soft, diffuse UV (recombination) emission from neighboring gas. In support of this hypothesis, Balick finds that many of the rays can be traced back to dense knots in the inner parts of the nebula. We denote these radial ray features with the descriptor, rr. These radial rays are classified separately from the searchlight beams (listed as $h(sb)$ under halo characteristics, Table 2) as they are of higher multiplicity than the latter. The searchlight beams generally occur in pairs, and lie within a narrow angular region around the polar axis of the bipolar PPNs in which these have been seen (CRL 2688, IRAS18276: SMSC07).

We find that a few PNs belonging to the E (and in one case, R) primary class have small, diametrically-opposed protrusions jutting out from an otherwise smoothly curving geometrical shape describing the primary structure of the PN; these are accounted for by adding a new descriptor, pr, to the set of "other nebular characteristics". The prime examples of PNs showing protrusions are PK215-24#1, PK258-00#1 and PK016-01#1 (Figs. 71, 75, and 95), at position angles[8], $pa \sim 35°$, $pa \sim 90°$, and $pa \sim 95°$, respectively. Additional possible examples are: PNG351.1+04.8, PK027+04#1, PK315-13#1, and PK320-09#1 (Figs. 82, 102, 77, and 45). Both PK315-13#1, and PK320-09#1 (especially the latter) show not one pair, but multiple pairs of such protrusions.

---

[8]we define the position angle pa, as the angle measured anti-clockwise from the vertical axis in each image

Some PNs show additional nebular structures which cannot be easily described by the above descriptors, nor possess sufficient geometrical symmetry to merit new descriptors labelling their specific geometries. For such objects (e.g., PK304-04#1: Fig. 19), we add *ir* to the set of descriptors for "other nebular characteristics".

Halo

Although halos are expected to be filled (i.e., not limb-brightened), surface-brightness limited structures and therefore not expected to have a well-defined outer edge, we find a few objects where the halo has a sharp outer edge, or shows the presence of a discontinuity within it – we describe this pheomenon by adding a new qualifier, d, for the h descriptor: $h(d)$. Prime examples of this phenomenon are PK226-03#1 and PK232-04#1 (Figs. 72, 73); additional examples are PNG004.0-03.0, PK004+04#1, and PK107-13#1 (Figs. 55, 58, 69). Amongst these, PK004+04#1, PK064+04#1, and PK232-04#1 have a discontinuity within the halo; in each of these three cases, the discontinuous structure is elongated. We note that the halos with discontinuities occur only in class-E objects.

3.2.3. *Partially Ionized Objects*

If we compare the Hα image of the PN IRAS21282+5050 (PNG093.9-00.1), with its image using the broad-band filter (F606W) (Fig. 116), we find that the latter image shows considerably more structure, based on which we would give it a primary classification of M, rather than its Hα-based classification as E. It is clear that for this object, the Hα image is only showing the ionised inner region of the multiple lobes seen in the F606W image. This raises the possibility that for some small fraction of very young PN, where the ionization front has not reached the boundaries of the lobes, Hα will not reveal the full nebular morphology. In order to assess this fraction, we need to be able to compare Hα and deep

broad-band images for a sample of very young and dusty PNs like IRAS21282+5050.

We have examined the HST archive for broad-band images of PNs in our sample. Unfortunately broad-band images with adequate exposure times are not available for most of our sample (or for similar PNs). Only for a few young PNs, both emission-line (in either Hα or [NII]6583) and broad-band images are available; and we find that these objects have very similar morphologies in both images, e.g., PN G056.0+02.0 (also known as IRAS 19255+2123 and K 3-35, Fig. 112), PK 060-07#2 (also known as NGC 6886, Fig. 118), PK 321+03#1 (also known as He 2-113, Fig. 117), and PK 315-13#1. For the Etched Hourglass Nebula, MyCn18, the continuum image, taken with the medium-band filter F547M, shows a very similar hourglass (bipolar) morphology as seen in the Hα image, within the limitations of the lower SNR in the F547M filter (Sahai et al. 1999).

3.2.4. Offset Central Star

An additional feature of PNs which first became evident with the HST imaging of the PN, MyCn18 (Sahai et al. 1999) is that the central star of the PN can be offset from the center of symmetry of the nebula. The nebular structures in MyCn18 have a very high degree of geometric symmetry, and the central star location has been shown to be offset from the centers-of-symmetry of the former (such as the waist, and the hourglass lobes) (Figs. 2 & 4 in Sahai et al. 1999). Other examples of highly symmetric objects where the central star appears offset from the center of symmetry are the Starfish Twins, He 2-47 and M 1-37 (Figs. 1 & 2 in Sahai 2000; Figs. 43, 31 in this paper). The measurements of such offsets is not straightforward, and requires different strategies, on a case-by-case basis. We postpone the discussion of this feature of PN morphology, and the measurements of these

offsets, to a future paper. However, we introduce a new qualifier[9] to the * descriptor into our classification scheme (Table 2), as follows. We include the offset of the central star from the nebular center of symmetry in units of milliarcsec, with the number of significant figures giving an indication of the accuracy or reliability of the measurement. In cases where there are several geometric structures in the nebula relative to whose center the offset of the central star can be measured (as, e.g., in MyCn18), we select the largest of these offsets. The main goal of this descriptor is to *indicate* whether the offset is so small (closer to 0 than to 0.1″) as to be not measurable, or if it is evident. If scientific analysis is to be done based on the offset, then the actual measurements and their uncertainties in the literature will need to be directly confronted. We use *(0) for objects in which offsets are well measured to be zero (i.e., closer to 0 than to 0.1″), distinguishing them from those objects for which we just have * (i.e., inadequate information on the offset).

The morphological classifications for our sample of young PNs are given in Table 3. We classify MyCn 18, a striking and demonstrative example of many of the secondary characteristics of our scheme, as B,o,t,*(480),an,ib,wv,rg,ps(s,an).

3.3. Nebular Ages

The age of each object has been calculated using its angular size, distance, and radial outflow velocity. These parameters are listed in Table 3. The angular size of each PN was measured along its longest axis, using the typically well-defined edge of the nebular

---

[9]We defined a qualifier for the central star descriptor in our PPN survey paper, which represented the shortest wavelength (in μm) at which the central star is seen, but we do not use that qualifier for PNs because we are using either the Hα or [NII] filters for our classification, and the wavelength difference between these is small

structure, excluding the halo (which is scattered light from the outflowing remnant of the AGB mass-loss). For those PNs, where the edge is not clear, or does not exist because the lobes are not closed along the long axis, we have drawn a vector showing the adopted size. In some cases, where one lobe of the nebula is much fainter than the other (or lies outside the image field of view) so that its outer boundary cannot be determined reliably, we have used the radial length from the central star to the tip of the bright lobe as a measure of half the nebular size.

Our main source for distances is the online version of the Acker et al. (1992) catalog[10]. There are several methods used for estimating the distances presented in that catalog. Our first choice is to take values from the local extinction study (labelled E in the catalog). When multiple E values were found, the average was used. In the absence of extinction values, either the kinematical distance (labelled K in the catalog) or the spectroscopic parallax distance of binary companions (labelled S in the catalog) was used. For objects for which none of the above distances was available, we used the median values of all the distances listed in the Acker et al. catalog. For objects without distances in the Acker et al. catalog, we examined the published literature; for these the relevant references are listed in the footnotes to Table,3.

The [NII] expansion velocities from Acker et al. were used in calculating the sizes of each object; if the [NII] data were missing, the [OIII] expansion velocity was used. For objects where both the [NII] and [OIII] expansion velocities were absent, the median of all known [NII] expansion velocities for objects in our table was used ($22\,\mathrm{km\ s^{-1}}$). The ages were then calculated by dividing the physical size of each object by twice the expansion velocity. Although an accurate determination of expansion ages for our objects requires that we take into account the inclination and a 2-dimensional model of the geometry of

---

[10]http://vizier.u-strasbg.fr/viz-bin/Cat?V/84

the expanding structures, the approximation used here is adequate for obtaining rough estimates. We find that most of our objects are relatively young, with a median age of 2470 yr, consistent with our expectation based on the ST98 selection criterion. The median age of the 23 objects with $R_{exc} > 1$ is 2880 yr, so these are generally young objects as well.

The expansion velocities for bipolar PNs are usually found to be significantly higher in the lobes than in the waist or central regions, as is the case for bipolar PPNs. Thus, for most bipolar and multipolar objects, our derived ages are likely to be upper limits because the measured velocities are some global average that is less than the polar expansion velocities. When the expansion velocity is taken from [OIII] data, its value is expected to be smaller than the actual expansion velocity in the lobes, since the [OIII] emission is significantly more confined to the central region of PNs, and the expansion of the waist/central region is generally much slower than that of the lobes: the derived age is thus again an upper limit.

3.4. Classification Statistics

We have calculated the fractions of objects in different primary classes (Table 4), both using the sub-sample of PNs in which $R_{exc} \leq 1$ (96 objects) and the full sample (119 objects): the differences are not statistically significant. We find that the class-B and Class-E objects represent about $30 - 35\%$ of the total population – although the fraction of class-E is slightly more than class-B, the difference is only at the 1σ level. The class-M objects represent 20% of the population, somewhat smaller than the class-B objects. The three classes with collimated lobe structures (B, M & L) as a whole, represent slightly more than half the population: this must be considered a lower limit because objects in any of these 3 classes can appear to belong to class-E if they are distant and not well-resolved, or if they are projected in such a way that their polar axis makes a relatively small angle with respect to the line of sight. Objects in each of the remaining classes (I, R, L, and

S) represent less than 10% each of the total. The total numbers of objects in each of these classes is rather small, hence the differences in their populations are not significant or only marginally so. We note that point-symmetry is widespread, occurring (in one or more of its different types) in 45% of our sample. Although our sample is not complete, it is representative of young PNs, and the statistics presented here are significant because the sample is drawn from observing programs which are not biased towards any specific morphological class.

3.5.   Testing the Morphological Classification with a New PN Sample

We apply our new morphological classification scheme to a new sample of PNe recently imaged as part of an ongoing SNAPshot survey of PNs (Table 5). Although this survey did not include narrow-band filters covering either the Hα or the [NII] lines, inspection of the survey images shows that the F200LP and F350LP bandpasses, which are extremely wide, and cover all major nebular emission lines, including [OIII], [NII] and Hα, show the morphology most sensitively (e.g., Fig. 123). A representative fraction of the imaged objects is shown in Figs. 123–136. We find that our scheme can adequately describe all the morphologies seen in this sample, showing that it is quite comprehensive.

3.6.   Resolution, Sensitivity and Nebular Orientation

Our classification of any specific object may be affected by angular resolution, sensitivity and the object's orientation. Our scheme is aimed at minimizing the importance of orientation, but projection effects unavoidably affect the classification for extreme inclinations. A class-B or L nebula, with its long axis oriented at a small angle to the line of sight, will appear to be merely elongated (i.e., class E). A barrel-shaped configuration

viewed from near its axis will appear toroidal, or simply round, and an elongated halo can be projected to appear circularly symmetric. In those cases where we suspect that the geometrical projection of the nebula plays a role in determining its classification, we have so indicated in the notes on individual objects in Table 3.

Sensitivity, which depends on the exposure times, has the biggest affect on the detection and classification of the halo region, which generally has a much lower surface brightness than the bright nebular shell. So it is possible, and perhaps likely, that many of our objects possess faint haloes which are below the limit of our detection. Given HST's resolution of $0.05''$, and pixel sizes typically $0.046''$, we find that when the angular size is smaller than about $1.6''$ (e.g., Figs. 57, 84), but greater than about $1''$, most secondary descriptors listed under *Central Region* in Table 2, some of those listed under *Other Nebular Characteristics* (such as *ib* and *wv*), and the qualifiers for point symmetry in the Central Region, namely $ps(t, bcr, ib)$, cannot be reliably assigned. When the angular size is smaller than about $1''$, in addition to the above limitations, objects that are intrinsically B, M, or L may appear to be have a primary classification of E, and most secondary characteristics listed under *Lobes*, *Central Region*, and *Other Nebular Characteristics* in Table, 2 cannot be reliably assigned (although it may still be possible to distinguish an overall point-symmetry in the shape (i.e., $ps(s)$, see e.g., Fig. 79)). However, only a small fraction of objects in our sample is affected by insufficient angular resolution: 8 objects in our sample have angular sizes $\lesssim 1.6''$, and 4 of these 8 have sizes $\lesssim 1.1''$.

The errors in the determination of the angular extent affect the derivation of parameters such as age and diameter only in the smallest objects (size $\lesssim 1''$), but are still small compared to the systematic uncertainties in these estimates due to the poorly known distances, and/or expansion velocities.

The morphological assignment may be ambiguous if the image is not of sufficiently good

quality, and we have added question marks to descriptors for which we judge the assignment to be somewhat ambiguous. Furthermore, if the image is too poor to assign a classification for any particular characteristic, we simply did not include it in the classification. We expect the classifications to be refined, and possibly altered in some respects, as deeper and/or higher-resolution images become available.

4. Discussion: The Formation and Shaping of Planetary Nebulae

The images presented in this paper forcefully demonstrate why high-resolution imaging available from a space-based observatory like HST, as opposed to seeing-limited ground-based facilities, is critical, even for objects with an overall extent an order of magnitude larger than the seeing-limited resolution. In the ground-based images, not only are important structural features not discernible, even the qualitative assesment of the basic morphological class in a given classification scheme (e.g. whether the PN is elliptical or bipolar) can be incorrect (§ 1). This is because the waist regions of PNs are much brighter than the polar lobes - when convolved with a large seeing disk, the spatial spread of the waist region to a given intensity level is much larger than that of the much fainter polar regions - so a bipolar nebula can look artificially elliptical. Two striking examples of this effect are provided by the objects PK 300-02#1 and PK 000+17#1. PK 300-02#1, a bipolar nebula with a very large aspect ratio (7:1) (Fig. 44), looks like an unremarkable elliptical nebula with a much smaller aspect ratio (1.6:1) from the ground (Górny et al. 1999). Similarly, PK 000+17#1, whose ground-based image by SCM92 shows a featureless elliptical blob of size about $7''\!.\times5''\!.8$, is actually an extreme bipolar nebula with a polar extent of $6''$, and a waist of width $1''\!.3$ (Fig. 1). Thus the fraction of PNs which are bipolar is likely to be severely underestimated from ground-based imaging studies, with important implications for any hypothesis for their formation.

In this paper we have applied our morphological classification scheme developed for PPNs to young PNs, with modifications and extensions. This ready applicability of our previous scheme substantiates its validity and results from the strong morphological similarities between these two classes of objects evident in current imaging surveys with HST. One view, which has often been expressed at a series of international conferences devoted to understanding the formation of aspherical PNs (APN I-IV: e.g., Corradi, Manchado & Soker 2009), is that understanding PPN shapes is not a prerequisite to understanding PN shapes because ionization will destroy much or all the detailed geometric structure we see in highly-structured PPNs (e.g., multipolar objects like IRAS19024+0044). But given the striking similarities which we report between PPN and PN shapes (e.g., between IRAS19024+0044 and the Starfish Twin PNs), this view does not appear to be valid. The overall preservation of PPN shapes as they transform to PNs is likely a consequence of the following two causes: (1) the ionization fronts get trapped inside the dense walls of the nebular lobes, and (2) even if all of the lobe material in a PPN gets ionised, it maintains its shape, since its expansion velocity significantly exceeds the sound speed in ionised gas ($10 \, \mathrm{km \, s^{-1}}$). Current observations of several bipolar and multipolar PPNs provide evidence that their lobes are expanding at very high velocities ($\gtrsim 100 \, \mathrm{km \, s^{-1}}$).

4.1. The Morphological Evolution of Waists

The comparison between the PPN and PN samples, and the resulting new morphological descriptors, highlight the task ahead of us in trying to understand the formation of aspherical planetary nebulae. The emergence of new morphological features in PNs signifies the operation of new physical processes affecting the nebular shapes, as PPNs evolve into PNs. We must first consider the shaping which occurs during the PPN phase, which is the primary shaping stage (SMSC07). During this phase, (1) the dense mass-loss of the AGB

phase has already ceased and the inner edge of the dense circumstellar shell is advancing outward, and (2) a collimated, fast wind (i.e., the CFW) is sculpting the dense shell from the inside out. As the central star evolves towards higher temperatures, the primary shaping is followed by the action of the Spherical, Radiatively-driven, Fast Wind from the PN central star (hereafter SRFW), on the pre-shaped nebula. The fact that we see the biggest changes between PPNs and PNs in the central waist region clearly supports this scenario, since the waist material is the first to be encountered by the wind from the PN central star. The central regions of waists are expected to be more exposed and visible during the PN stage compared to the PPN stage, because the waists seen in PPNs are likely expanding structures, and further clearing of the central region occurs as a result of the SRFW.

The closed (c) and open (o) qualifiers on the bcr descriptor of the central region are diagnostic of differences in its structure during the preceding evolutionary phases. Thus, one may imagine that the $bcr(c)$ central regions result from the inflation of an originally compact structure that surrounded the central star in all directions, when the object was a PPN. Such a dusty structure has been proposed to surround the central star in the well-studied PPN, CRL 2688, by Sahai et al. (1998b). In contrast, $bcr(o)$ central regions may be produced in objects by the inflation of a highly flared disk or a toroidal central region. The inflating agent in both cases is the SRFW. A possible example of an object showing such inflation of a torus into a $bcr(o)$-type central region is PK002-09#1 (Fig. 3). The presence of irregular structure in the central region, captured by the i qualifier, may result from hydrodynamical instabilties produced during its inflation; the presence of geometric structure, captured by the g qualifier, is less easily understood. One possibility is that the collimated jet-like outflows which we know operate during the PPN phase remain active as the central star evolves to higher temperatures and starts driving the SRFW; the combined interaction of these two fast winds with themselves and the central region then results in either irregular or geometric structure of the latter, depending on the relative

speeds and momentum fluxes of these winds.

The continued evolution of a PN having a barrel-shaped central region (*bcr*) and a B-, M- or L- primary classification, may result in an object whose primary structure appears to be E, because the lobe regions have become too tenuous to be seen and only the bright *bcr* region is visible. A possible example of this phenomenon is PK327-02#1 (Fig. 80), where a pair of very faint lobes may be present, emanating from the top and bottom parts of the periphery of the elongated central region. This possibility could be tested out using deep imaging in low-excitation nebular lines such as [NII] and [OI], which may reveal such lobes.

There is a natural morphological continuity in primary classes from B, to L, to those which are E and have the *t* secondary characteristic. It is likely that class-L objects, or class-E objects having the *t* descriptor, were B earlier on in their evolution, but continued expansion of their waist regions as these objects evolved resulted in the loss of the pinched-in waist as the latter expanded out to become the toroidal feature.

4.2. The Rarity of Round PNs

Our survey shows that round PNs are rare: only 3.4% of our sample belongs to the R class. Soker (2002) discussed the rarity of round PNs; he proposed that most PNs evolve from binaries, which both enhances the AGB mass-loss rates (as a "final intensive wind") and makes the mass outflows non-spherically symmetric, whereas round PNs are objects which evolve from single stars (i.e., have no close companions, stellar or substellar); they also have low metallicity, so the AGB mass-loss rate is low, thus resulting in a relatively faint PN. Hence such objects are difficult to find. In contrast to the occurrence of R objects in our sample of PNs, there is a complete lack of round PPN (SMSC07). We hypothesize that this difference indicates that (i) a fast wind is needed in order to carve

out the aspherical cavities inside the AGB CSE for a post-AGB object to appear as a visible PPN, (ii) the fast wind is always collimated, to a smaller or larger degree. Hence, post-AGB objects which do not develop such collimated fast winds - i.e., most likely single stars with no close companions, stellar or substellar – show a shell-like structure only at the PN-phase, once the central star becomes hot enough to produce a SRFW, and ionize the swept-up circumstellar shell. This hypothesis could be tested with an extensive search for round PPNs with HST; if it is correct, we would not find any round PPNs.

4.3. New PN-specific Secondary Characteristics

Young PNs show more complex morphological features than PPNs. We have already discussed some of these above in connection with the central region. The addition of new descriptors and qualifiers to the list of secondary characteristics is indicative of new processes that apparently do not occur during the PPN phase. For example, inner bubbles (i.e., *ib*) are likely to represent emission from very hot gas in the reverse shock generated by the SRFW. This interpretation is supported most directly by the X-ray imaging observations of NGC 6543 (Chu et al. 2001), which show that the X-ray emission comes from an inner structure which would be classified as an inner bubble. In the case of PK215-24D1 (IC418), the [OIII] image clearly shows enhanced emission in the inner bubble region (Fig. 122).

The *wv* descriptor, which denotes the presence of small-scale patterns of surface brightness variations over the body of the primary shell structure, may be the result of specific hydrodynamical instabilities. It is noteworthy that, with one exception, all objects with *wv* belong to the E primary class.

The radial rays (labelled by the *rr* descriptor) and searchlight beams (labelled by the *sb* qualifier of the halo descriptor) may be related phenomena. In the case of the PPN,

CRL 2688, where these were first discovered, Setal98 presented a model in which the beams were the result of an obscuring dust cloud aroud the central star having a specific geometry: they proposed that the obscuring cloud has annular holes around the symmetry axis of the nebula, allowing the preferential leakage of starlight which illuminates the extended spherical circumstellar envelope to give the searchlight beam features. It appears plausible then, that when the central star evolves into a hot post-AGB star with a SRFW, the latter results in partial disintegration of this cloud, destroying its annular hole geometry and resulting in a less spatially-organized distribution of dust around the central star. The ionising radiation from the star can then be extincted along directions with optically thick dust clumps; it is along these directions that the radial rays are seen, as ionization shadows.

4.4. Comparison with Other Classification Schemes

We have compared our classification scheme with the detailed ones by SCS93+CS95 and Metal96, and we find obvious similarities as well as important distinctions (Appendix). We find that our classification system is broader and more comprehensive than the SCS93+CS95 and Metal96 systems, encompassing a more diverse array of morphologies (by employing a larger number of secondary descriptors), and is also more precise. These differences have mostly been motivated by the availability of high-resolution images of PNs obtained with HST. An important difference between our scheme and those of SCS93+CS95 and Metal96, at the primary classification level, is their inclusion of a separate point-symmetric class. The results of our study here show that point-symmetry can be present in objects in a variety of ways for all primary clases except those that belong to the irregular (I) class. Further, neither Metal96 nor SCS93+CS95 have multipolar or spiral-arm classes. Our scheme includes Metal96's class Q objects in our M (multipolar) class; it is not yet clear if the quadrupolar objects are distinct from those with more than 2 pairs of lobes.

The SCS93+CS95 and Metal96 schemes do not include any descriptors for the presence of halos.

An intriguing classification of PNs, devised by Soker & Hadar (2002: SH02), is based on the departure from an axisymmetic shape (considering only departures along and near the equatorial plane between structures on opposite sides of the nebular symmetry axis): SH02 discuss the connection between departure types and the physical mechanisms that may cause them, mainly resulting from the influence of a stellar binary companion. The PN images and the classification scheme here are relevant to the SH02 study in several ways, the most important of which is the widespread presence of point-symmetry in our PNs sample, rather than axial symmetry, which at the very least, severely restricts the sample of PNs subject to the SH02 classification. An possible example of an object in our sample that shows a "bent" departure from axisymmetry (as defined by SH02) is PK 000+17#2 (Fig. 1). One of the departures discussed by SH02 relates to the offset of the central star from the "center of the nebula": although we have included such an offset in our scheme, we have not implemented it in this paper, because in order to do so, one needs to define objective methods of finding the geometrical center of a nebula, and a quantitative estimate of the resulting uncertainty (§ 3.2.4).

4.5.   Physical Mechanisms Underlying Morphology

The morphological classes constituting the classification scheme presented in this paper were devised with minimal prejudice regarding their underlying physical cause. However, in many cases, physical causes are readily suggested by the geometry, supplemented by the kinematics that have been measured in some systems. Kinematic studies, mostly using high-resolution long-slit spectroscopy (e.g., review in López et al. 2004), are time-consuming, but will eventually be necessary to fully disentangle the 3-D morphology

of PNs where projection effects appear to be important. Several of the physical causes have been discussed above where the primary and secondary characteristics are defined.

Collimated lobe structures seen in the B or L classes imply the presence of collimated outflows but cannot directly tell us whether the collimation takes place near the central star(s) or is rather due to deflection by an equatorial concentration of matter, unless point-symmetry is also present. Although many hydrodynamical studies of interacting winds, with different assumptions about their geometries, have been carried out over the years (e.g., Mellema & Frank 1995, Lee & Sahai 2003, García-Arredondo & Frank 2004, Dennis et al. 2008), a new and focussed effort of hydrodynamical modelling is needed to address this issue, since simulations of hydrodynamical collimation undertaken so far suggest that the fast outflows are intrinsically collimated. For example, comparisons of simulations of a spherical wind interacting with an equatorially dense AGB envelope – the so-called Generalized Interacting Stellar Winds or GISW model (Kwok et al. 1978, Balick 1987) – does not produce the pinched-in shape of the lobes at their base characterizing class-B objects (see, e.g., Mellema & Frank 1995), even with very high equatorial to polar density contrast ratios. This discrepancy between data and models of this type highlights the importance of the pinched-in shape of the lobes in class-B PNs as a criterion for testing models.

In all cases, *point symmetry* indicates a secular trend – presumably precession – in the orientation of the central driver of a rapid, collimated outflow. Point-symmetry due to shape, $ps(s)$, or the presence of point-symmetric ansae[11], $ps(an)$, implies that the outflows are not collimated by hydrodynamical processes, but are intrinsically collimated, likely driven by a central accretion disk undergoing precession or wobbling of its axis. Numerical simulations are of course needed to verify whether precession can produce the several types

---

[11]which most likely result from the impact of a jet upon a slower-moving, prior wind

of point-symmetry covered in our classification scheme. A recent study by Raga et al. (2009) is a good first step in this direction. In this study, the authors show that models of accretion disks around a star in a binary system predict that the disk will have a retrograde precession with a period a factor of ∼2-20 times the orbital period, and they present an analytic, ballistic model and a three-dimensional gasdynamical simulation of a bipolar outflow from a source in a circular orbit, and with a precessing outflow axis. They find that this combination results in a jet/counterjet system with a small-spatial-scale spiral which is reflection-symmetric across the equatorial plane (resulting from the orbital motion) and a larger-scale, point-symmetric spiral (resulting from the longer period precession).

The multiple lobe pairs in class M objects also require intrinsically collimated flows or ejections. Hypotheses for producing such lobes have been discussed by Sahai et al. (2005) in connection with the starfish PPN, IRAS 19024+0044, and include a direction-changing bipolar jet driven by a wobbling accretion disk, or "explosive" ejections of matter along different directions driven by a correspondingly fast release of magnetic energy from the central star.

A *waist* is the signature of a strong equatorial concentration of matter, whether it be outflowing or in a bound Keplerian disk. If the equatorial concentration has expanded following a diminution or a cessation of mass loss, then an evacuated *toroidal* structure results, ionized and/or illuminated on its inside edge by the radiation from the central star. If the distribution of outflowing matter is less concentrated toward the system's equatorial plane, then, following the cessation of mass loss, the toroidal configuration will have a large vertical extent, and the ionization and illumination of its inside boundary will present a *barrel*-shaped appearance.

Ideally, one would like to relate nebular characteristics to fundamental, irreducible, physical variables innate to the system. The nebular morphology, when coupled with

velocity measurements, often provides access to variables that relate to the timing, such as the temporal history of the mass loss rate, and in particular the time since the cessation of rapid mass loss. Another innate variable is the presence of a binary companion to the mass-losing star, operationally expressed as the stellar mass ratio, separation and orbital eccentricity. This variable can affect the degree of concentration of the mass outflow towards the system's equatorial plane (e.g., Mastrodemos & Morris 1999), but in a rather complex way that requires elaborate dynamical modeling of the morphology and the velocity field in order to access those variables. De Marco (2009), following Soker (1997), summarises five main types of PN-shaping binary interactions as a function of just the binary separation. Amongst these types, close binaries which avoid a CE interaction (separation few to $\lesssim 100\,\mathrm{AU}$) or result in one (separation$\lesssim$few AU), are the ones most likely to produce dramatic departures from spherical symmetry in the central regions. During CE interactions in which the binary survives, the stellar envelope of the primary star can become unbound as a result of transfer of energy and angular momentum from the secondary (e.g., Iben & Livio 1993), and the ejected mass can be strongly concentrated in the equatorial plane (Sandquist et al. 1998). Thus CE ejection is a promising mechanism for producing the waist structure identified in our classification scheme for PNs and PPNs. CE interaction may also produce bipolar nebulae more often than single progenitors, as suggested by Miszalski et al. (2009)[12] who find a "penchant for bipolarity" in a sample of 30 post-CE PNs.

Another variable related to binarity is the rate of stellar rotation, which is likely to be significant enough to affect the geometry of the mass outflow only if a stellar merger has taken place during a CE interaction, or if tidal interaction in a close binary has

[12]these authors caution that further morphological studies are needed for a definitive conclusion on this issue

synchronized the primary rotation with the orbit of the secondary. Other fundamental variables enter the picture if a stellar magnetic field plays a role in shaping the stellar mass outflow (e.g., Pascoli 1997, Chevalier & Luo 1994; García-Segura 1997, García-Segura et al. 1999, Blackman et al. 2001): the magnetic geometry, strength, and orientation. However, Soker (2006) argues that in order to sustain a sufficiently strong global magnetic field for an adequate period of time during which mass can be ejected in a collimated manner, angular momentum needs to be continuously supplied to the star, and this can only come from a companion, hence magnetic fields may play a role, but are perhaps not the fundamental underlying agent shaping PNs.

Additional innate variables are needed to account for the point symmetry displayed by a large fraction (almost 50%) of the nebulae presented here (e.g., variables relating to the coupling of orbital and rotational angular momenta might be important in this context, but the cause of the precession of the central driver has not been identified yet in any system). Finally, we note that yet unidentified variables may be needed to account for the multipolarity of many systems and for the arc features and other discontinuities observed in the halos of many well-observed PNs and PPNs. It is clear that this will remain a dynamic area of research for some time to come.

APPENDIX

SCS93+CS95's main morphological classes are elliptical (E), bipolar (B), point-symmetrical (P), and irregular (I). We ignore the trivial class of unresolved (poorly) resolved objects which SCS93+CS95 label "stellar (gaussian)" . The *elliptical* class includes both round and elliptical shaped objects. *Bipolar* objects are defined as axially symmetric PNs with an equatorial waist from which two faint extended lobes emanate, *point-symmetric* are objects whose morphological components show point-symmetry around the center, *irregular* objects have shapes lacking geometric symmetry and which therefore do not fall in the previous 3 classes. Metal96 have 5 primary classes: round (R), elliptical (E), bipolar (B), quadrupolar (Q), and point-symmetric (P). The definitions of the classes in common with CS95 (i.e., R, E, B, and P) are the same. SCS93+CS95 and Metal96 add descriptors (lower-case letters) to their primary class descriptors to denote the presence of additional structures. Thus, for E and R, Metal96, add 3 descriptors: "s" for those with inner structures, "a" for those with ansae, and "m" is when any of these exhibit multiple shells. SCS93+CS95 also use "s" and "m" descriptors with similar meanings for their E class, but don't have an "a" descriptor. For the B class, Metal96 add a descriptor "r" if the objects show a "marked bright ring", whereas SCS93+CS95 add "m" for those which show "multiple events". Metal96's class Q objects have two pairs of lobes, and objects which are too irregular to fit onto the above are called non-classified or "NC" (hence the same as SCS93+CS95's I objects). Our round and elongated classes correspond to Metal96's R and E classes; our bipolar and "collimated lobe pair" classes correspond to Metal96's B class, and our irregular class is similar to Metal96's NC class.

REFERENCES

Acker, A., Ochsenbein, F., Stenholm, B., Tylenda, R., Marcout, J. & Schohn, S. 1992, Strasbourg-ESO Catalog of Galactic Planetary Nebulae, European Southern Observatory, Garching

Balick, B. 1987, AJ, 94, 671

Balick, B. 2004, AJ, 127, 2262

Balick, B., Preston, H. & Icke, V. 1987, AJ, 94, 164

Balick, B. & Frank, A. 2002, ARA&A, 40, 439

Blackman, E. G., Frank, A., & Welch, C. 2001, ApJ, 546, 288

Bryce, M., Lopez, J. A., Holloway, A. J., & Meaburn, J. 1997, ApJ, 487, L161

Bond, H. and Livio, M. 1990, ApJ, 355, 568

Bujarrabal. V., Garcia-Segura, G., Morris,M., Soker, N. & Terzian, Y. 2000 *Asymmetrical Planetary Nebulae II: From Origins to Microstructures*, eds. Kastner, Soker, & Rappaport, ASP, 199, 201

Bujarrabal, V., Castro-Carrizo, A., Alcolea, J., & Sánchez Contreras, C. 2001, A&A, 377, 868

Cohen, M., Van Winckel, H., Bond, H. E., & Gull, T. R. 2004, AJ, 127, 2362

Chevalier, R. A., & Luo, D. 1994, ApJ, 421, 225

Chu, Y.-H., Guerrero, M. A., Gruendl, R. A., Williams, R. M., & Kaler, J. B. 2001, ApJ, 553, L69

Corradi, R. L. M., & Schwarz, H. E. 1993, A&A, 268, 714

Corradi, R. L. M., & Schwarz, H. E. 1995, A&A, 293, 871

Corradi, R.L.M., Manchado, A. & Soker, N. 2009, *Asymmetrical Planetary Nebulae IV*, I.A.C. electronic publication

Corradi, R.L.M., Guerrero, M., Manchado, A., & Mampaso, A. 1997, New Astronomy, 2, 461

Corradi, R. L. M., Sánchez-Blázquez, P., Mellema, G., Giammanco, C., & Schwarz, H. E. 2004, A&A, 417, 637

Corradi, R.L.M. et al. 2010, MNRAS (in press), also arXiv:1009.1043v1

Dayal, A., Sahai, R., Watson, A. M., Trauger, J. T., Burrows, C. J., Stapelfeldt, K. R., & Gallagher, J. S., III 2000, AJ, 119, 315

De Marco, O., & Crowther, P. A. 1998, MNRAS, 296, 419

De Marco, O. 2009, PASP, 121, 316

Dennis, T. J., Cunningham, A. J., Frank, A., Balick, B., Blackman, E. G., & Mitran, S. 2008, ApJ, 679, 1327

Dgani, R., and Soker, N. 1998, ApJ, 495, 337

Dobrinčić, M., Villaver, E., Guerrero, M. A., & Manchado, A. 2008, AJ, 135, 2199

Durand, S., Acker, A., & Zijlstra, A. 1998, A&AS, 132, 13

Garcia Lario, P., Manchado, A., Riera, A., Mampaso, A., & Pottasch, S. R. 1991, A&A, 249, 223

García-Arredondo, F., & Frank, A. 2004, ApJ, 600, 992

Garcia-Segura, G. 1997, ApJ, 489, L189

Garcia-Segura, G., Langer, N., Rozyczka, M., & Franco, J. 1999, ApJ, 517, 767

Gesicki, K., & Zijlstra, A. A. 2007, A&A, 467, L29

Górny, S. K., Schwarz, H. E., Corradi, R. L. M., & Van Winckel, H. 1999, A&AS, 136, 145

Iben, I., Jr., & Livio, M. 1993, PASP, 105, 1373

Kerber, F., Lercher, G., & Weinberger, R. 1996, A&AS, 119, 423

Kunder, A., & Chaboyer, B. 2009, AJ, 137, 4478

Kwok, S., Purton, C. R., & Fitzgerald, P. M. 1978, ApJ, 219, L125

Kwok, S., & Su, K. Y. L. 2005, ApJ, 635, L49

Kwok, S., & Hsia, C. H. 2007, ApJ, 660, 341

Lee, C.-F., & Sahai, R. 2003, ApJ, 586, 319

López, J. A., García-Segura, G., & Steffen, W. 2004, Asymmetrical Planetary Nebulae III,
    ASP Conference Proceedings, 313, 161

Manchado, A., Guerrero, M. A., Stanghellini, L., & Serra-Ricart, M. 1996a, The IAC
    morphological catalog of northern Galactic planetary nebulae, Publisher: LaLaguna,
    Spain: Instituto de Astrofisica de Canarias (IAC)

Manchado, A., Stanghellini, L., Guerrero, M.A. 1996b, ApJ, 466, L95

Mastrodemos, N., & Morris, M. 1999, ApJ, 523, 357

Matsuura, M., Zijlstra, A. A., Molster, F. J., Waters, L. B. F. M., Nomura, H., Sahai, R.,
    & Hoare, M. G. 2005, MNRAS, 359, 383

Mellema, G., & Frank, A. 1995, MNRAS, 273, 401

Miszalski, B., Acker, A., Parker, Q. A., & Moffat, A. F. J. 2009, A&A, 505, 249

Morris, M. 1981, ApJ, 249, 572

Morris, M. 1987, PASP, 99, 1115

Morris, M. 1990, in FROM MIRAS TO PLANETARY NEBULAE: Which Path for Stellar Evolution, Eds. M.O. Mennessier & A. Omont, (Editions Frontieres), p520

Pascoli, G. 1997, ApJ, 489, 946

Preite-Martinez, A. 1988, A&AS, 76, 317

Rozyczka, M. & Franco, J. 1996, ApJ, 469, L127

Raga, A. C., Esquivel, A., Velázquez, P. F., Cantó, J., Haro-Corzo, S., Riera, A., & Rodríguez-González, A. 2009, ApJ, 707, L6

Sahai, R. 2000, ApJ, 537, L43

Sahai, R., Hines, D.C., Kastner, J.H., Weintraub, D.A., Trauger, J.T., Rieke, M.J., Thompson, R.I., & Schneider, G. 1998a, ApJ, 492, L163

Sahai, R., et al., 1998b, ApJ, 493, 301

Sahai, R. and Bieging, J.H. 1993, AJ, 105, 595

Sahai, R., Wootten, A., Schwarz, H.E., & Clegg, R.E.S. 1991, A&A, 251, 560

Sahai, R. & Trauger, J.T. 1998, AJ, 116, 1357 (ST98)

Sahai, R., et al. 1999, AJ, 118, 468

Sahai, R., Bujarrabal, V., Castro-Carrizo, A., & Zijlstra, A. 2000, A&A, 360, L9

Sahai, R., Nyman, L.-Å., & Wootten, A. 2000, ApJ, 543, 880

Sahai, R. 2004, in *Asymmetrical Planetary Nebulae III*, eds. M. Meixner, J.H. Kastner, B. Balick, & N. Soker, ASP Conf. Ser., 313, 141

Sahai, R. 2003, IAU Symposium 209, *Planetary Nebulae: Their Evolution and Role in the Universe*, Eds. Sun Kwok, Michael Dopita, and Ralph Sutherland,, 209, 471

Sahai, R., Sánchez Contreras, C., & Morris, M. 2005, ApJ, 620, 948

Sahai, R., Young, K., Patel, N. A., Sánchez Contreras, C., & Morris, M 2006, ApJ, 653, 1241

Sahai, R., Morris, M., Sánchez Contreras, C., & Claussen, M. 2007a, AJ, 134, 2200 (SMSC07)

Sahai, R., Sánchez Contreras, C., Morris, M., & Claussen, M. 2007b, ApJ, 658, 410

Sandquist, E. L., Taam, R. E., Chen, X., Bodenheimer, P., & Burkert, A 1998, ApJ, 500, 909

Schwarz, H.E. 1992, A&A, 264, L1

Schwarz, H. E., Aspin, C., & Lutz, J. H. 1989, ApJ, 344, L29

Schwarz, H.E., Corradi, R.L.M. & Melnick, J. 1992, A&ASS, 96, 23

Schwarz, H. E., Corradi, R. L. M., & Stanghellini, L. 1993, Planetary Nebulae, 155, 214

Schwarz, H. E., Aspin, C., Corradi, R. L. M., & Reipurth, B. 1997, A&A, 319, 267

Soker, N. 1990, AJ, 99, 1869

Soker, N. 1992, ApJ, 389, 628

Soker, N. 1996a, ApJ, 468, 774

Soker, N. 1996b, ApJ, 460, L53

Soker, N. 1997, ApJS, 112, 487

Soker, N. 2002, A&A, 386, 885

Soker, N. 2006, PASP, 118, 260

Soker, N. & Livio, M. 1989, ApJ, 339, 268

Soker, N. & Livio, M. 1994, ApJ, 421, 219

Soker, N., & Hadar, R. 2002, MNRAS, 331, 731

Suárez, O., García-Lario, P., Manchado, A., Manteiga, M., Ulla, A., & Pottasch, S. R. 2006, A&A, 458, 173

Trammell, S. R., & Goodrich, R. W. 2002, ApJ, 579, 688

Van de Steene, G. & Zijlstra, A.A. 1995, A&A, 293, 541

Vázquez, R., Miranda, L. F., Olguín, L., Ayala, S., Torrelles, J. M., Contreras, M. E., & Guillén, P. F. 2008, A&A, 481, 107

Young, K., Cox, P., Huggins, P. J., Forveille, T., & Bachiller, R. 1999, ApJ, 522, 387

Zijlstra, A. A., Gesicki, K., Walsh, J. R., Péquignot, D., van Hoof, P. A. M., & Minniti, D. 2006, MNRAS, 369, 875
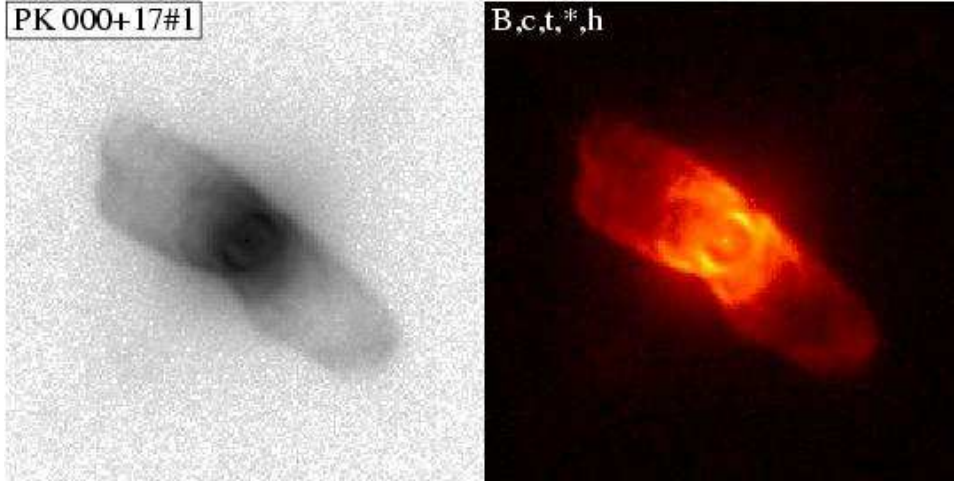
Fig. 1.— PK 000+17#1 – left panel shows HST Hα image (log stretch, reverse grey-scale), right panel shows the same image, processed to enhance sharp structures, in false-color. The panel length along the horizontal axis is given in Table 3 [**The quality of this and following figures as it appears in the arXiv pdf output is not up-to-par; the full ms with high-quality figures is available by anonymous FTP at ftp://ftp.astro.ucla.edu/pub/morris/AJ-360163-sahai.pdf**].
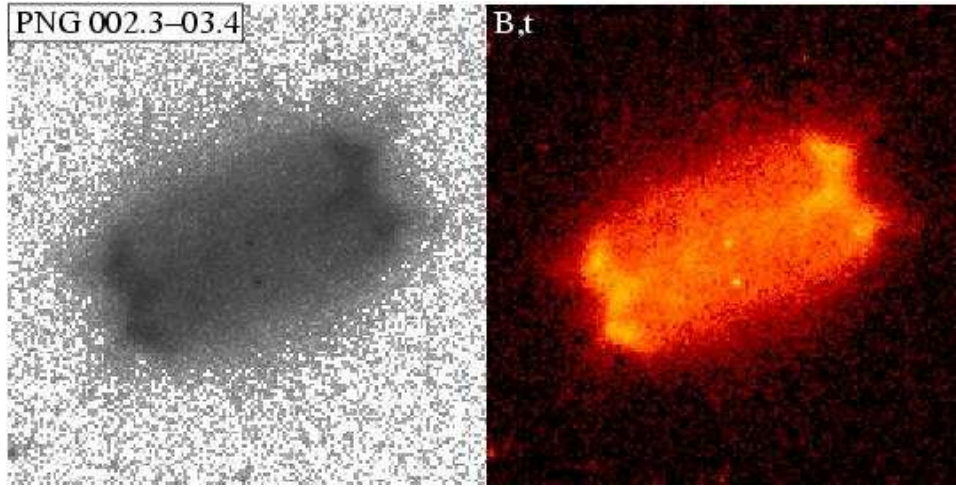
Fig. 2.— As in Fig 1., but for PNG002.3-03.4.
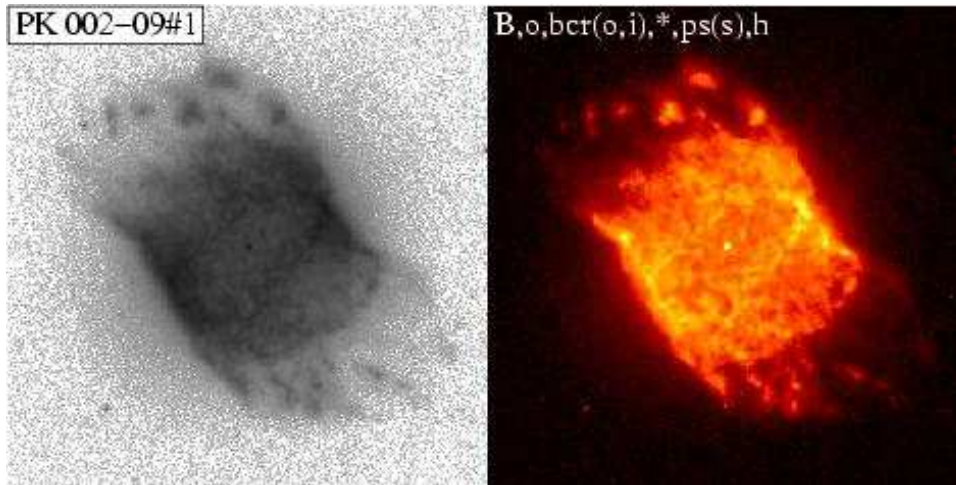
Fig. 3.— As in Fig 1., but for PK 002-09#1.
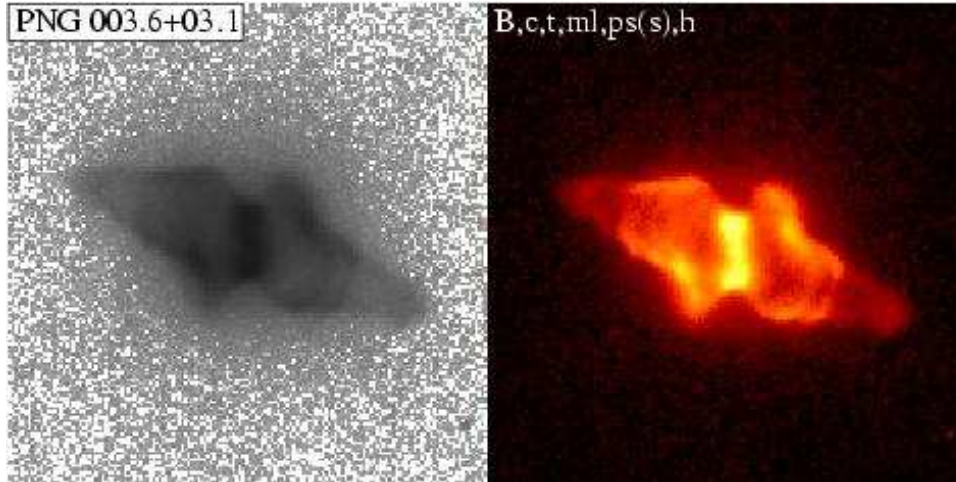
Fig. 4.— As in Fig 1., but for PNG003.6+03.1.
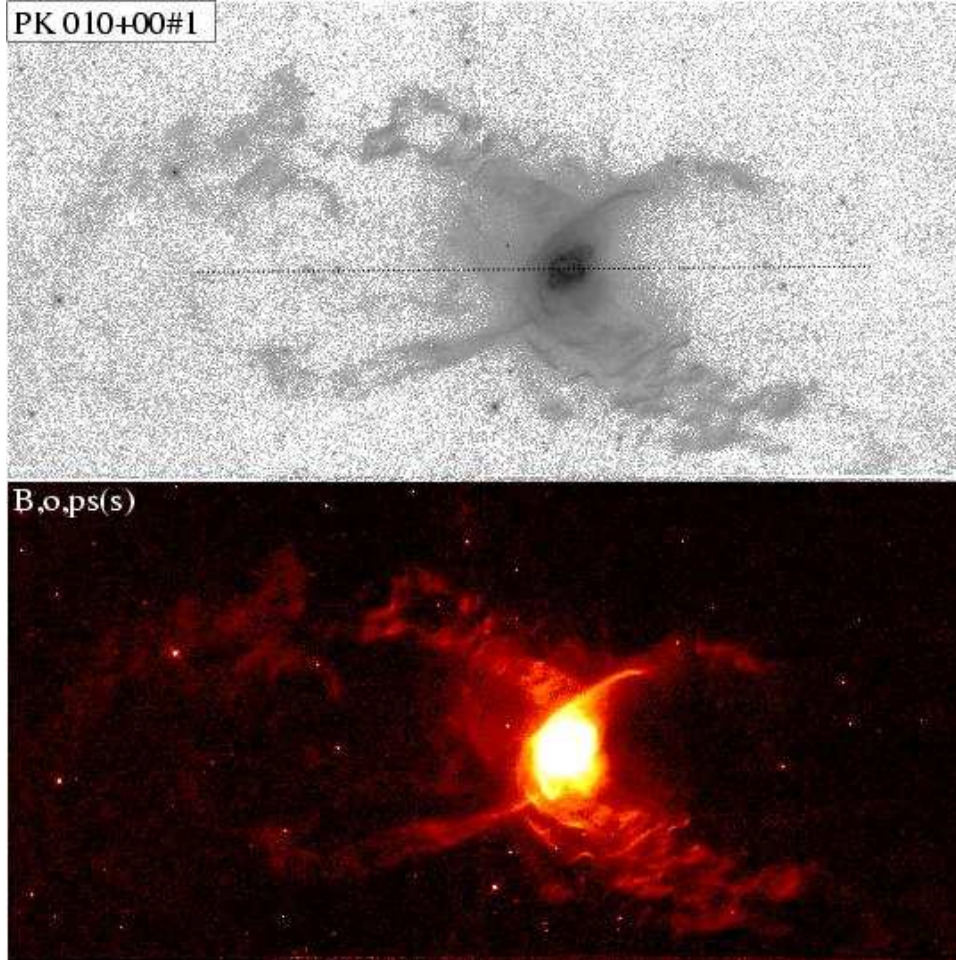
Fig. 5.— As in Fig 1., but for PK 010+00#1
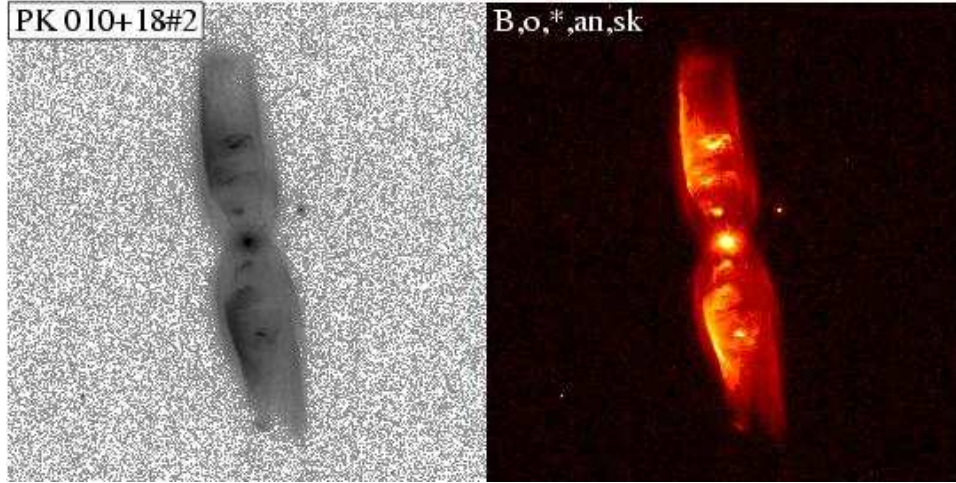
Fig. 6.— As in Fig 1., but for PK 010+18#2.
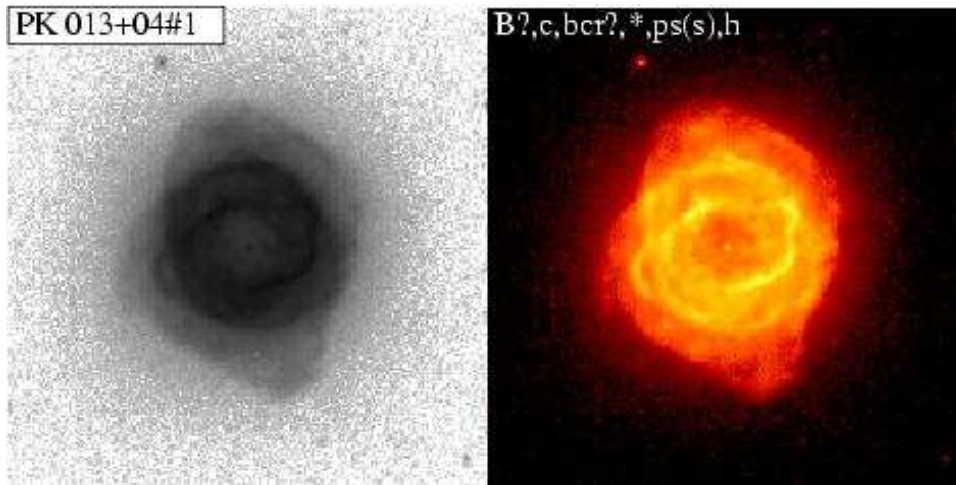
Fig. 7.— As in Fig 1., but for PK 013+04#1 and the F658N ([NII]) filter.
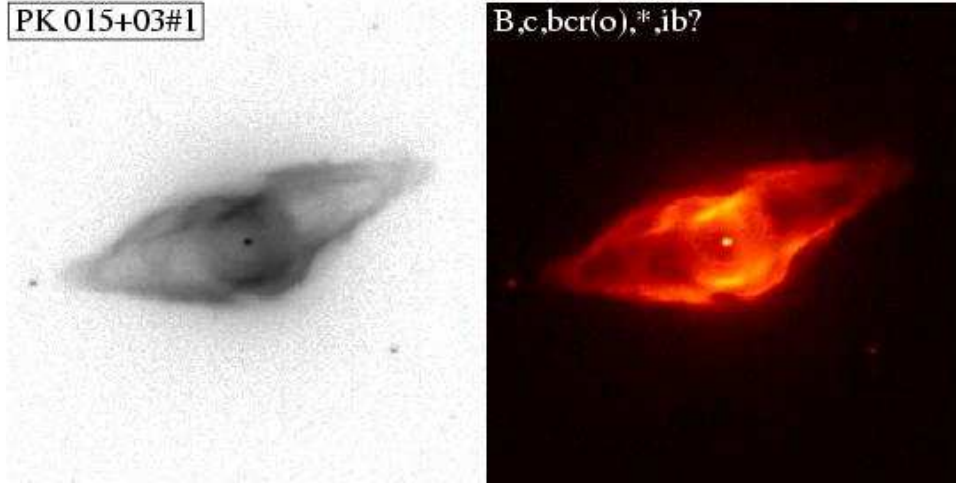
Fig. 8.— As in Fig 1., but for PK 015+03#1.
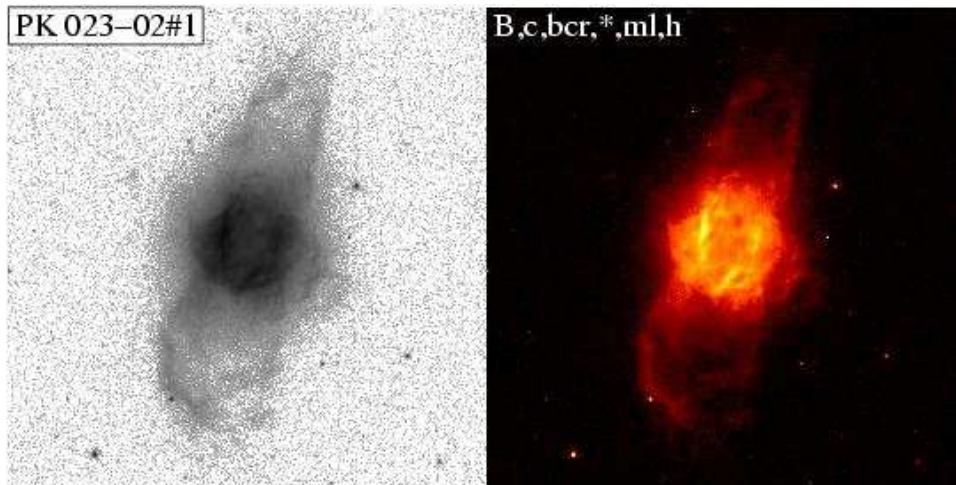
Fig. 9.— As in Fig 1., but for PK 023-02#1.
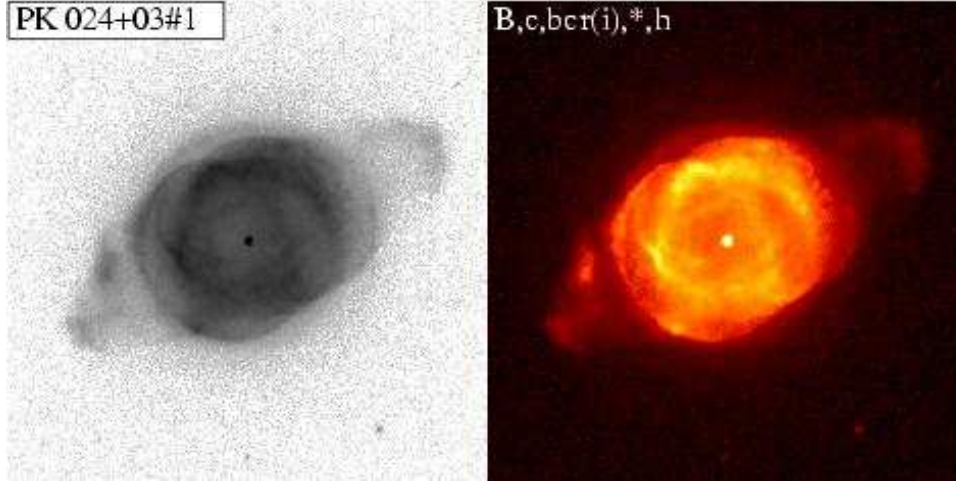
Fig. 10.— As in Fig 1., but for PK 024+03#1.
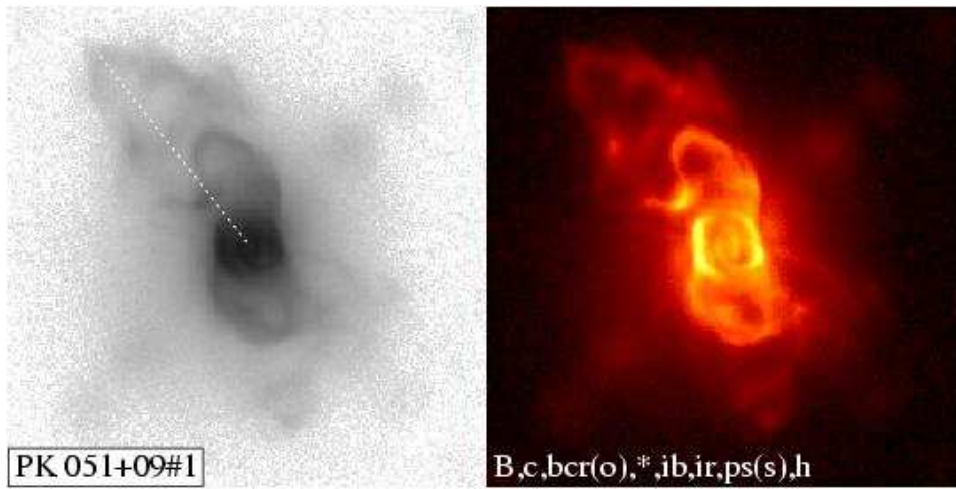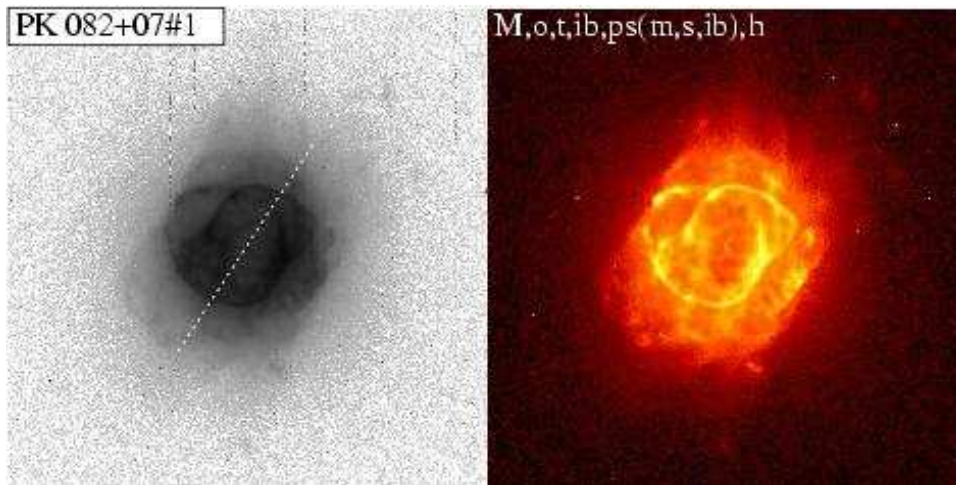

Fig. 11.— As in Fig 1., but for PK 051+09#1.
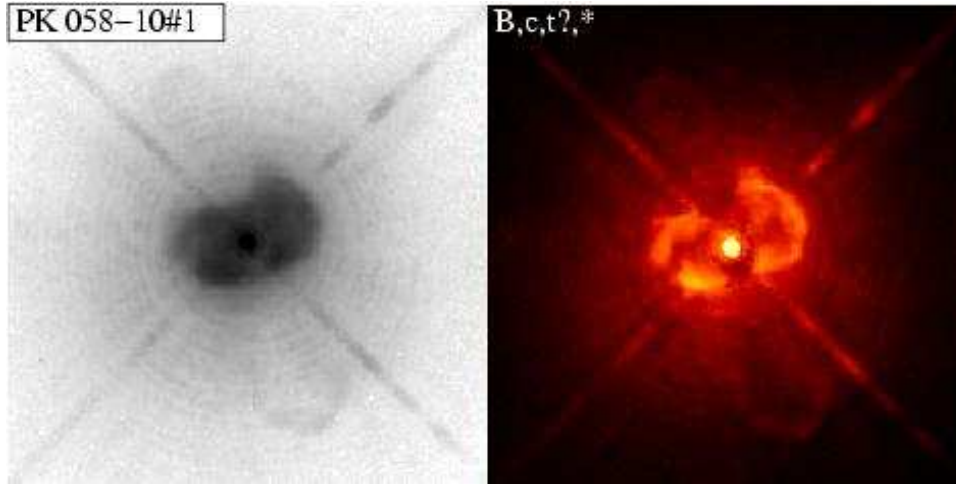
Fig. 12.— As in Fig 1., but for PK 058-10#1.
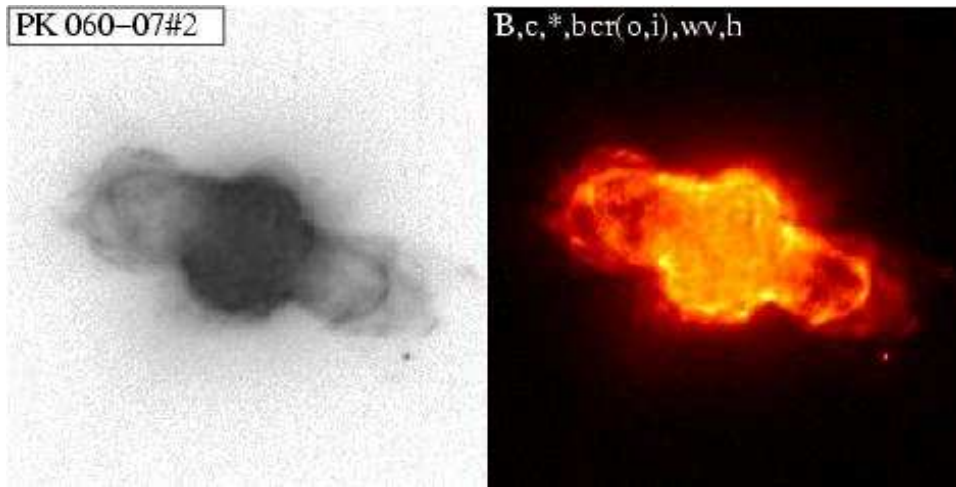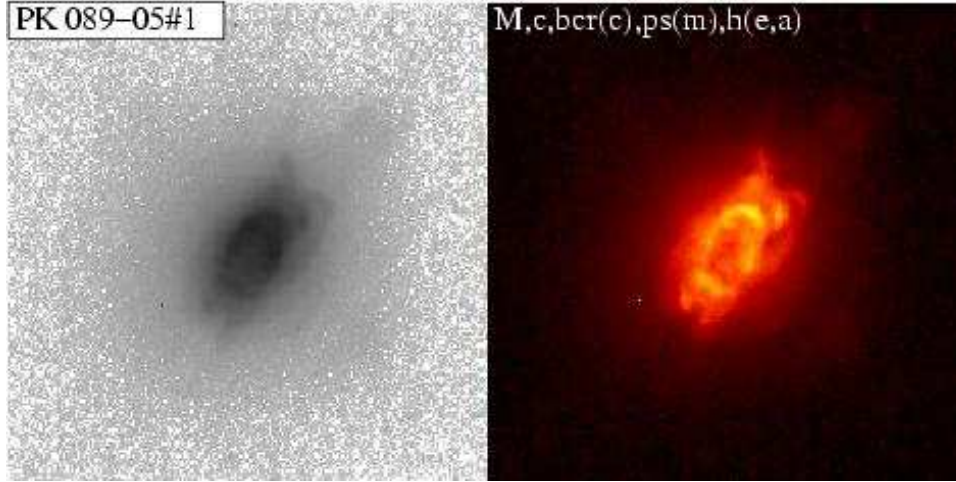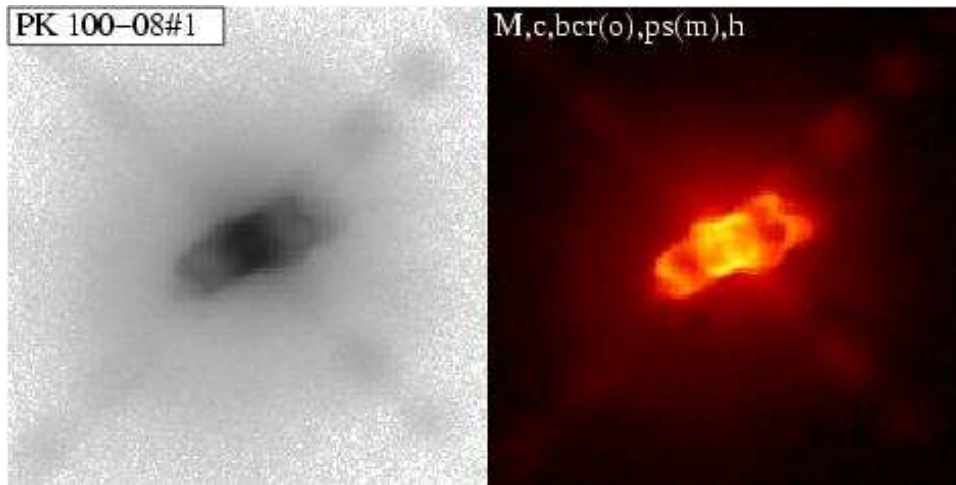

Fig. 13.— As in Fig 1., but for PK 060-07#2.
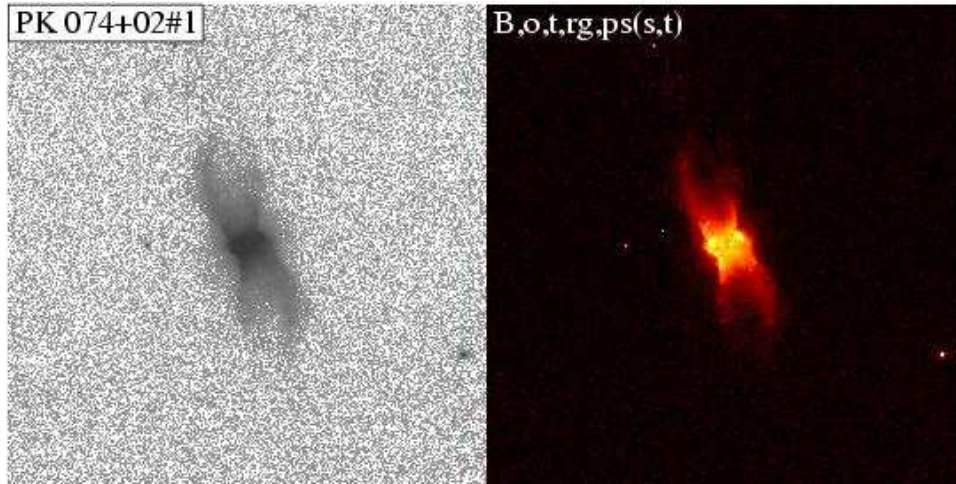
Fig. 14.— As in Fig 1., but for PK 074+02#1.
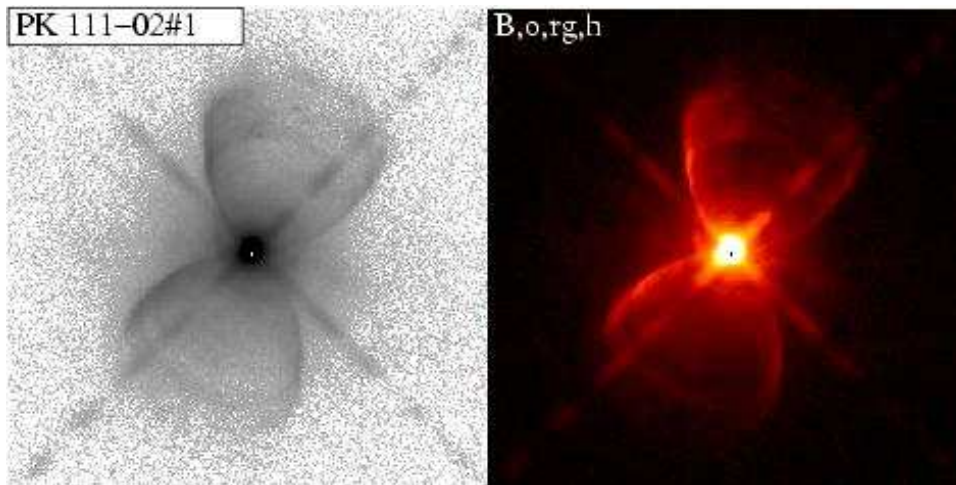
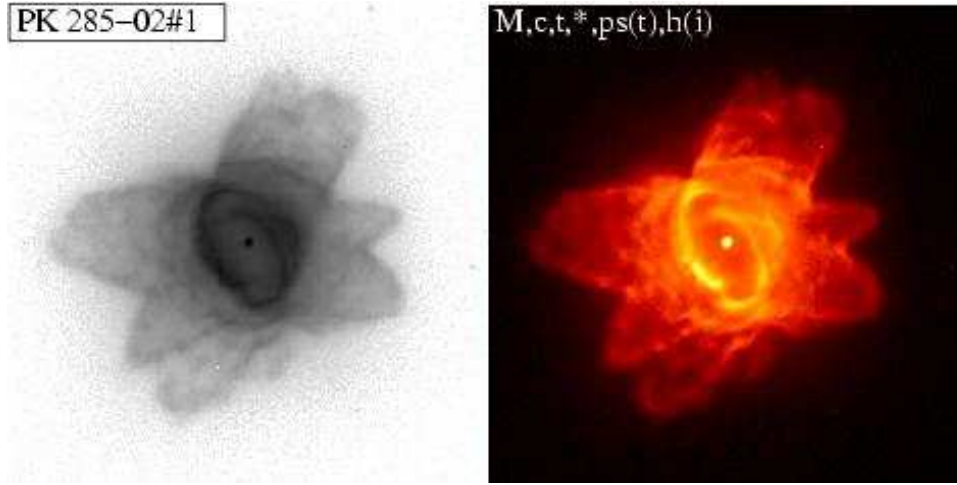Fig. 15.— As in Fig 1., but for PK 111-02#1 (adapted from ST98).
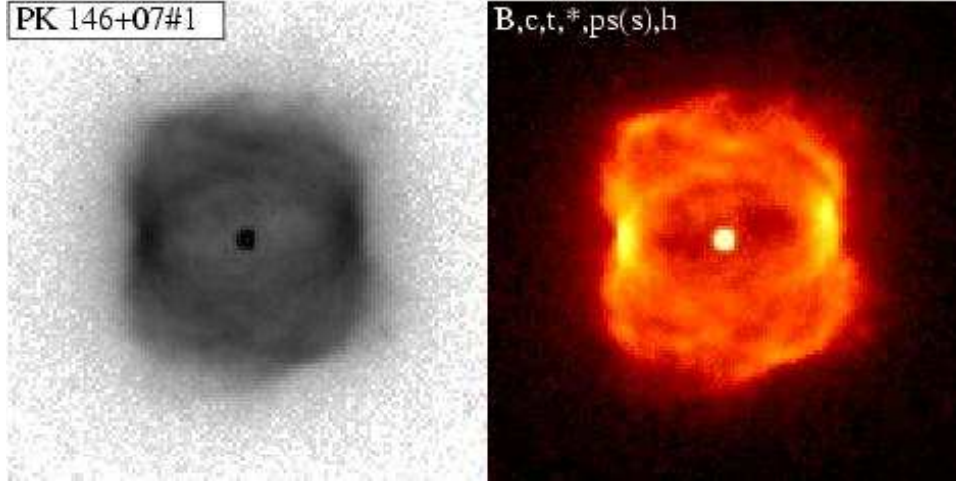
Fig. 16.— As in Fig 1., but for PK 146+07d1 (adapted from ST98).
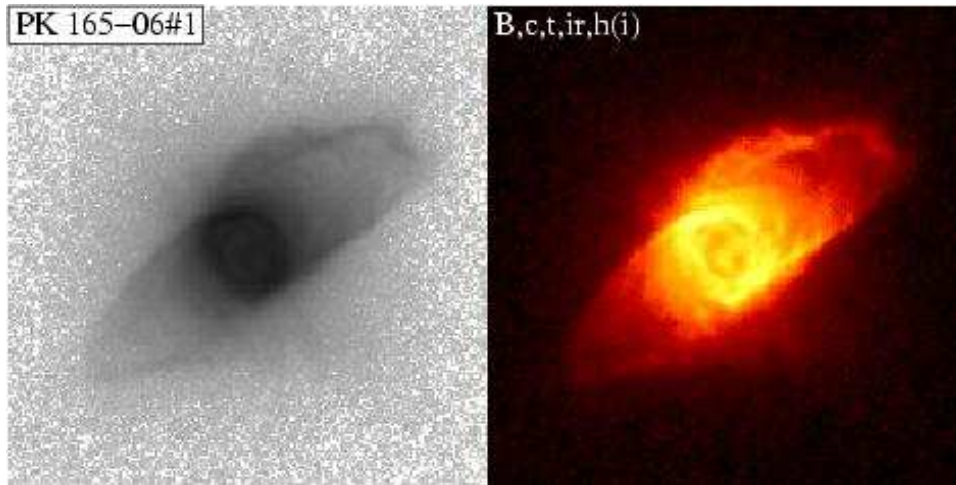
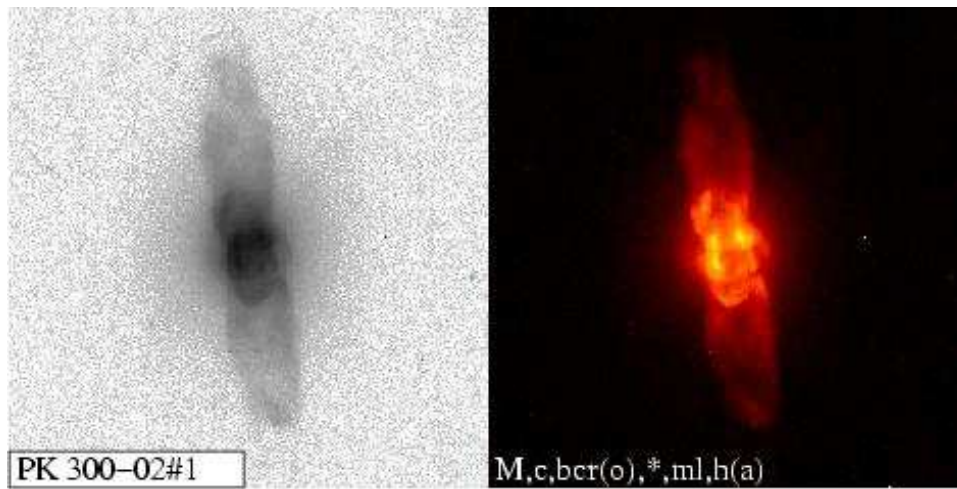Fig. 17.— As in Fig 1., but for PK 165-06#1.
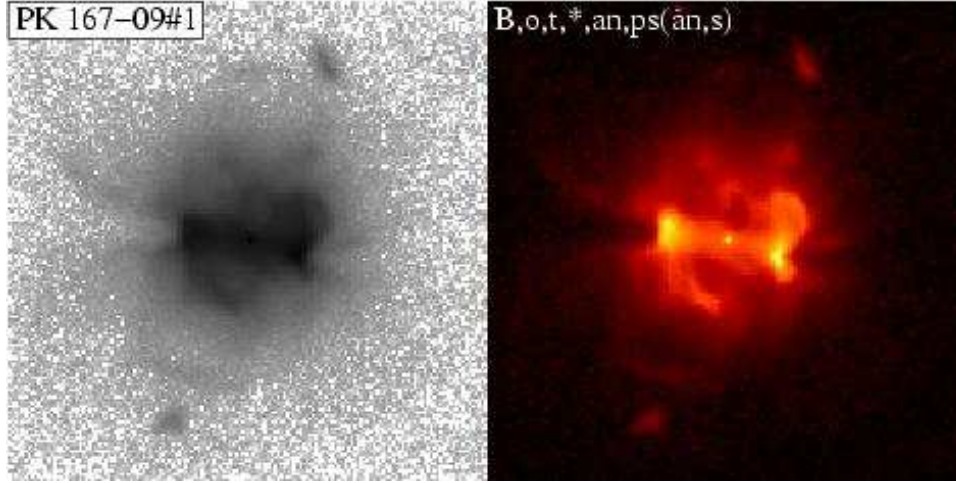
Fig. 18.— As in Fig 1., but for PK 167-09#1 (adapted from ST98).
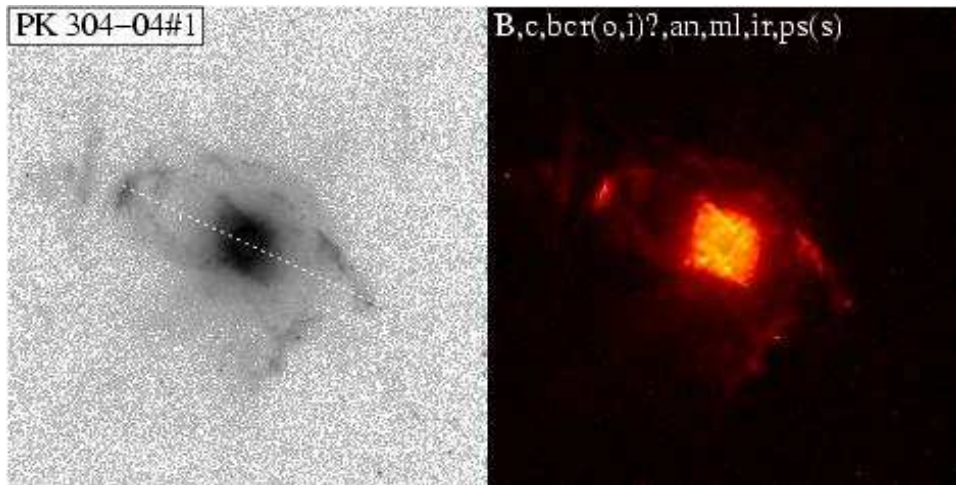
Fig. 19.— As in Fig 1., but for PK 304-04#1.
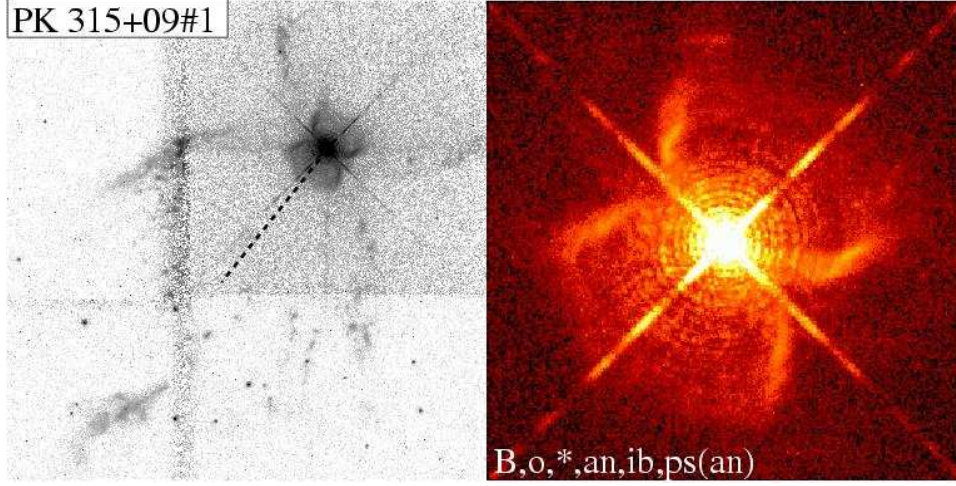
Fig. 20.— As in Fig 1., but for PK 315+09#1 (adapted from ST98). The field-of-view in the left panel does not cover the ansa feature diametrically opposed to the one seen in the lower left corner (see Corradi & Schwarz 1993 for a full view). The right panel shows only the central region ($12.2'' \times 12.2''$).
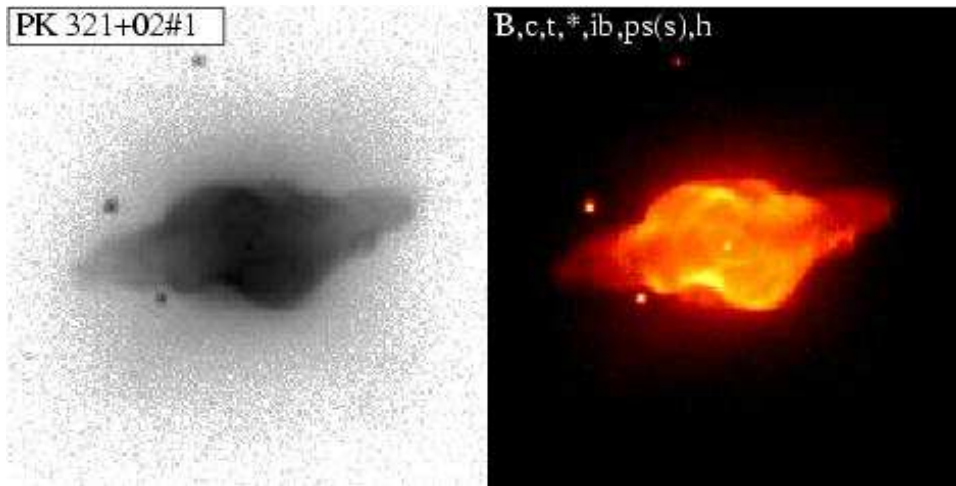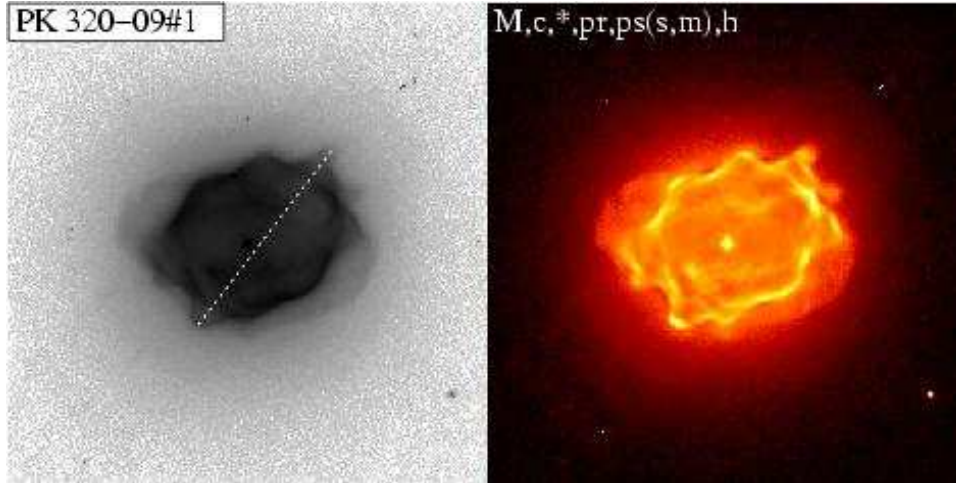

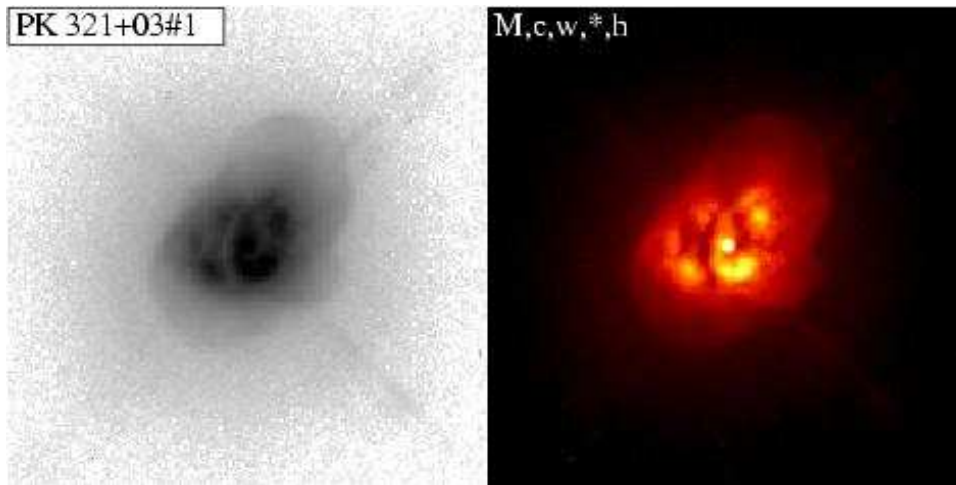Fig. 21.— As in Fig 1., but for PK 321+02#1 (adapted from ST98).
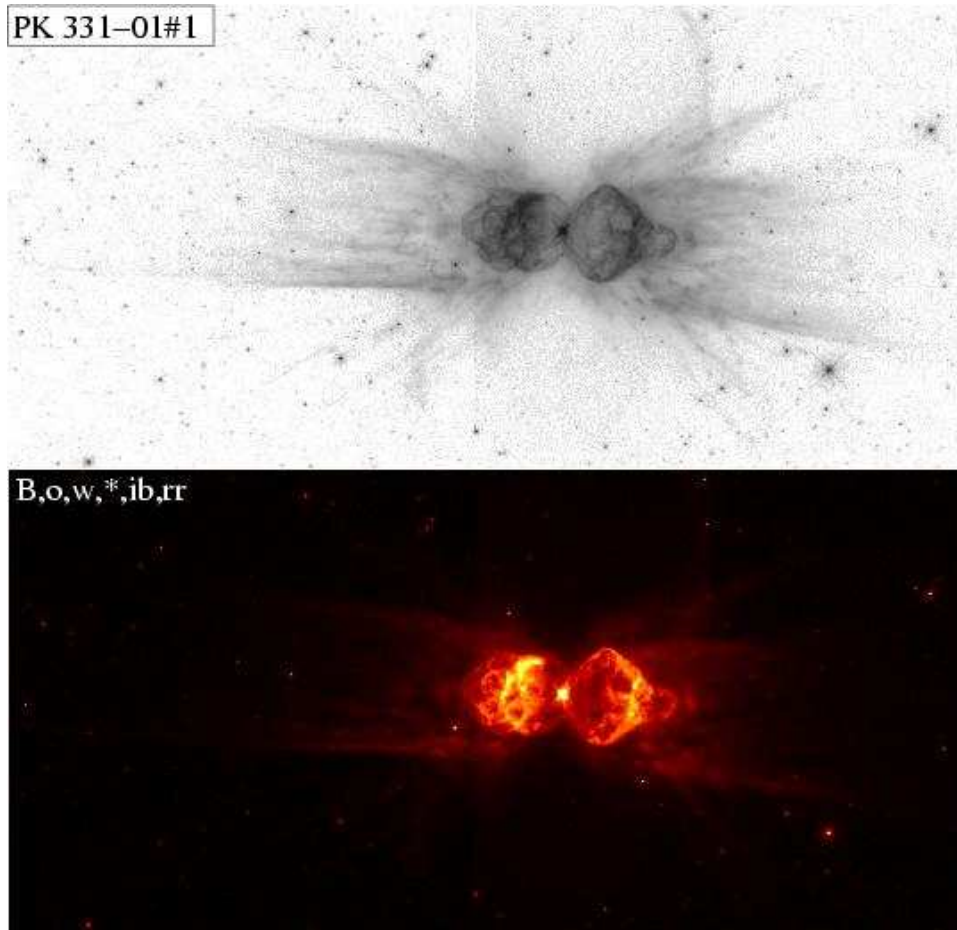
Fig. 22.— As in Fig 1., but for PK 331-01#1.
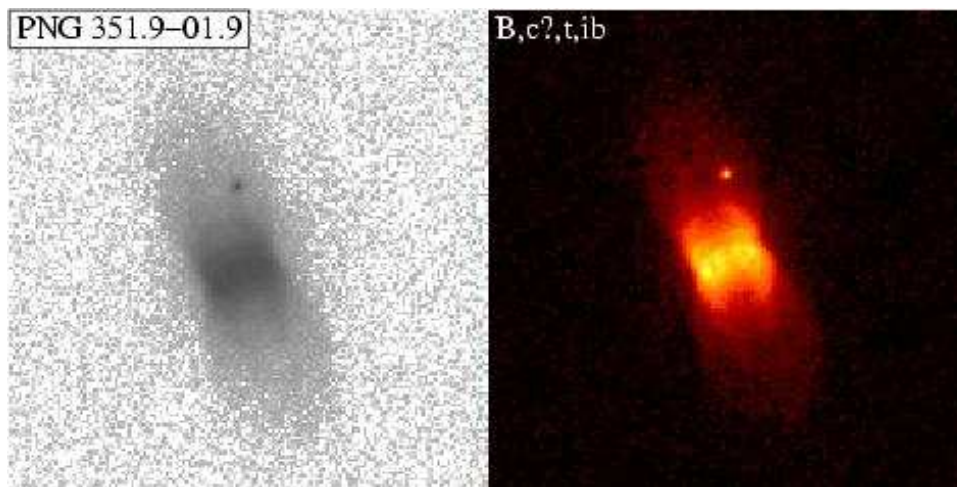
Fig. 23.— As in Fig 1., but for PNG 351.9-01.9.
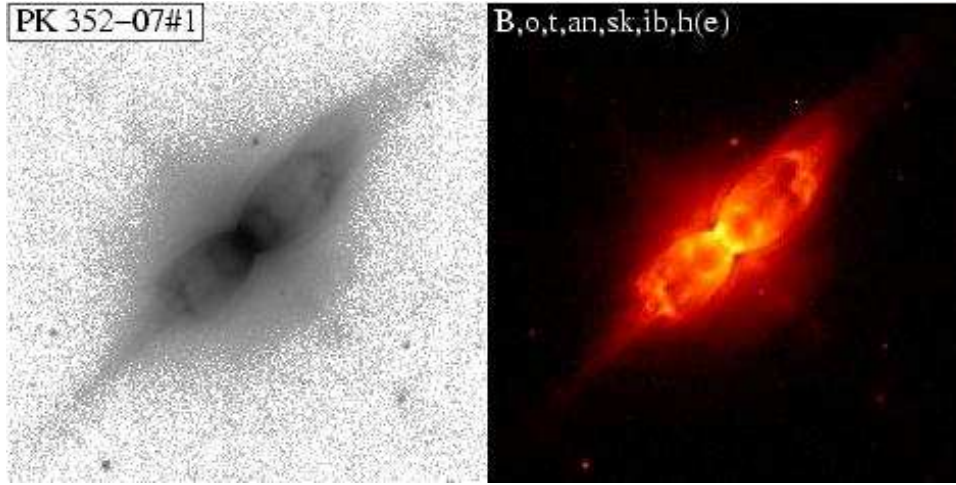
Fig. 24.— As in Fig 1., but for PK 352-07#1.
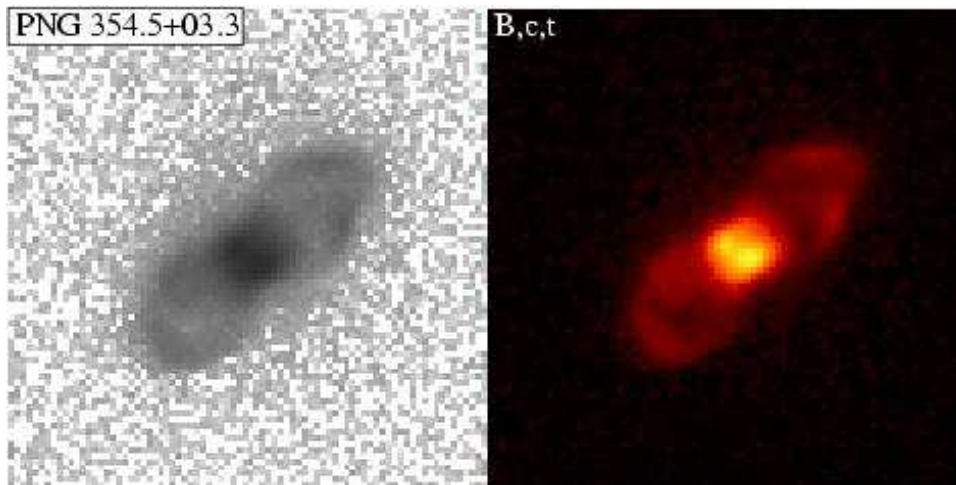
Fig. 25.— As in Fig 1., but for PNG354.5+03.3.

PNG 355.4−02.4

B,o?,bcr(o)?
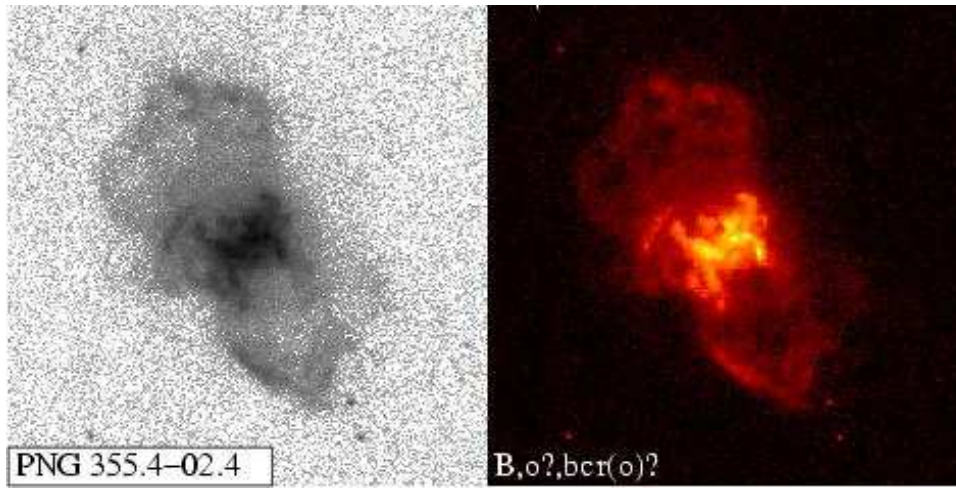
Fig. 26.— As in Fig 1., but for PNG 355.4-02.4.

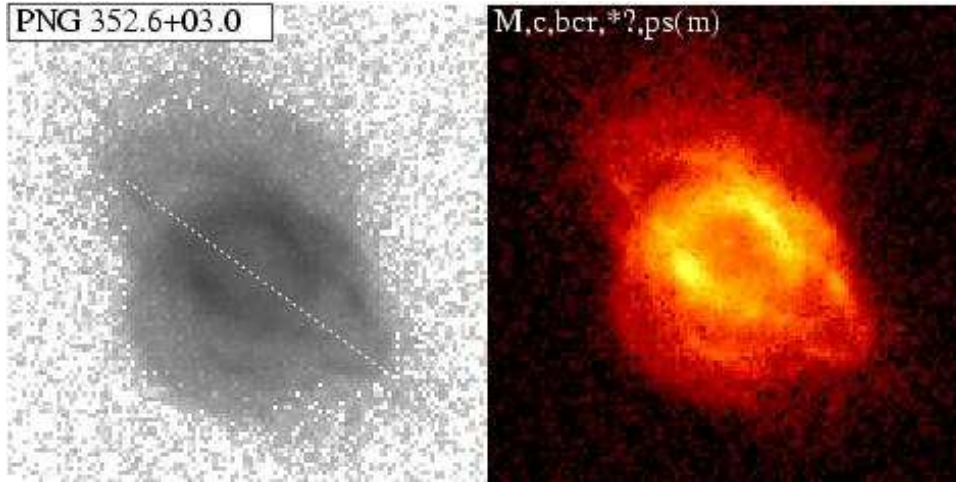PK 355−03#3

B,c,bcr(o),h
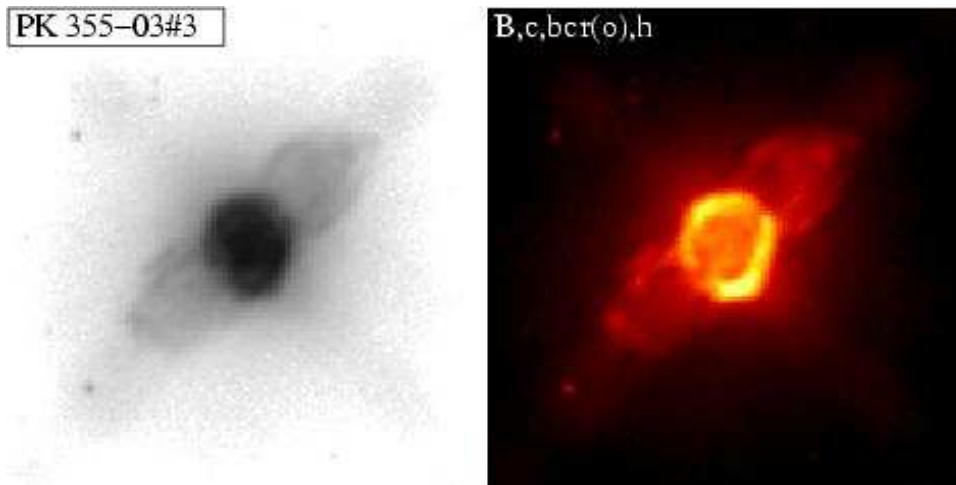
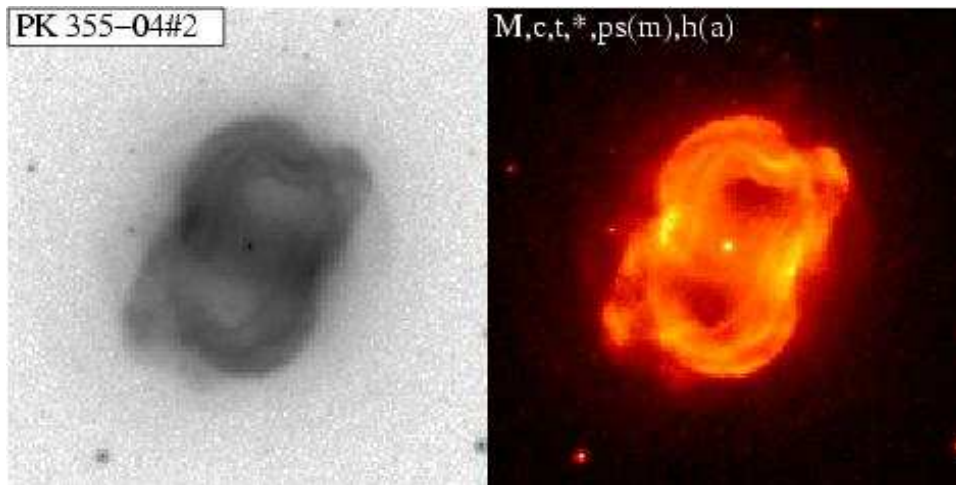Fig. 27.— As in Fig 1., but for PK 355-03#3.
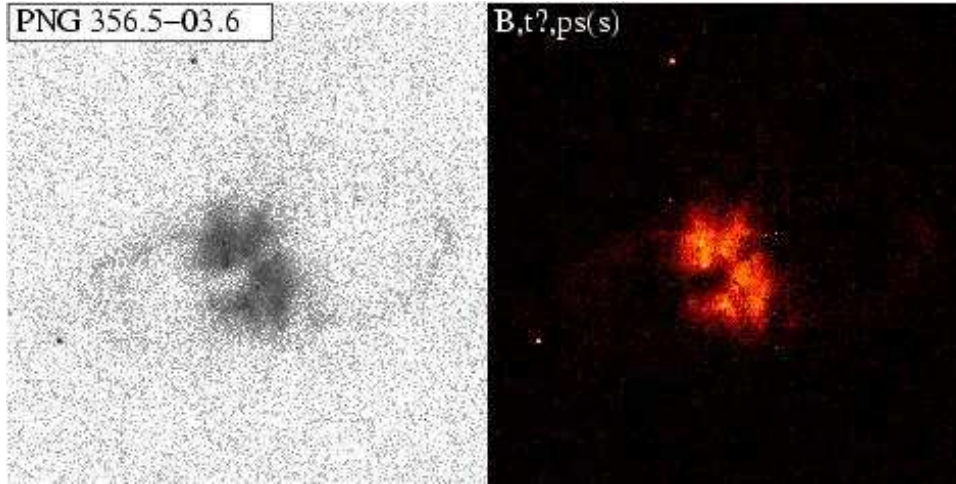
Fig. 28.— As in Fig 1., but for PNG356.5-03.6.
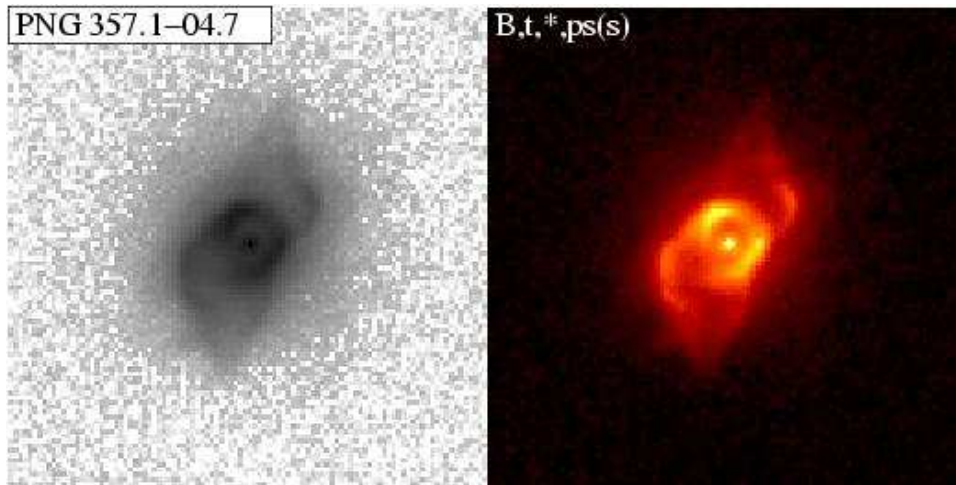
Fig. 29.— As in Fig 1., but for PNG357.1-04.7.
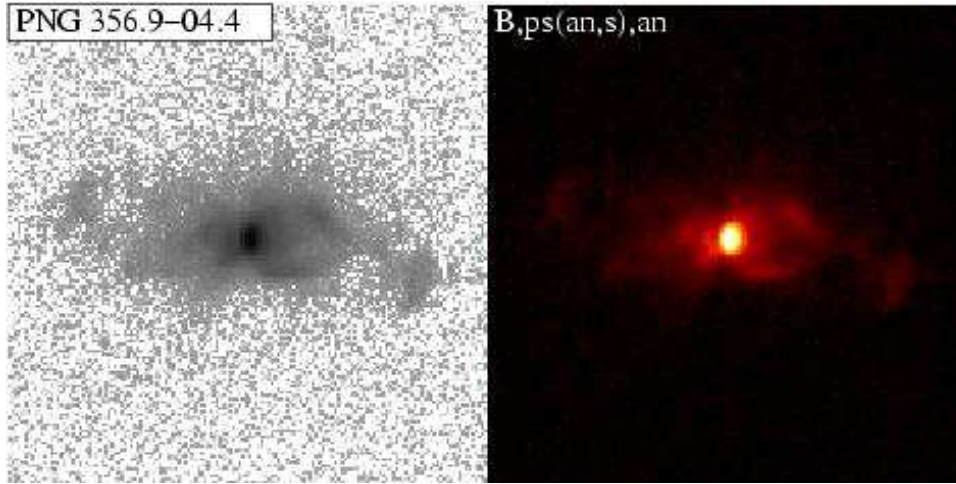
Fig. 30.— As in Fig 1., but for PNG356.9-04.4.

PK 002−03#3   M,c,t,*,ps(m),h(a)
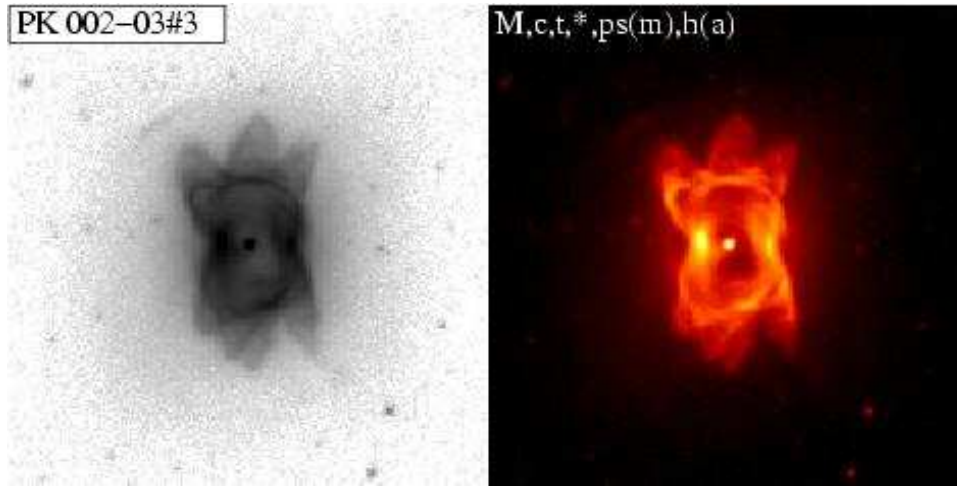
Fig. 31.— As in Fig 1., but for PK 002-03#3 (adapted from Sahai 2000).

PK 002−04#1   M,bcr(o),ps(m),h(a)
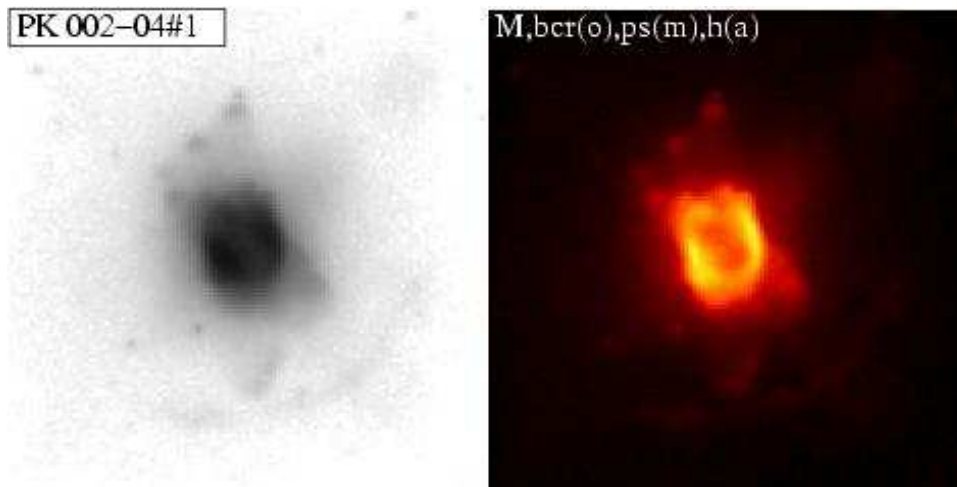
Fig. 32.— As in Fig 1., but for PK 002-04#1.
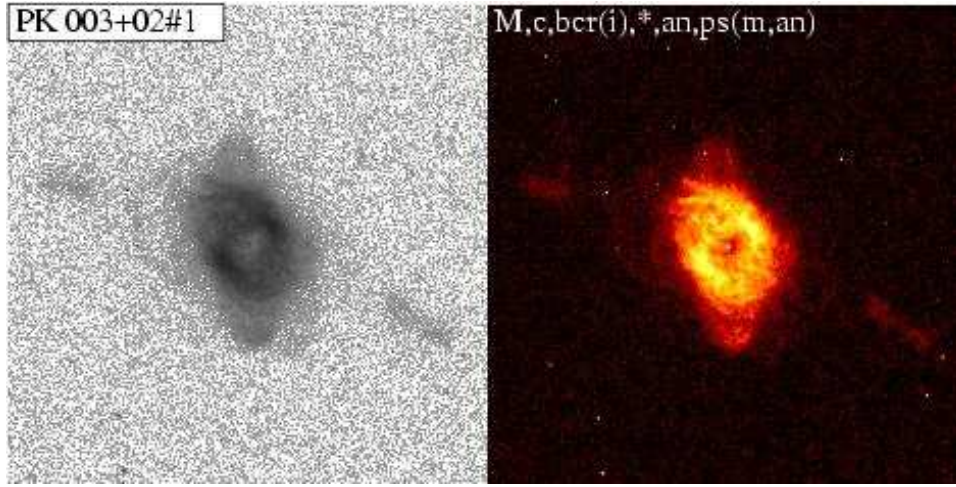
Fig. 33.— As in Fig 1., but for PK 003+02#1.
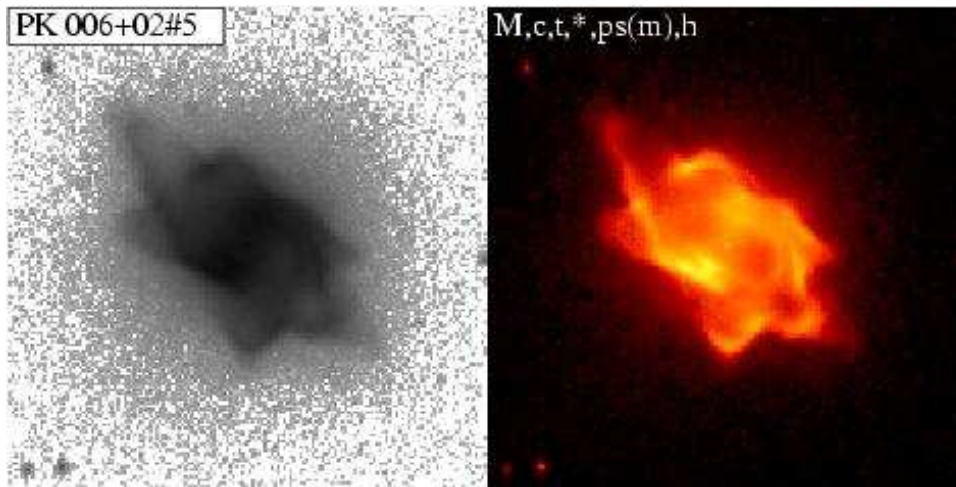
Fig. 34.— As in Fig 1., but for PK 006+02#5.

PK 008−07#2   M,c,bcr?,*,ib,h
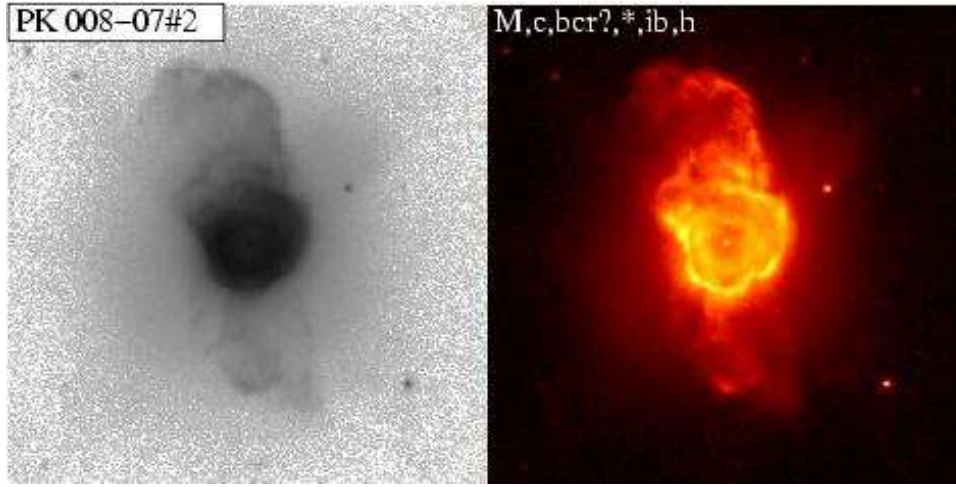
Fig. 35.— As in Fig 1., but for PK 008-07#2.

PK 019−05#1   M,c,bcr,*,ml,ib,ps(s),h
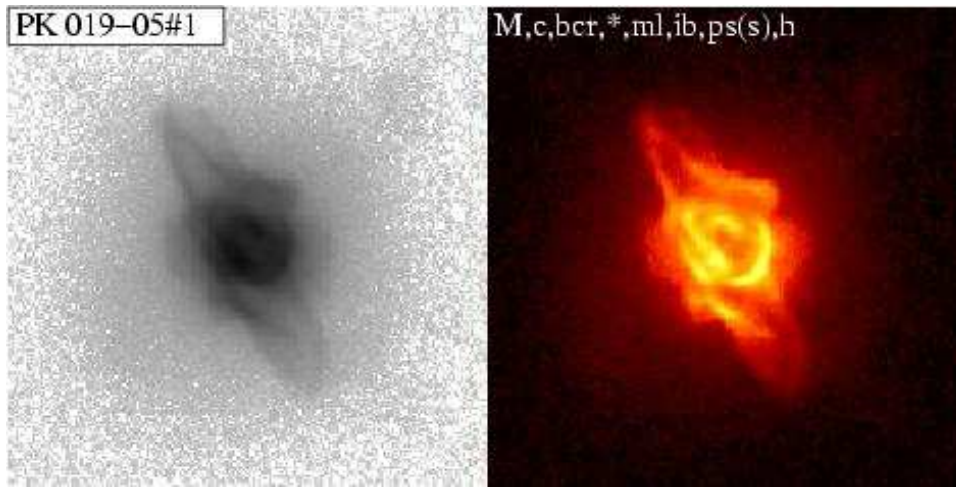
Fig. 36.— As in Fig 1., but for PK 019-05#1.
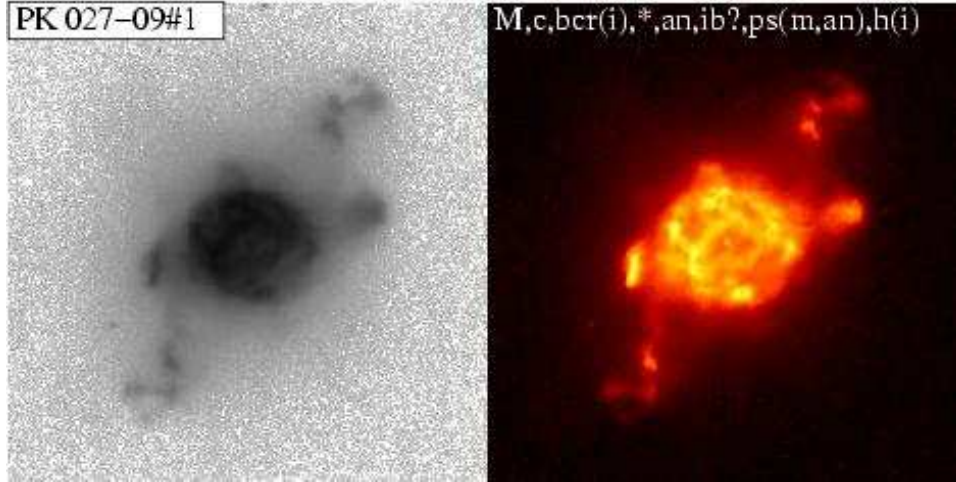
Fig. 37.— As in Fig 1., but for PK 027-09#1.
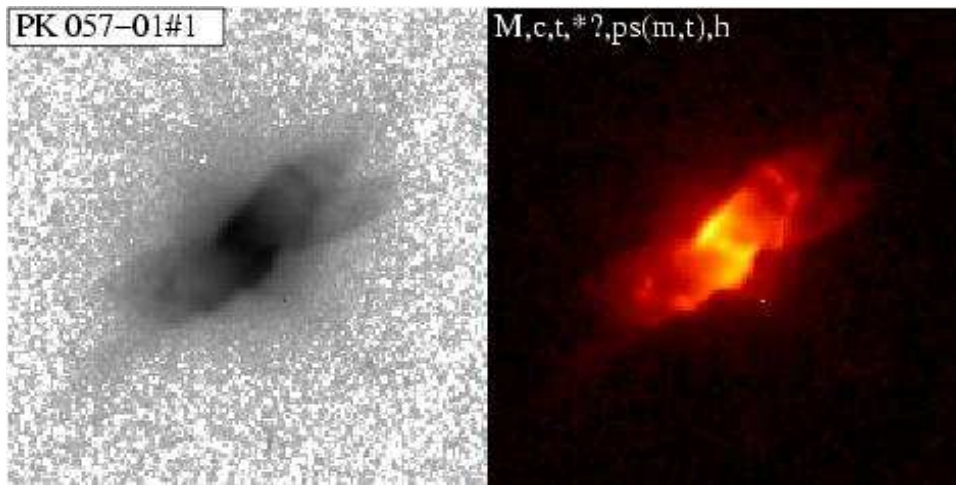
Fig. 38.— As in Fig 1., but for PK 057-01#1.
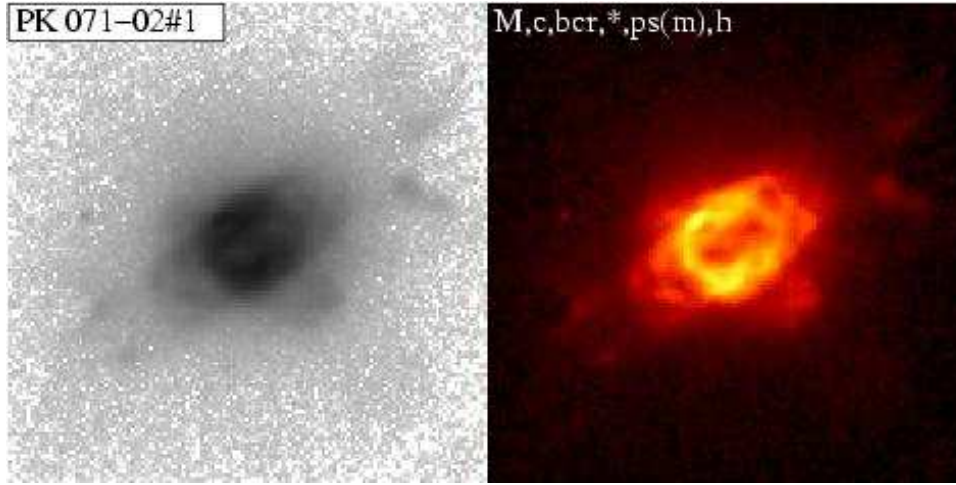
Fig. 39.— As in Fig 1., but for PK 071-02#1.


Fig. 40.— As in Fig 1., but for PK 082+07#1.

Fig. 41.— As in Fig 1., but for PK 089-05#1.

Fig. 42.— As in Fig 1., but for PK 100-08#1 (adapted from ST98).

Fig. 43.— As in Fig 1., but for PK 285-02#1 (adapted from Sahai 2000).

Fig. 44.— As in Fig 1., but for PK 300-02#1.

PK 320–09#1   M,c,*,pr,ps(s,m),h

Fig. 45.— As in Fig 1., but for PK 320-09#1 (adapted from ST98).

PK 321+03#1   M,c,w,*,h

Fig. 46.— As in Fig 1., but for PK 321+03#1.

Fig. 47.— As in Fig 1., but for PNG352.6+03.0.

Fig. 48.— As in Fig 1., but for PK 355-04#2.

PNG 358.5−04.2

M,c,t,an,ml,ps(m,an,s)
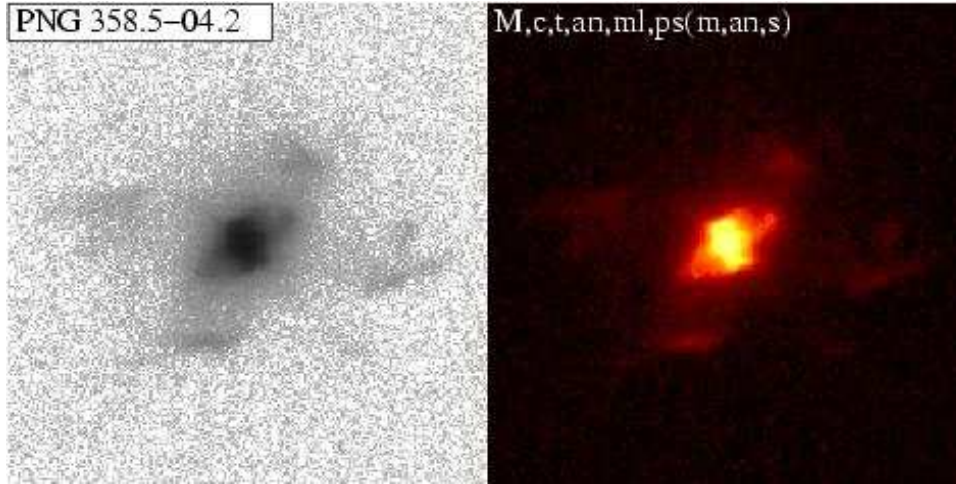
Fig. 49.— As in Fig 1., but for PNG358.5-04.2.

PNG 358.9+03.4

M,c,t,ps(m)
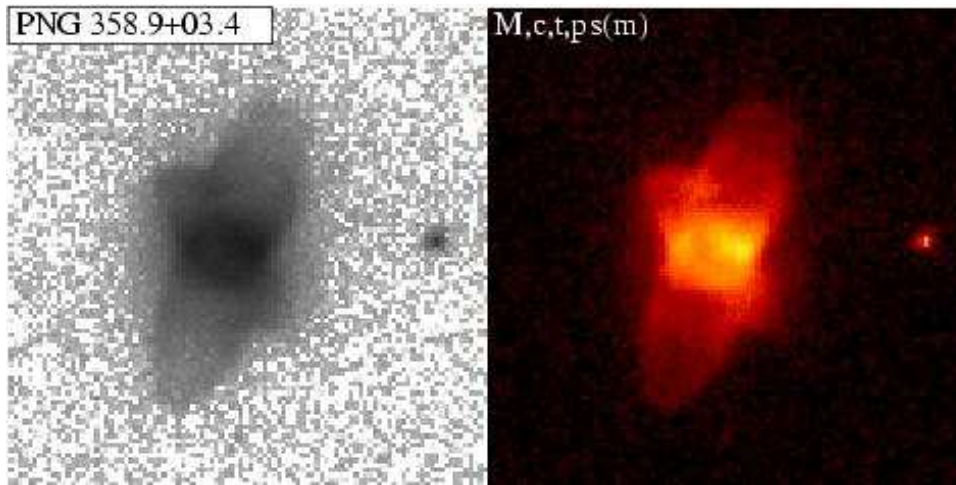
Fig. 50.— As in Fig 1., but for PNG358.9+03.4.

PK 358−00#2   M,c,bcr(c),*,ir,h(i)
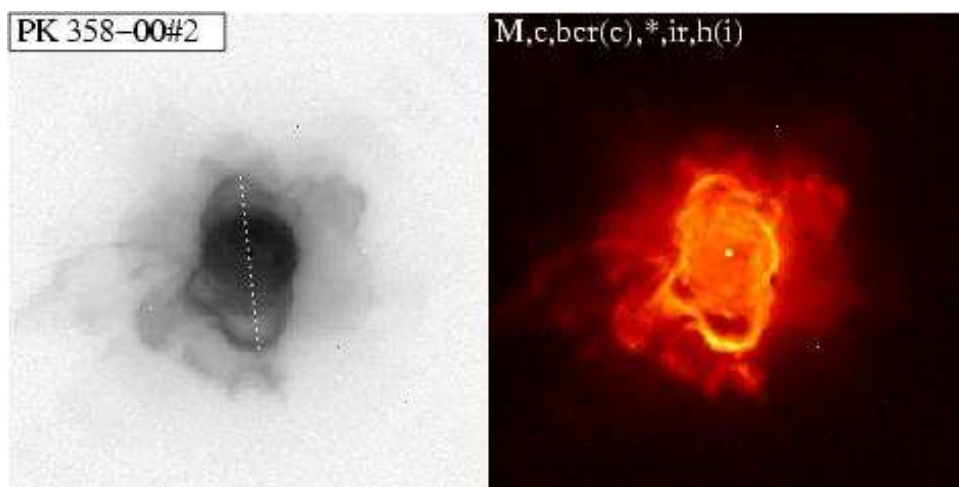
Fig. 51.— As in Fig 1., but for PK 358-00#2 (adapted from ST98).
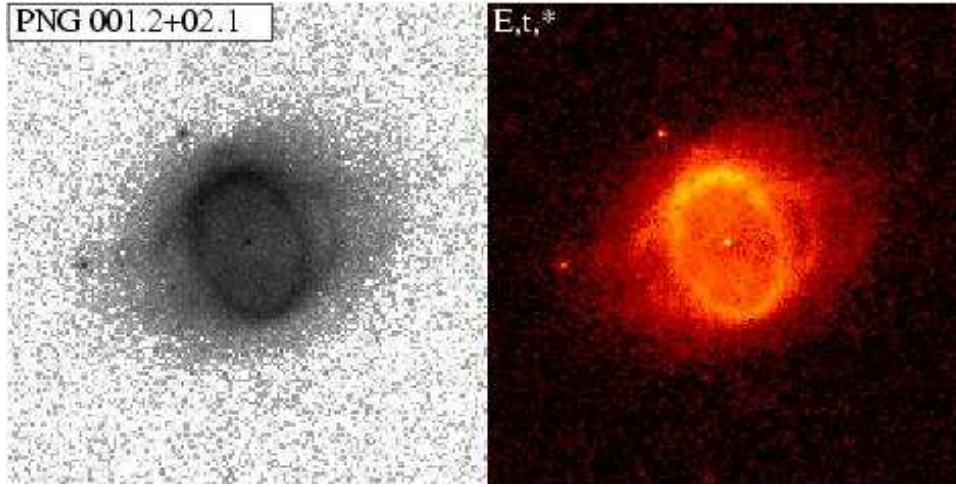
Fig. 52.— As in Fig 1., but for PNG001.2+02.1.
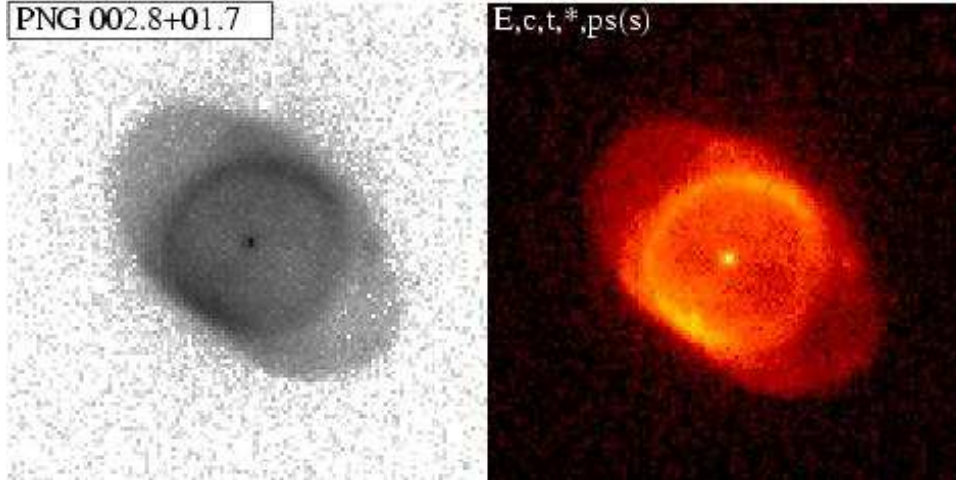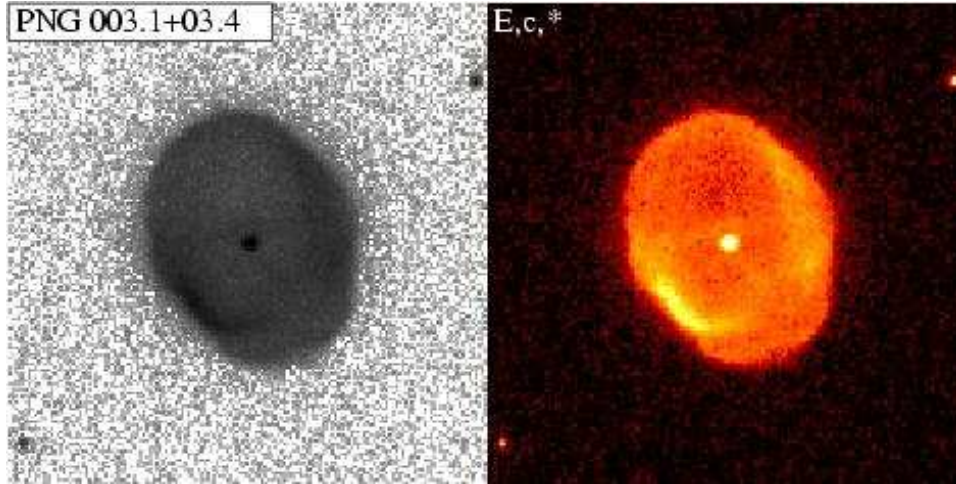

Fig. 53.— As in Fig 1., but for PNG002.8+01.7.

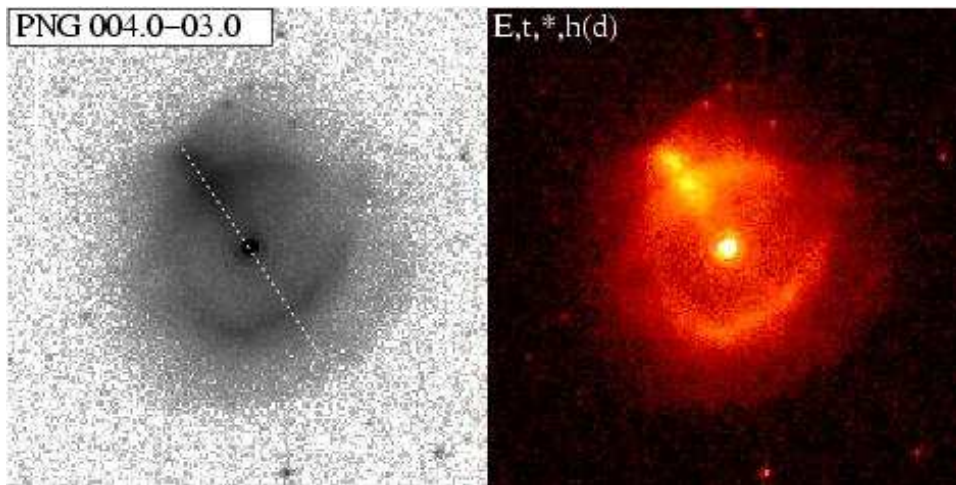Fig. 54.— As in Fig 1., but for PNG003.1+03.4.
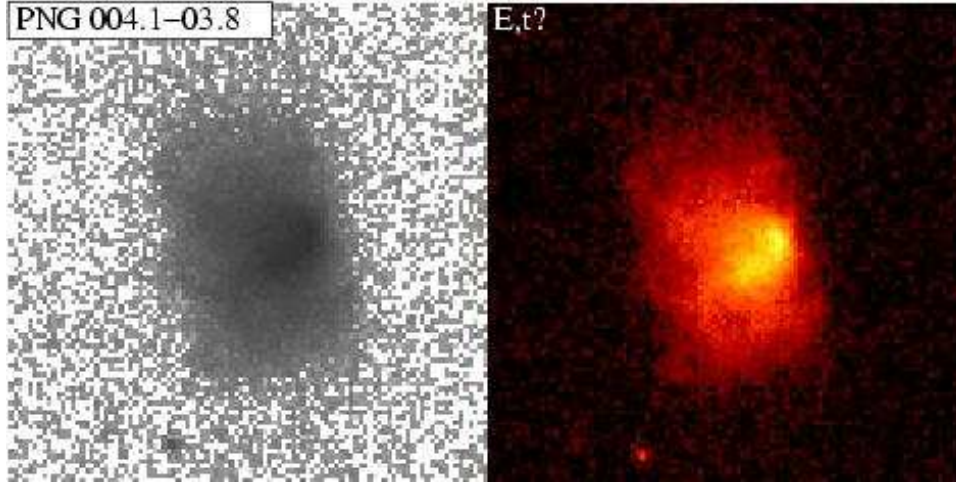

Fig. 55.— As in Fig 1., but for PNG004.0-03.0.

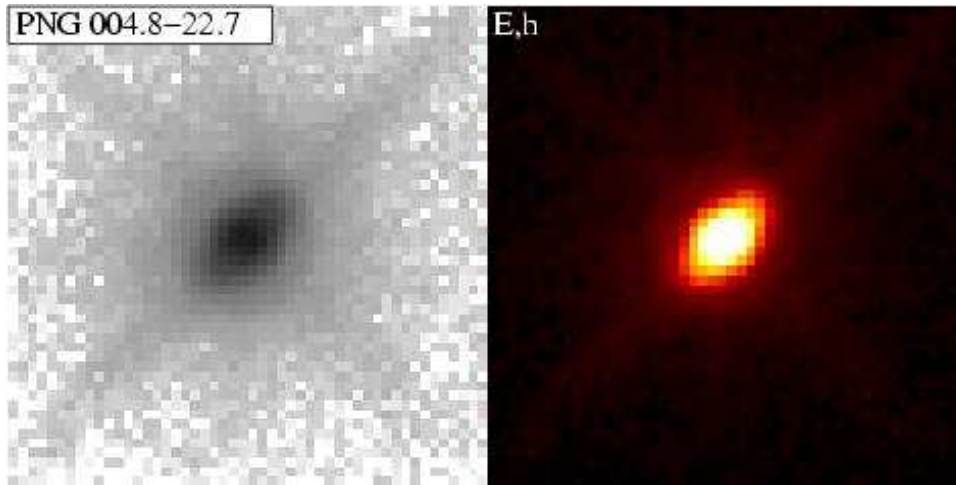Fig. 56.— As in Fig 1., but for PNG004.1-03.8.

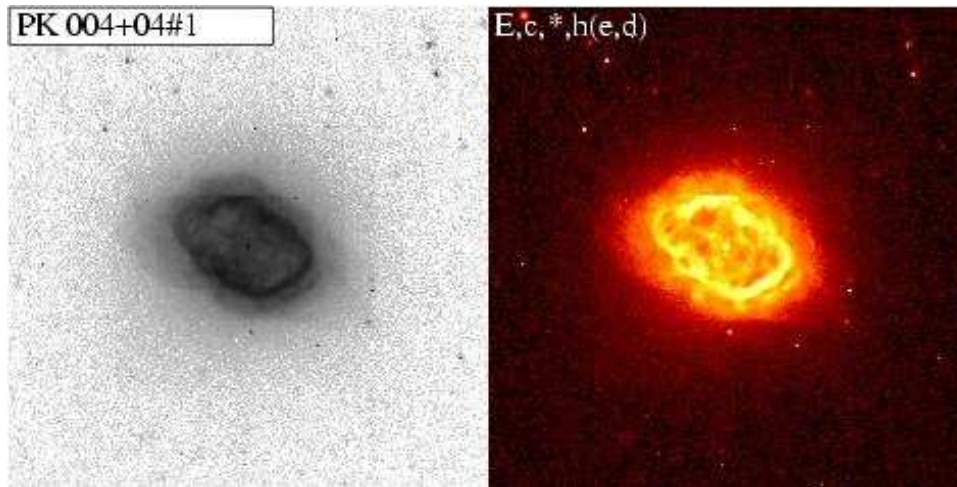Fig. 57.— As in Fig 1., but for PNG004.8-22.7.

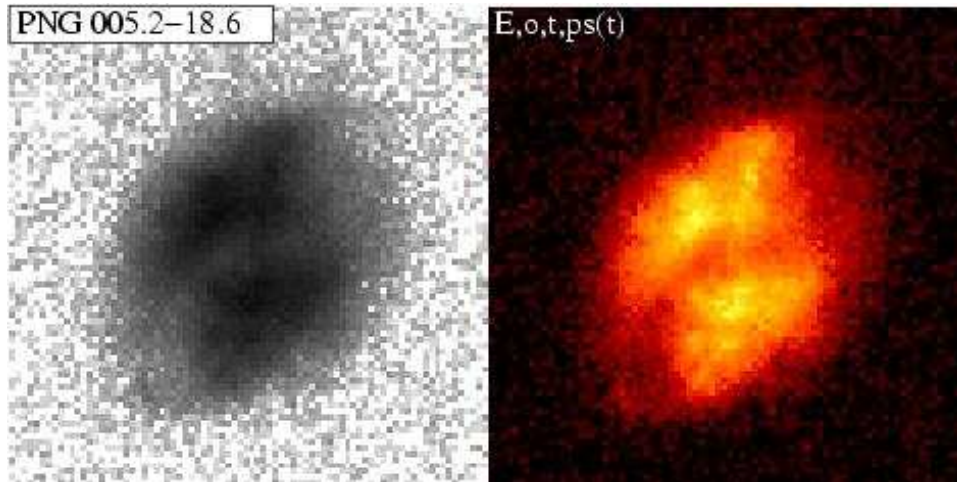Fig. 58.— As in Fig 1., but for PK 004+04#1.
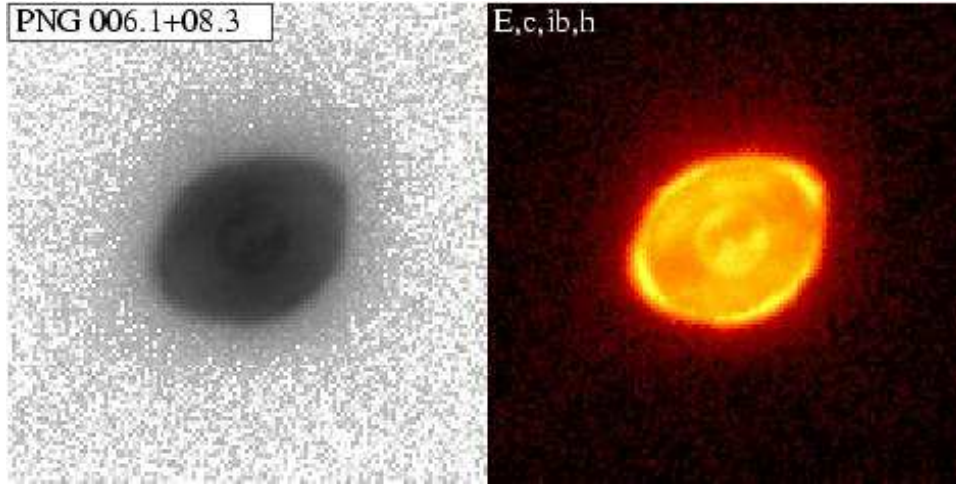

Fig. 59.— As in Fig 1., but for PNG005.2-18.6.

Fig. 60.— As in Fig 1., but for PNG006.1+08.3.
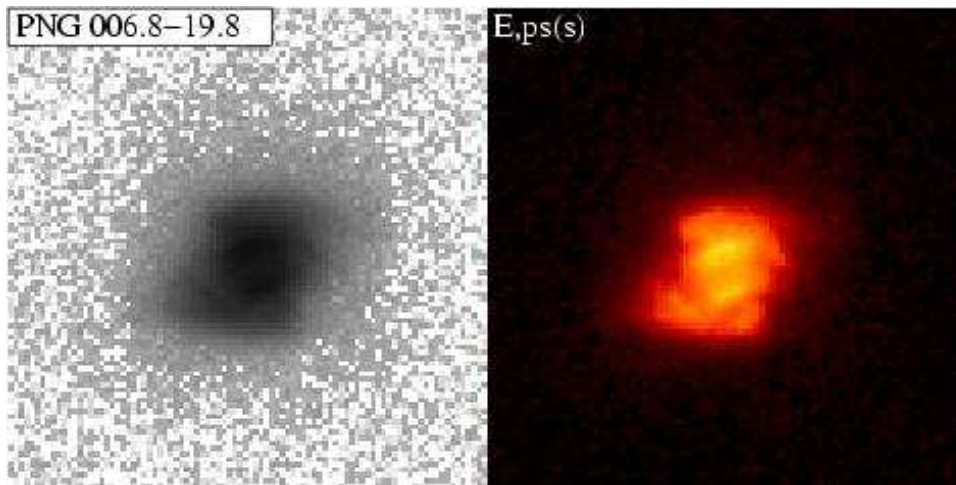
Fig. 61.— As in Fig 1., but for PNG006.8-19.8.
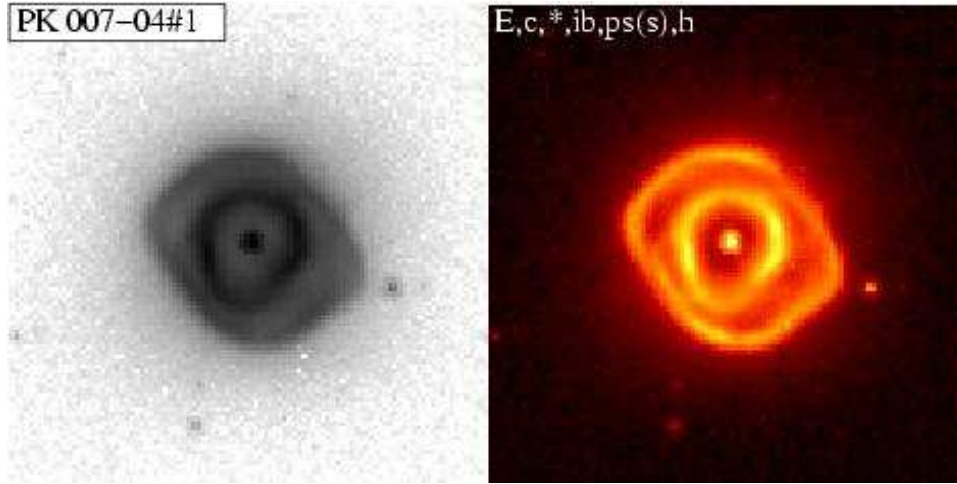
Fig. 62.— As in Fig 1., but for PK 007-04#1.
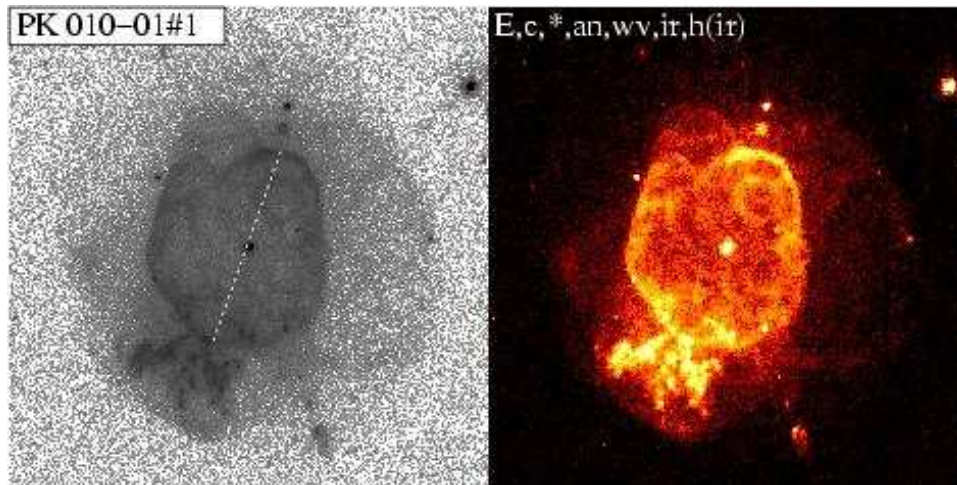
Fig. 63.— As in Fig 1., but for PK 010-01#1 and the F658N ([NII]) filter.

Fig. 64.— As in Fig 1., but for PK 038+12#1.
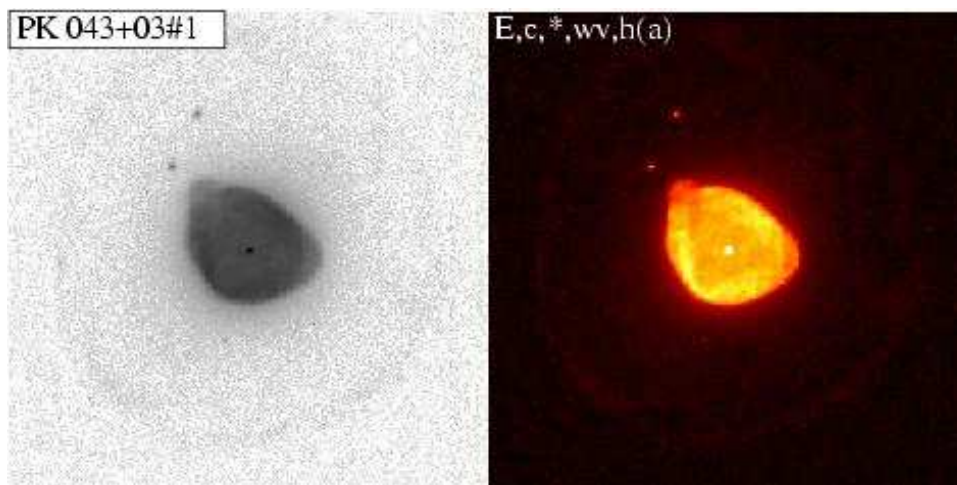
Fig. 65.— As in Fig 1., but for PK 043+03#1.

PK 051−03#1

E,bcr,*,ib,ps(s)

Fig. 66.— As in Fig 1., but for PK 051-03#1.

PK 064+05#1

E,c,*,rr,an?,h(e,d)

Fig. 67.— As in Fig 1., but for PK 064+05#1 (adapted from ST98).
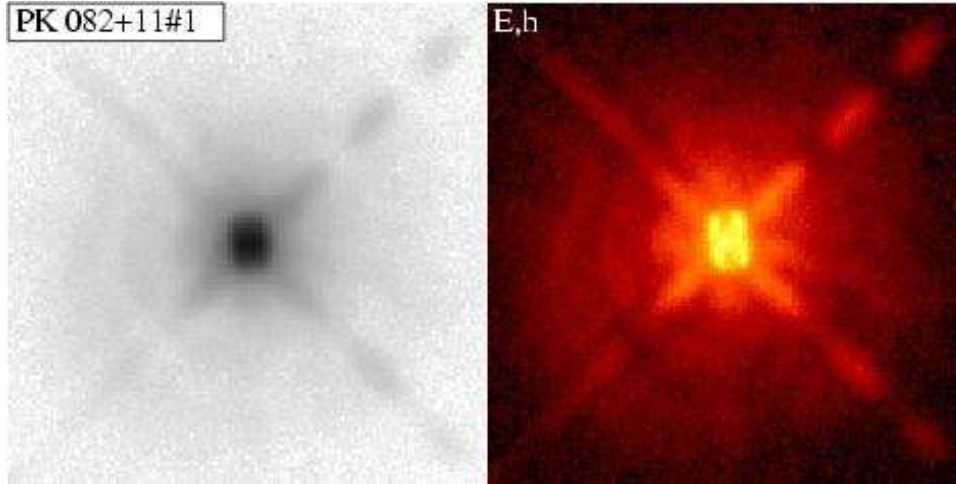
Fig. 68.— As in Fig 1., but for PK 082+11#1.
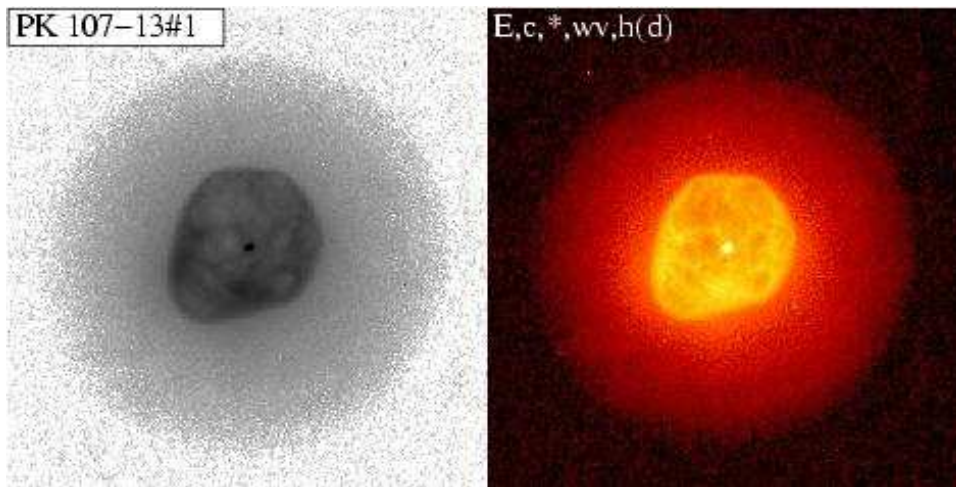
Fig. 69.— As in Fig 1., but for PK 107-13#1.

Fig. 70.— As in Fig 1., but for PK 147-02#1.

Fig. 71.— As in Fig 1., but for PK 215-24#1.

Fig. 72.— As in Fig 1., but for PK 226-03#1.

Fig. 73.— As in Fig 1., but for PK 232-04#1.

– 84 –

Fig. 74.— As in Fig 1., but for PK 235-01#1.
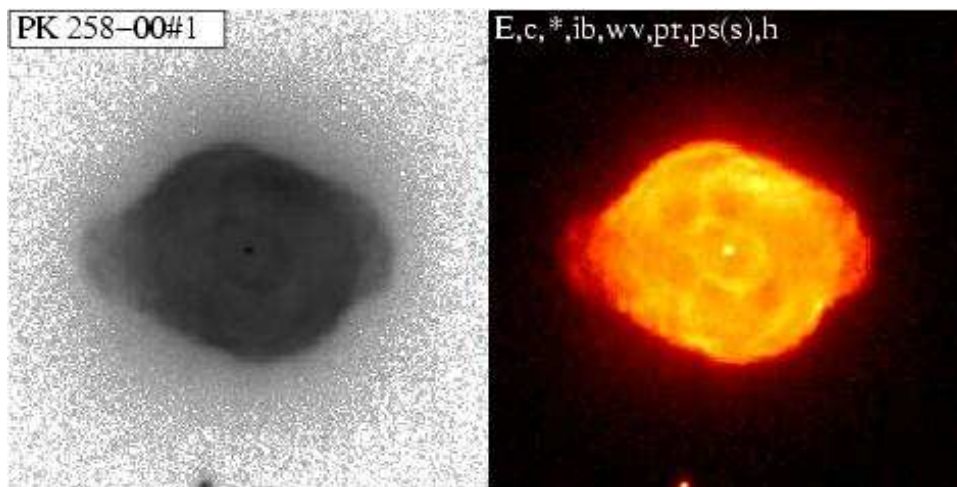
Fig. 75.— As in Fig 1., but for PK 258-00#1.
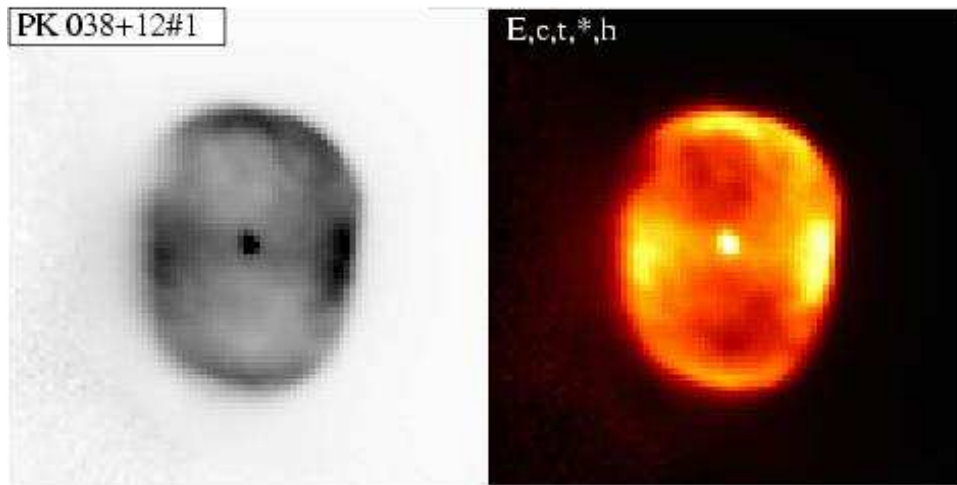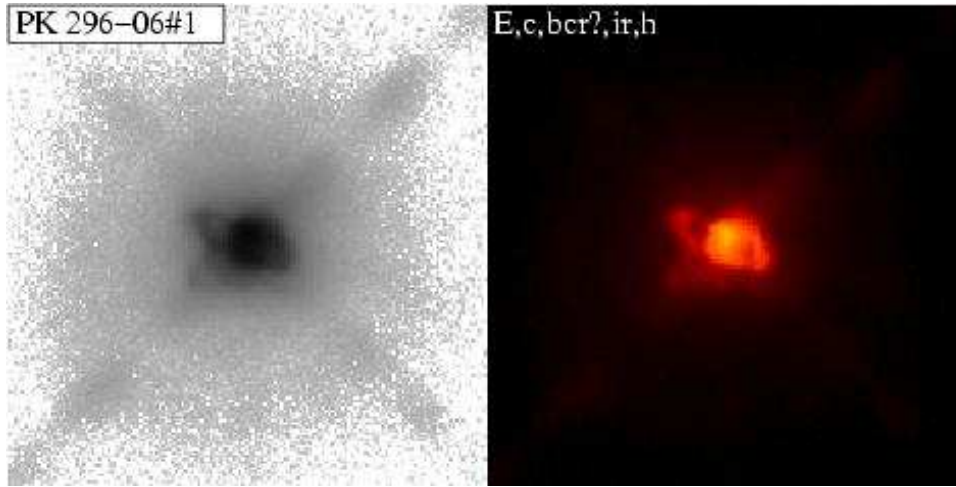
Fig. 76.— As in Fig 1., but for PK 296-06#1.
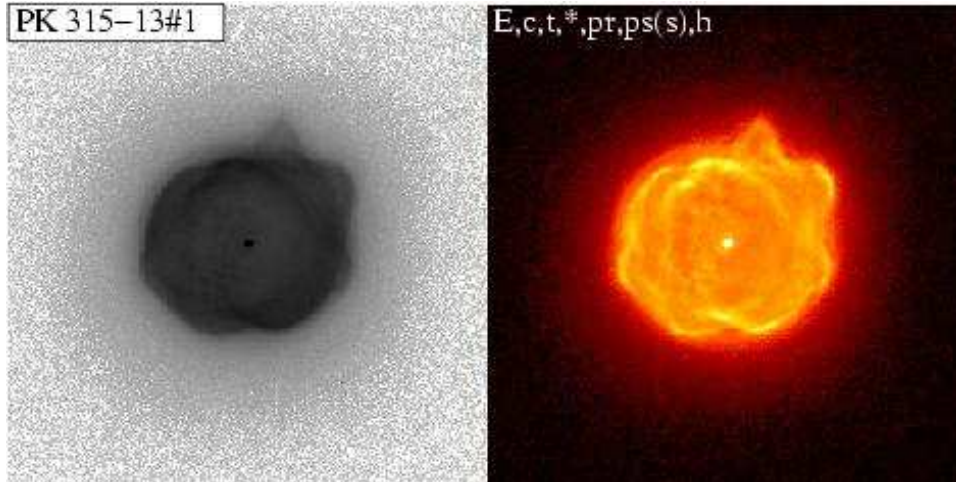
Fig. 77.— As in Fig 1., but for PK 315-13#1 (adapted from ST98).
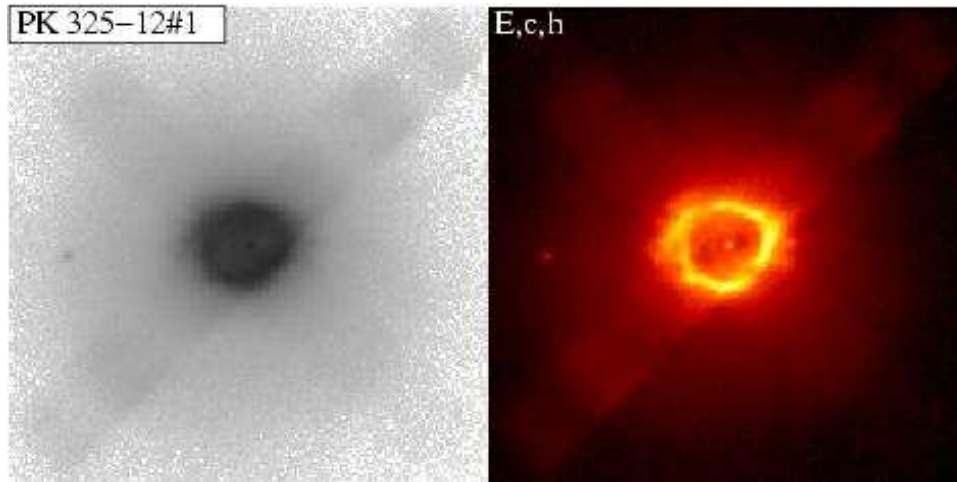
Fig. 78.— As in Fig 1., but for PK 325-12#1.
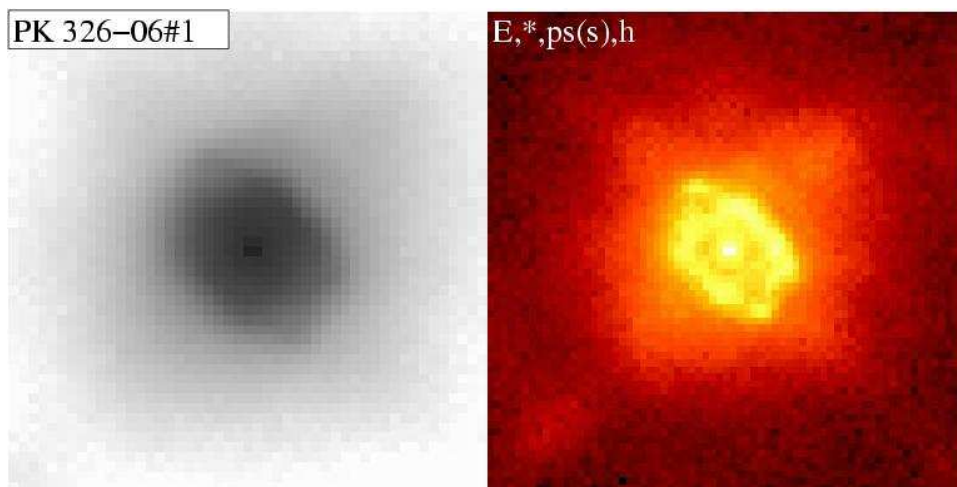
Fig. 79.— As in Fig 1., but for PK 326-06#1.

PK 327-02#1

E?,c,*,rr,ps(s),h
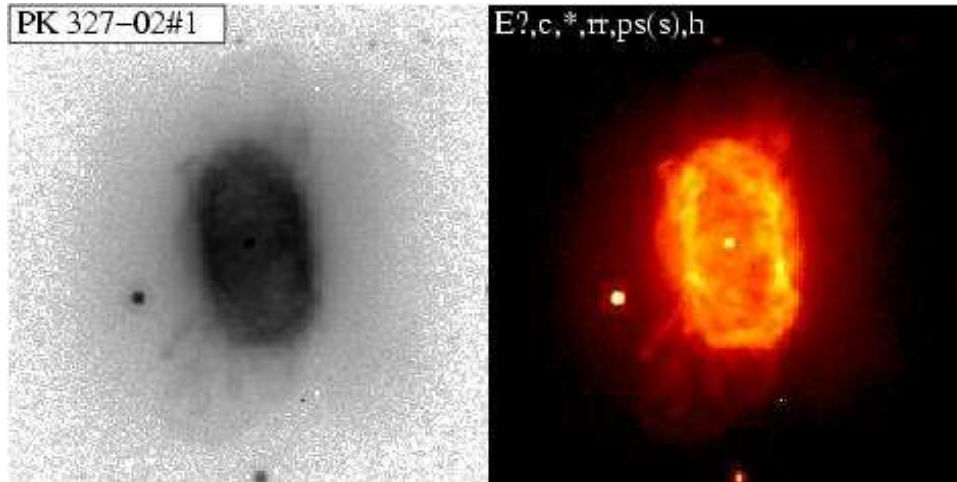
Fig. 80.— As in Fig 1., but for PK 327-02#1 (adapted from ST98).

PK 331-02#2

E,o,t,*?,an
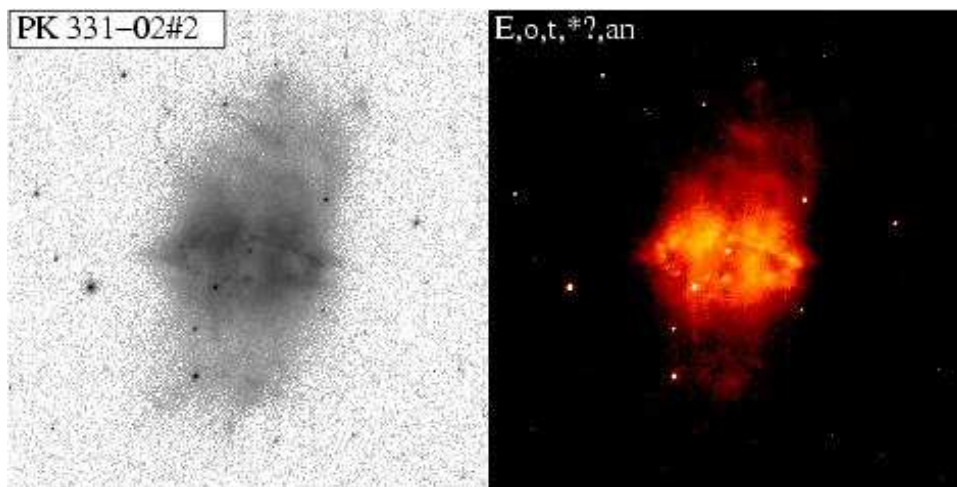
Fig. 81.— As in Fig 1., but for PK 331-02#2.
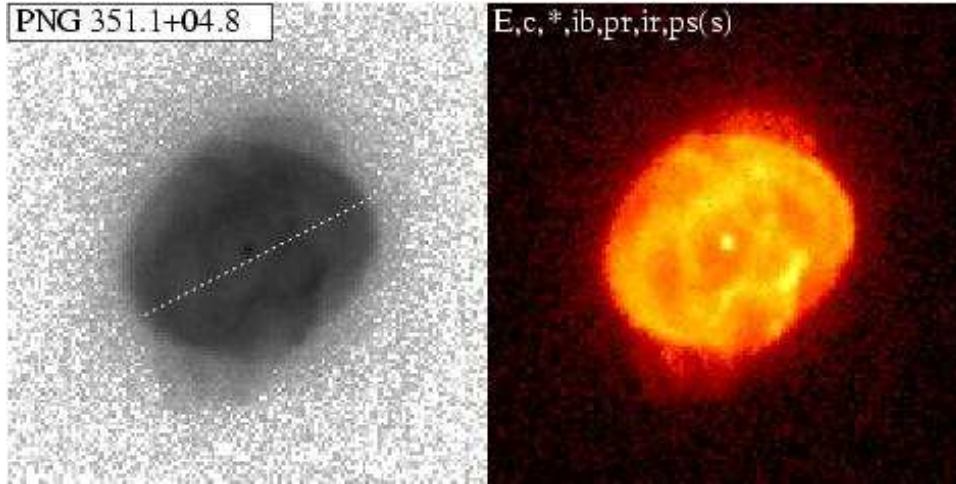
Fig. 82.— As in Fig 1., but for PNG351.1+04.8.
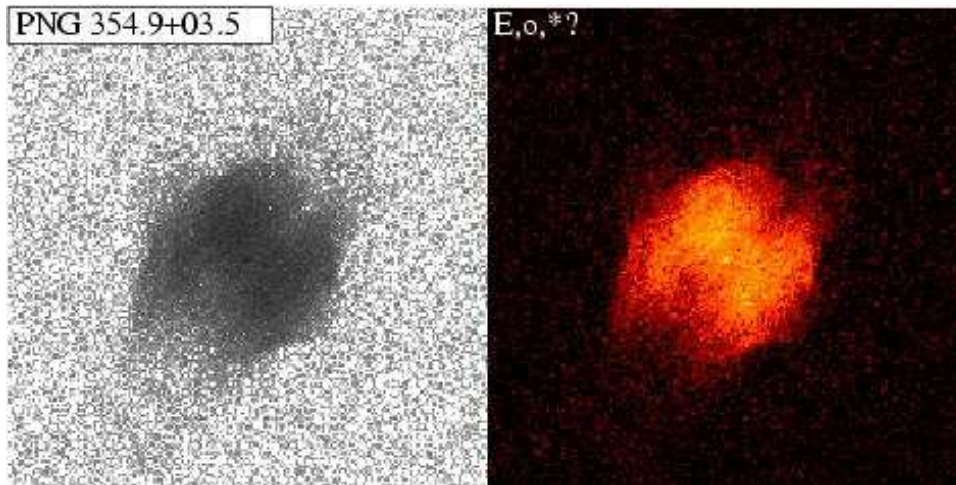
Fig. 83.— As in Fig 1., but for PNG354.9+03.5.
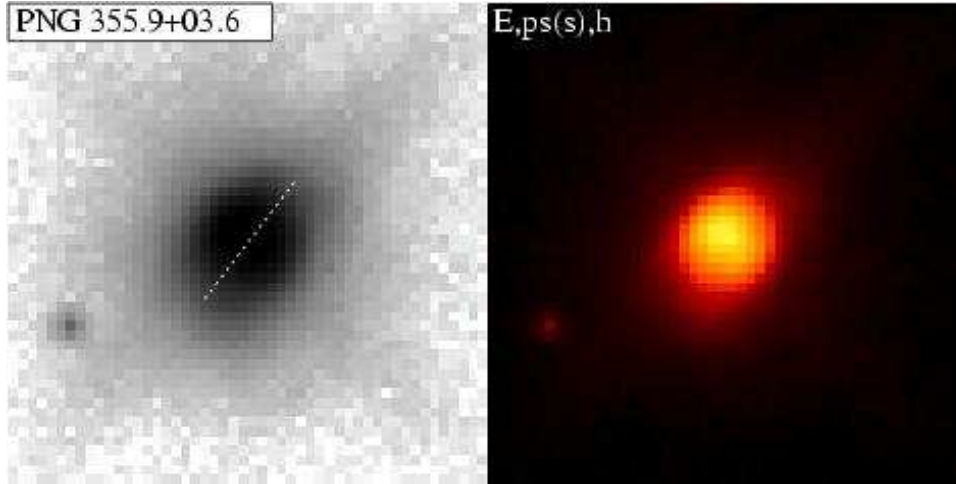
Fig. 84.— As in Fig 1., but for PNG355.9+03.6.
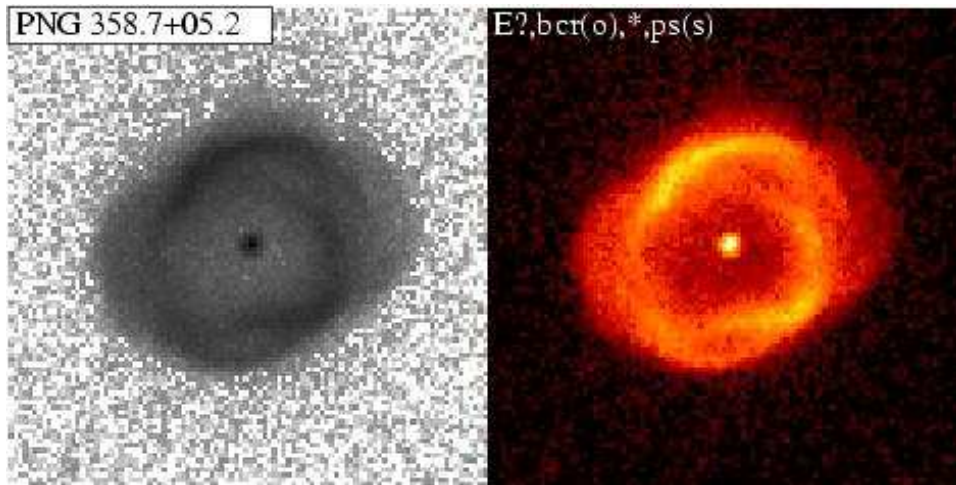
Fig. 85.— As in Fig 1., but for PNG358.7+05.2.
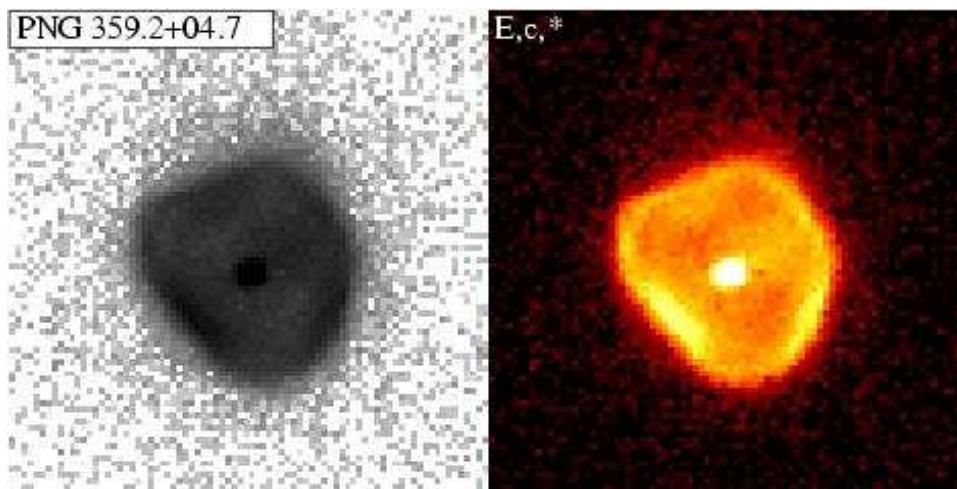
Fig. 86.— As in Fig 1., but for PNG359.2+04.7.
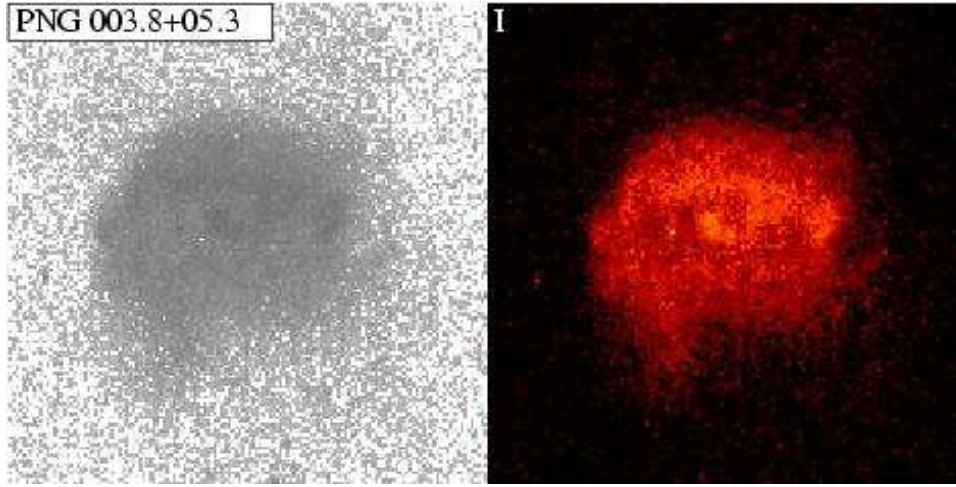
Fig. 87.— As in Fig 1., but for PNG003.8+05.3.
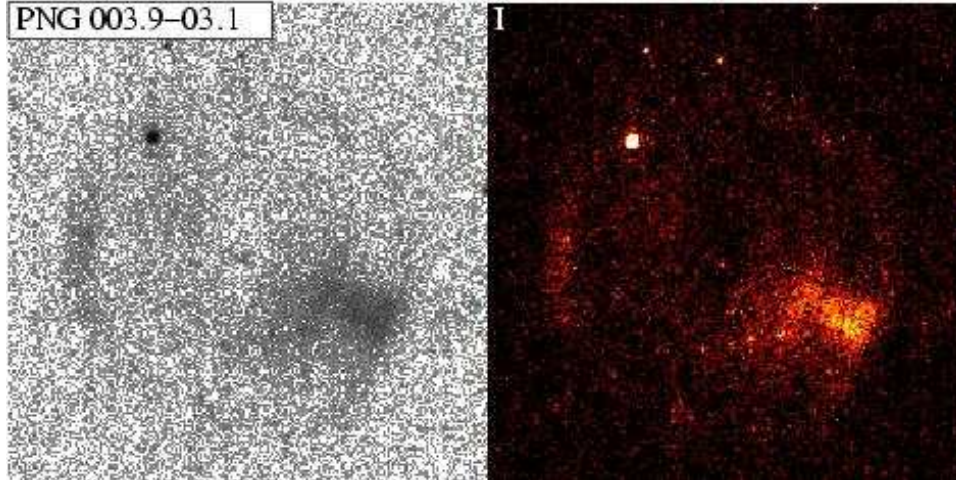
Fig. 88.— As in Fig 1., but for PNG003.9-03.1.
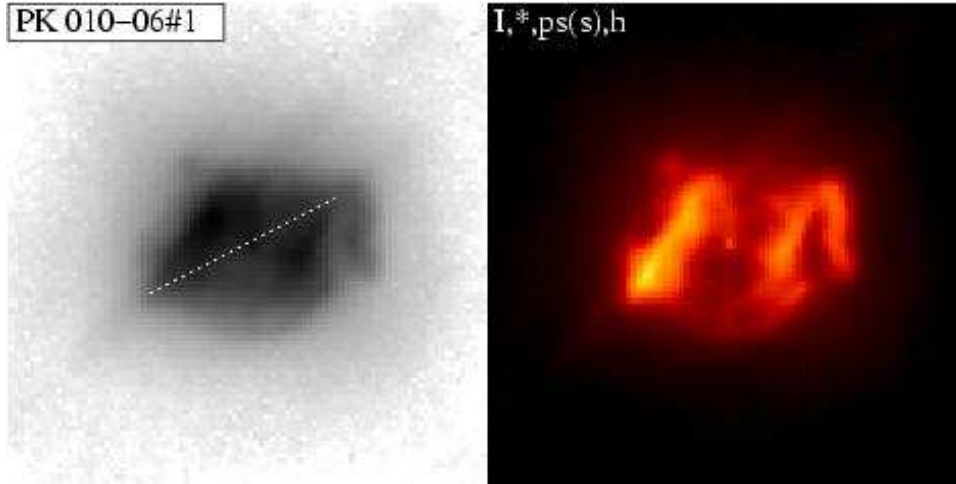
Fig. 89.— As in Fig 1., but for PK 010-06#1.
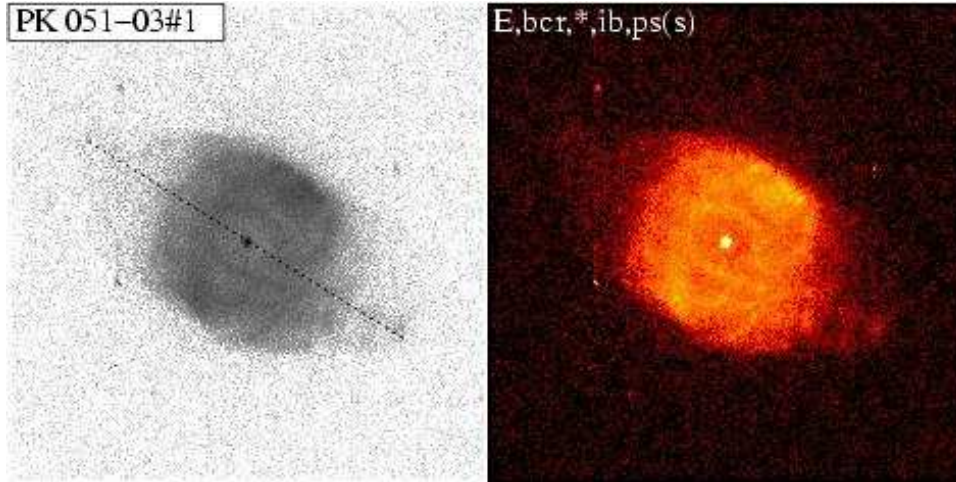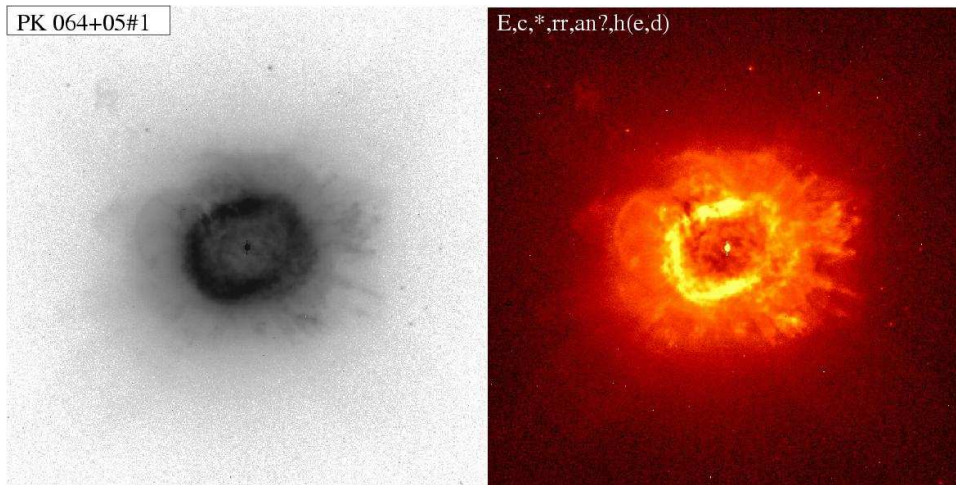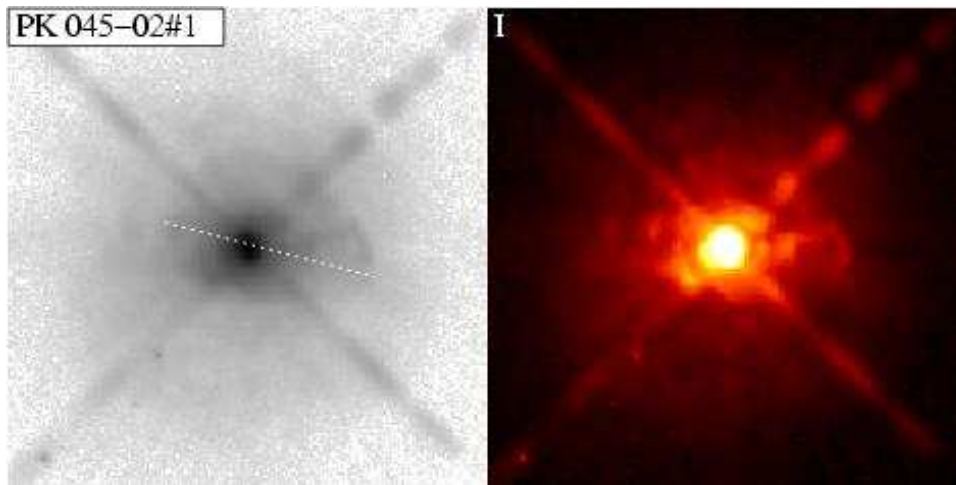

Fig. 90.— As in Fig 1., but for PK 045-02#1.
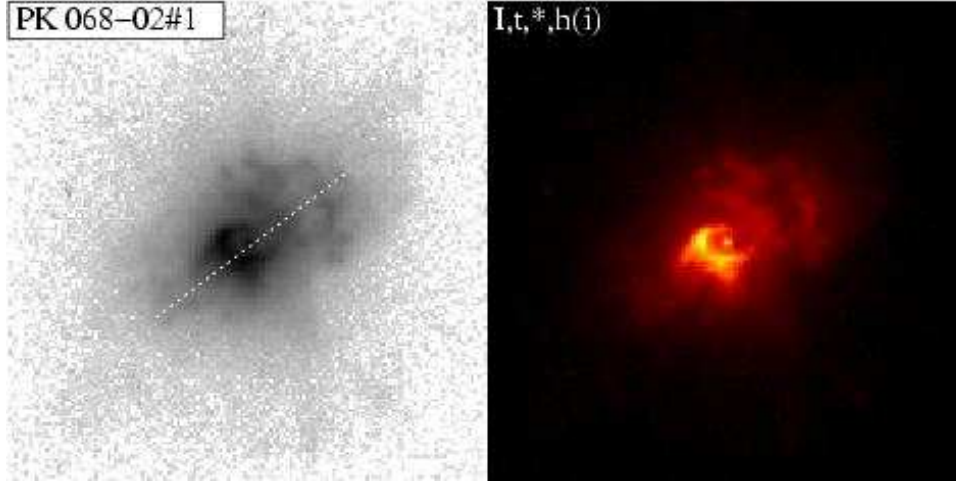
Fig. 91.— As in Fig 1., but for PK 068-02#1 (adapted from ST98).
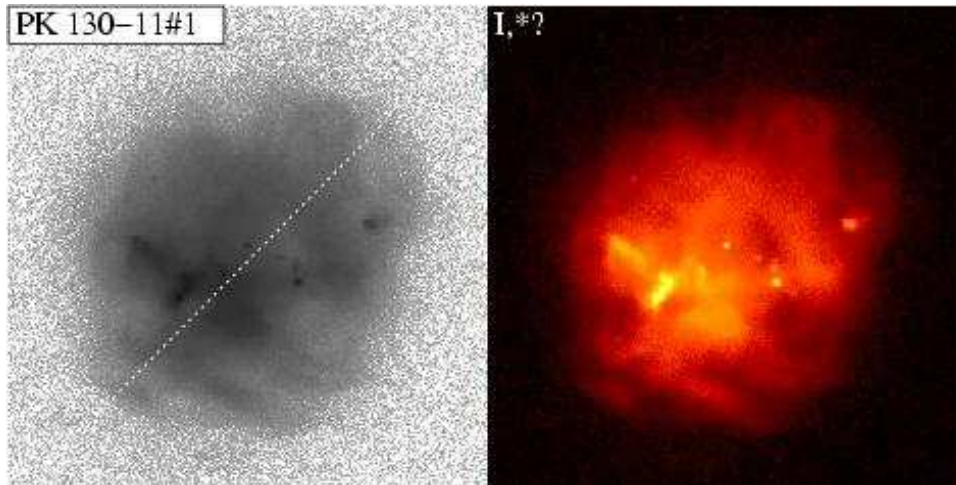
Fig. 92.— As in Fig 1., but for PK 130-11#1.
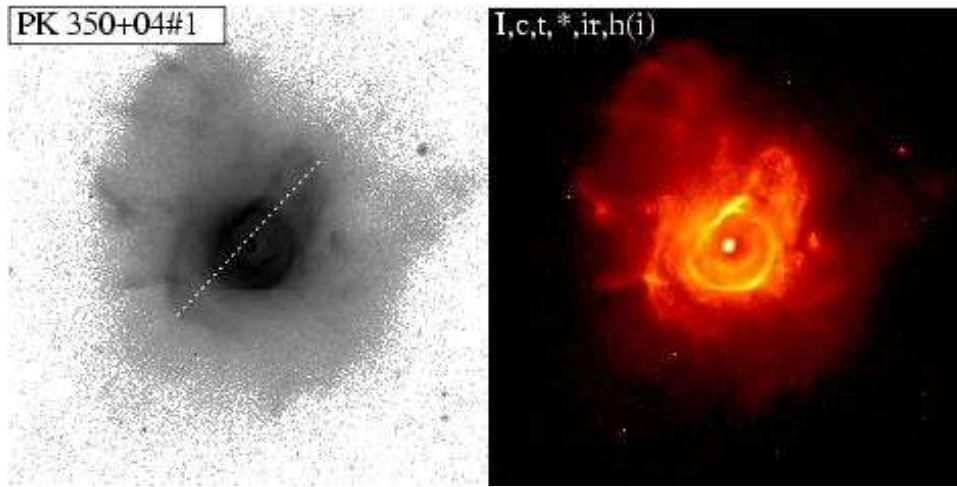
Fig. 93.— As in Fig 1., but for PK 350+04#1.
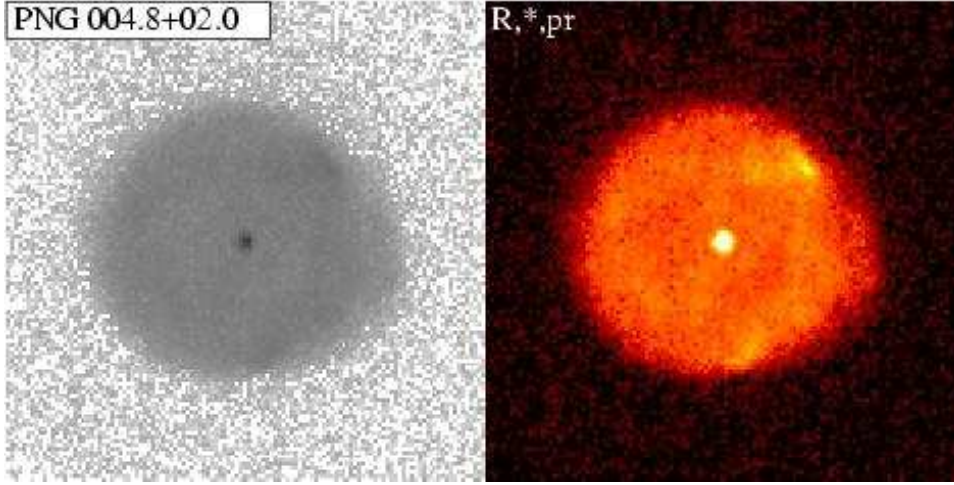
Fig. 94.— As in Fig 1., but for PNG004.8+02.0. We believe that the small departures from a round shape visible in the image are caused by a pair of small, diametrically-opposed protrusions along an axis oriented at $pa \sim -100 \, \mathrm{deg}$.
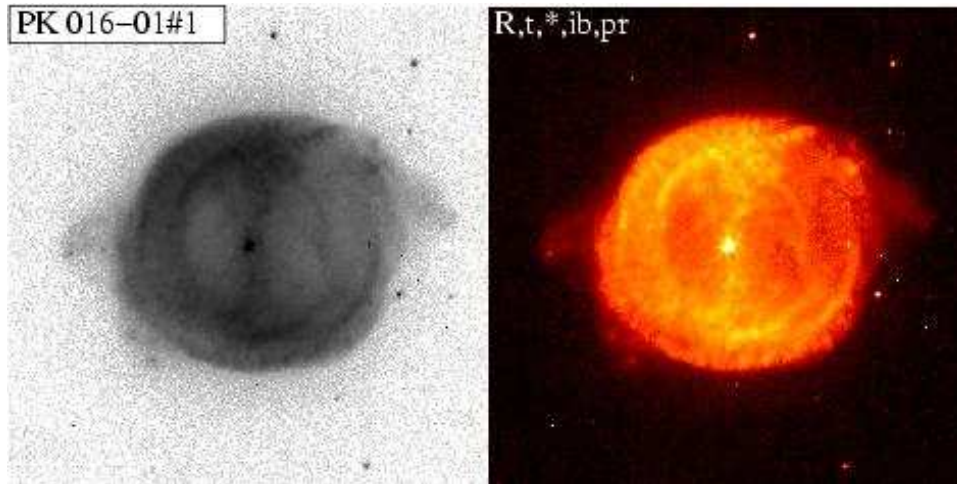
Fig. 95.— As in Fig 1., but for PK 016-01#1.
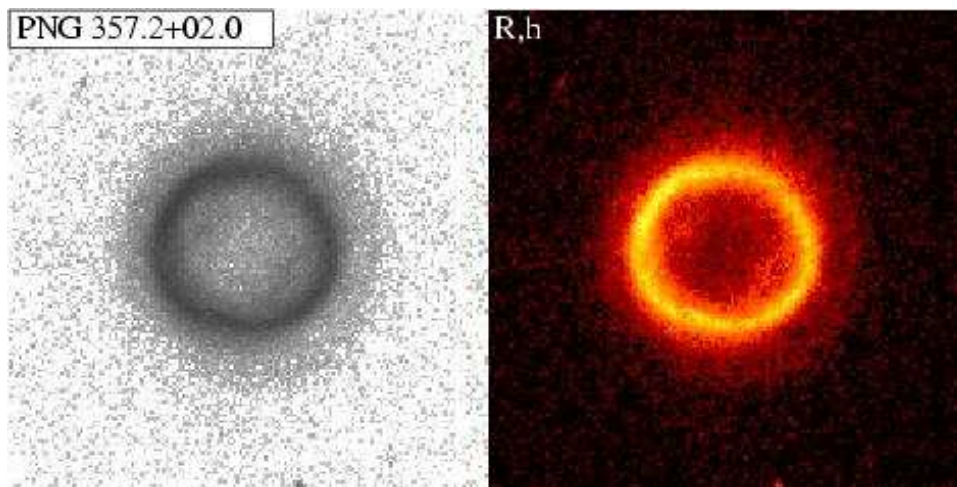
Fig. 96.— As in Fig 1., but for PNG 357.2+02.0.
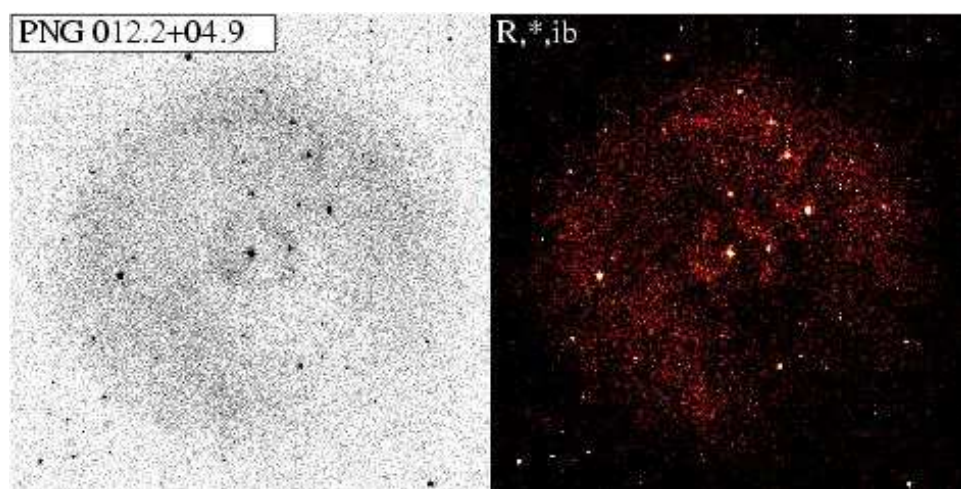
Fig. 97.— As in Fig 1., but for PNG012.2+04.9.
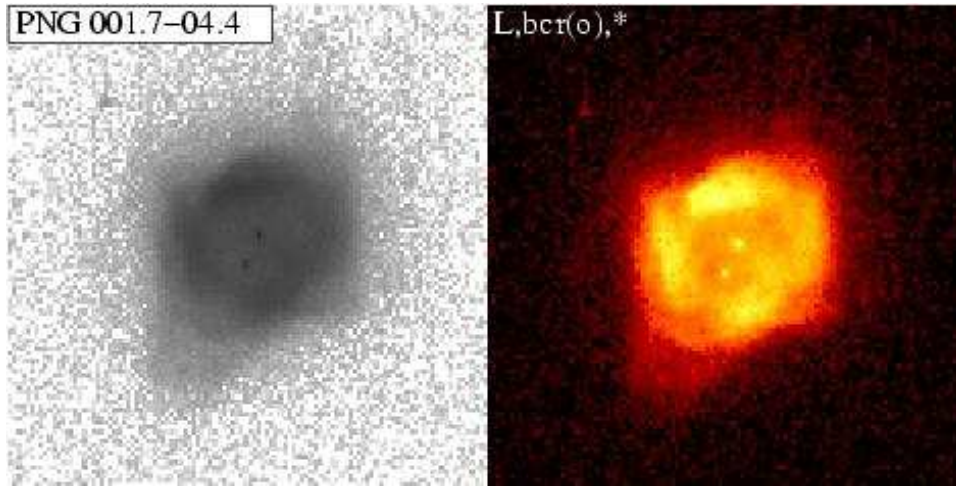
Fig. 98.— As in Fig 1., but for PNG001.7-04.4.
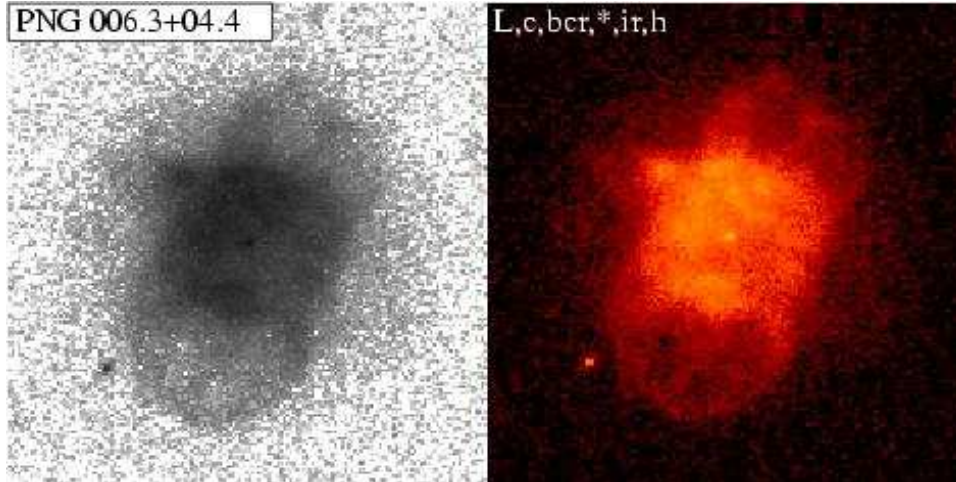
Fig. 99.— As in Fig 1., but for PNG006.3+04.4.
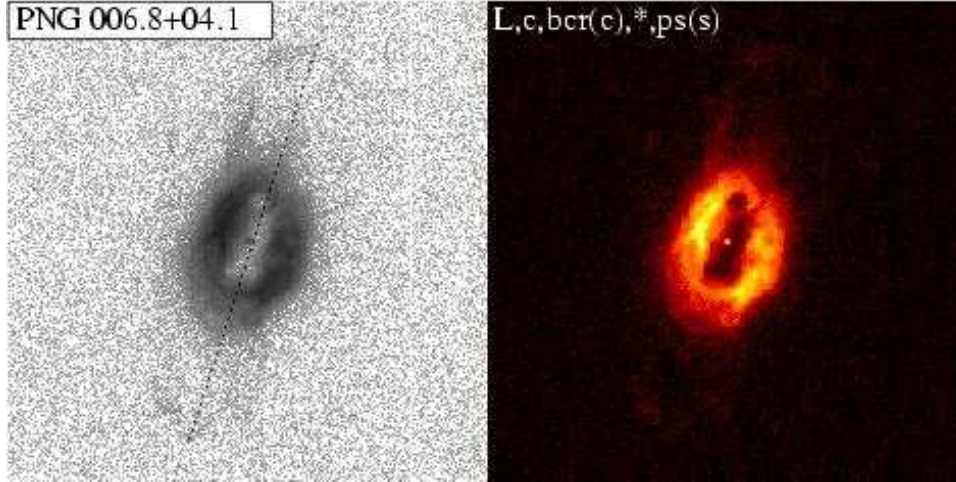
Fig. 100.— As in Fig 1., but for PNG006.8+04.1.
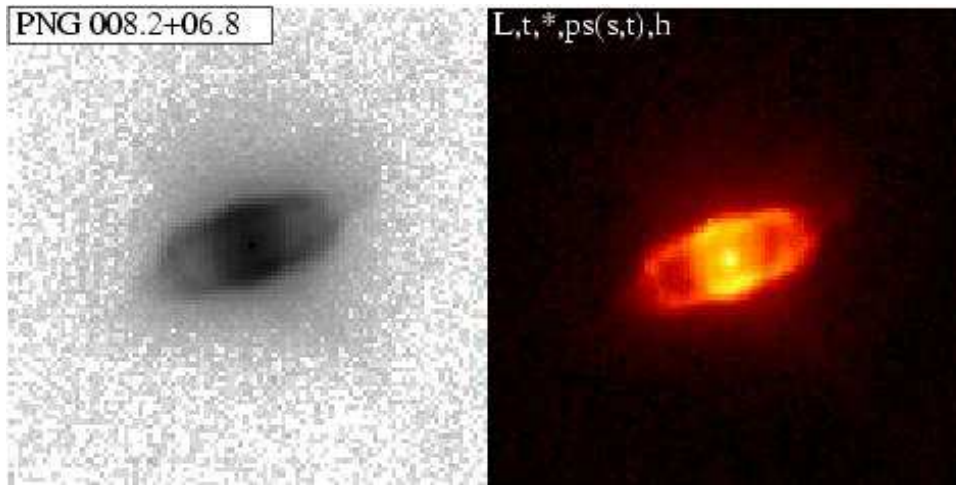
Fig. 101.— As in Fig 1., but for PNG008.2+06.8.
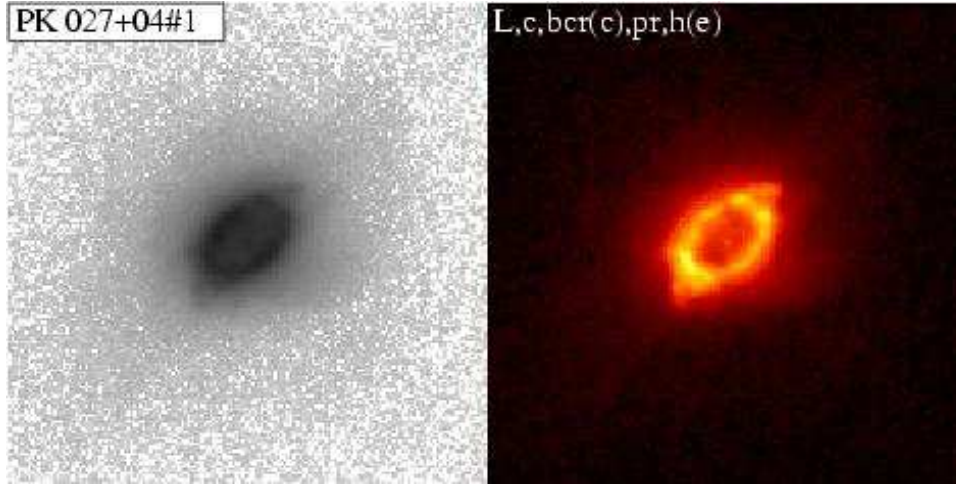
Fig. 102.— As in Fig 1., but for PK 027+04#1.
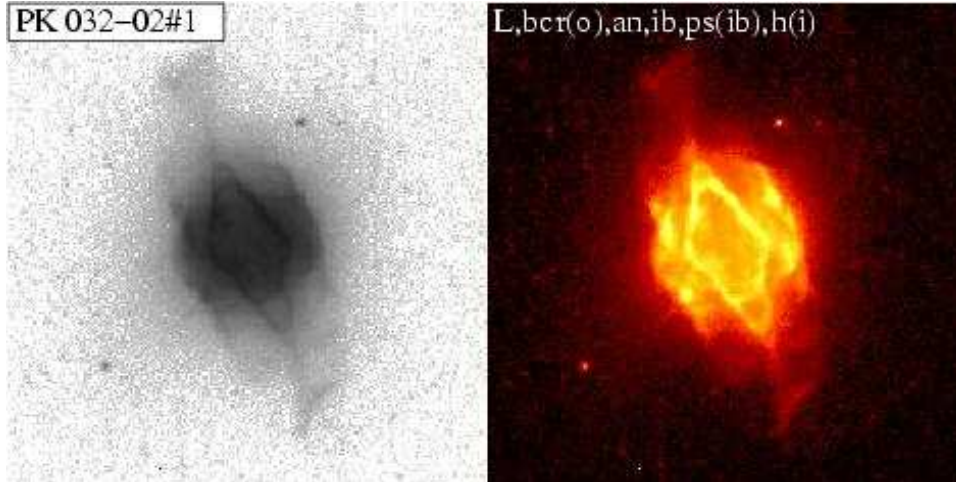
Fig. 103.— As in Fig 1., but for PK 032-02#1.
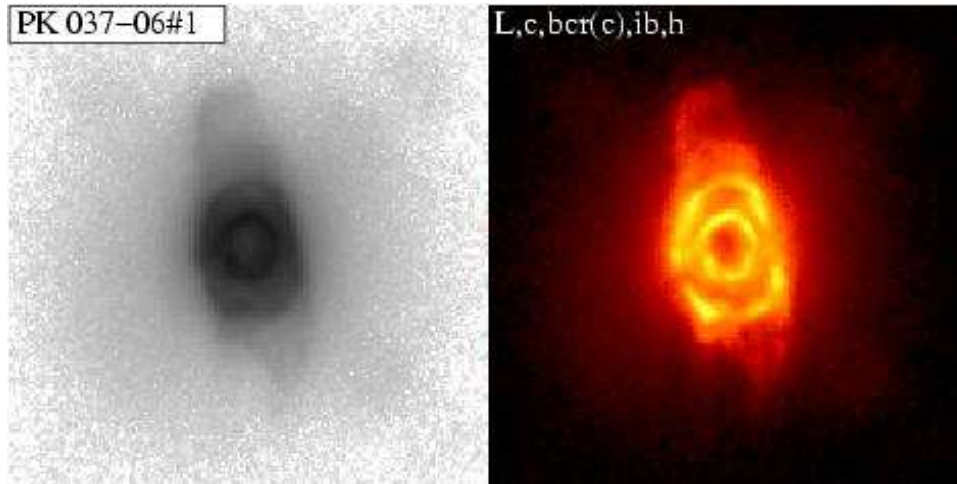
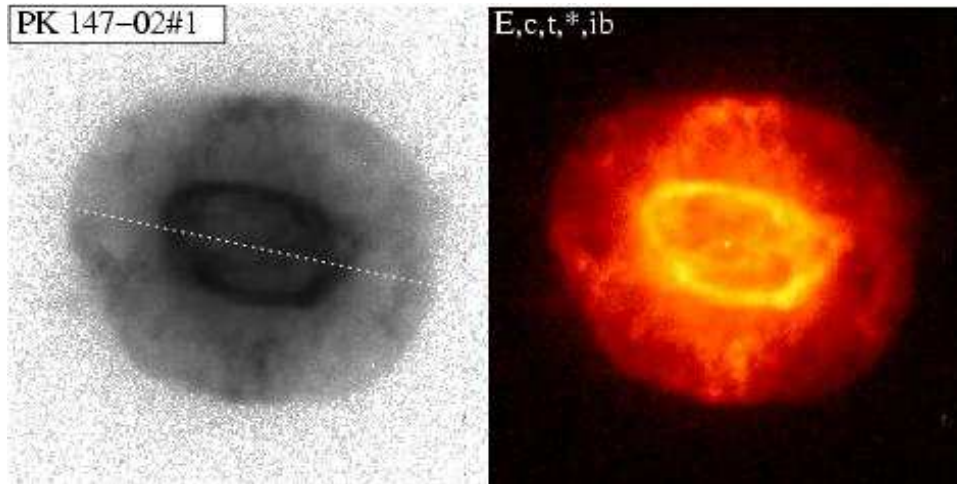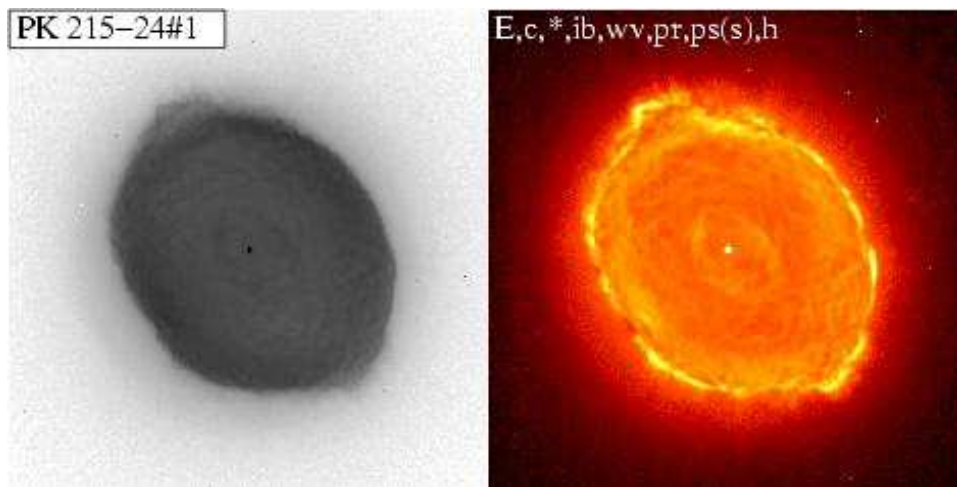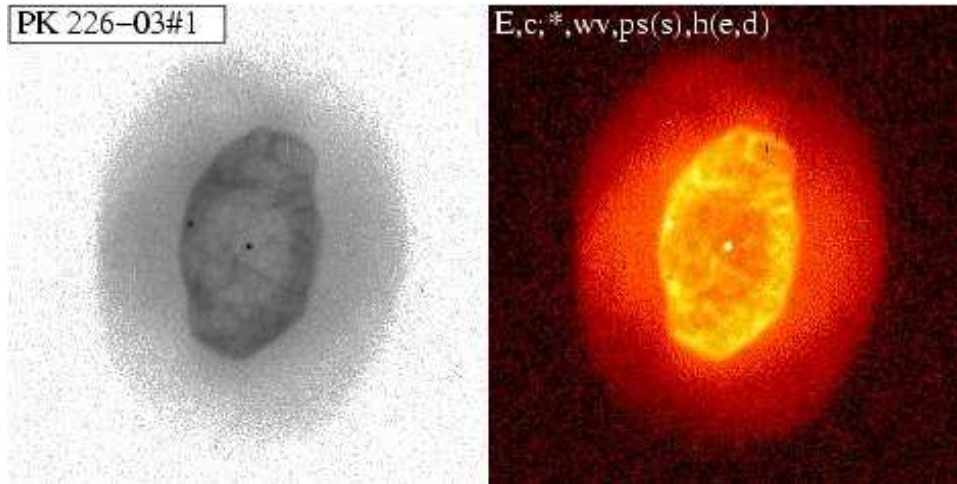Fig. 104.— As in Fig 1., but for PK 037-06#1.

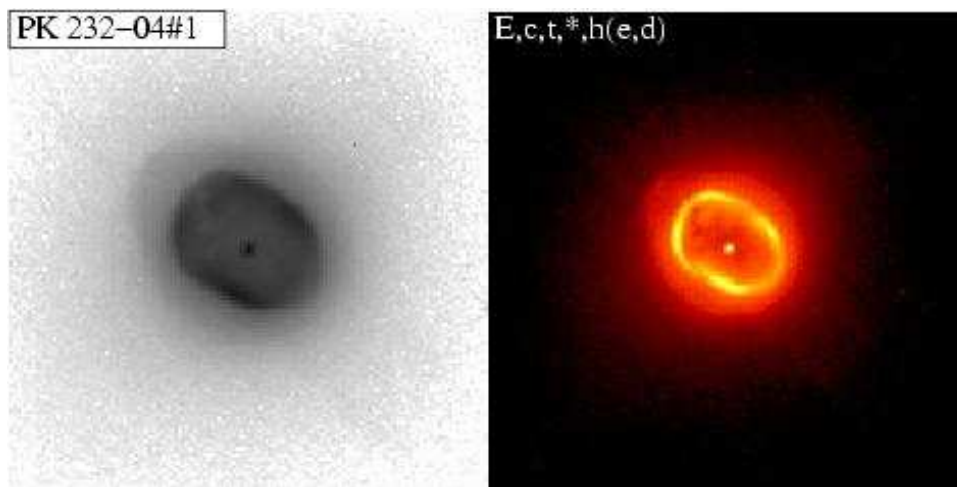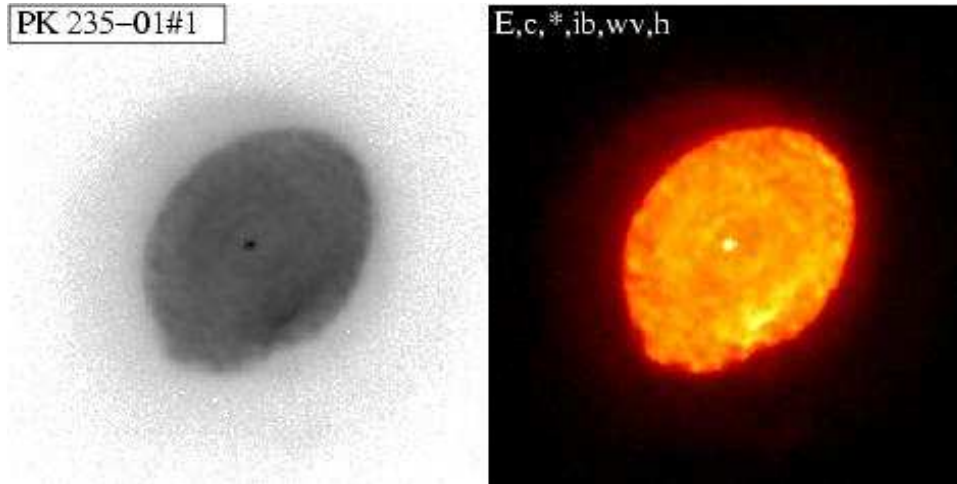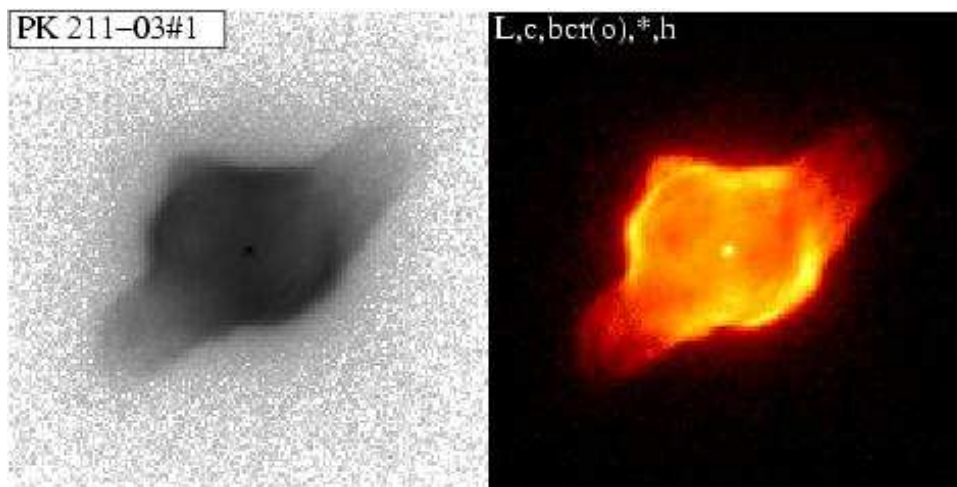Fig. 105.— As in Fig 1., but for PK 211-03#1.
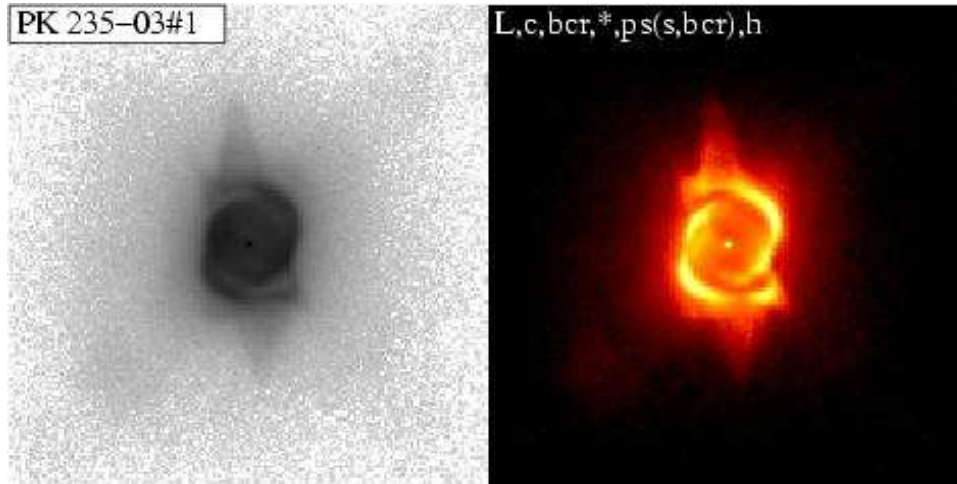
Fig. 106.— As in Fig 1., but for PK 235-03#1.
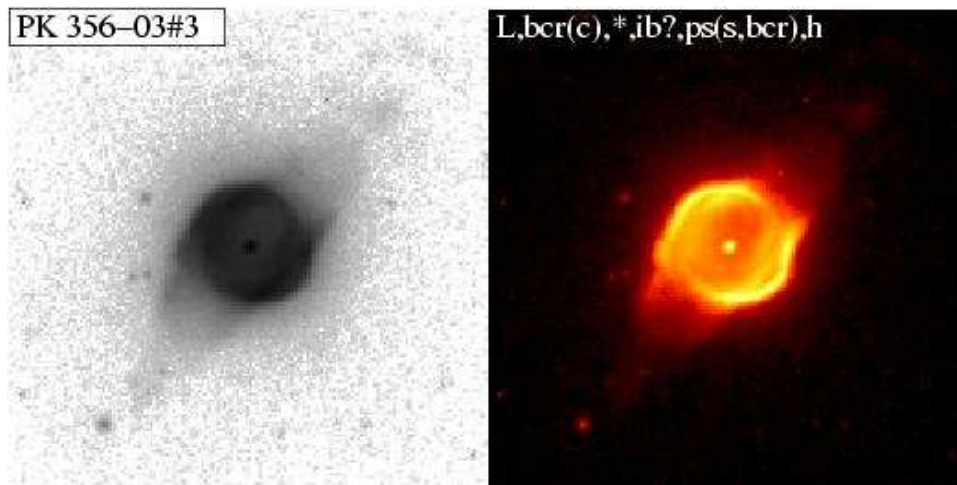
Fig. 107.— As in Fig 1., but for PK 356-03#3.
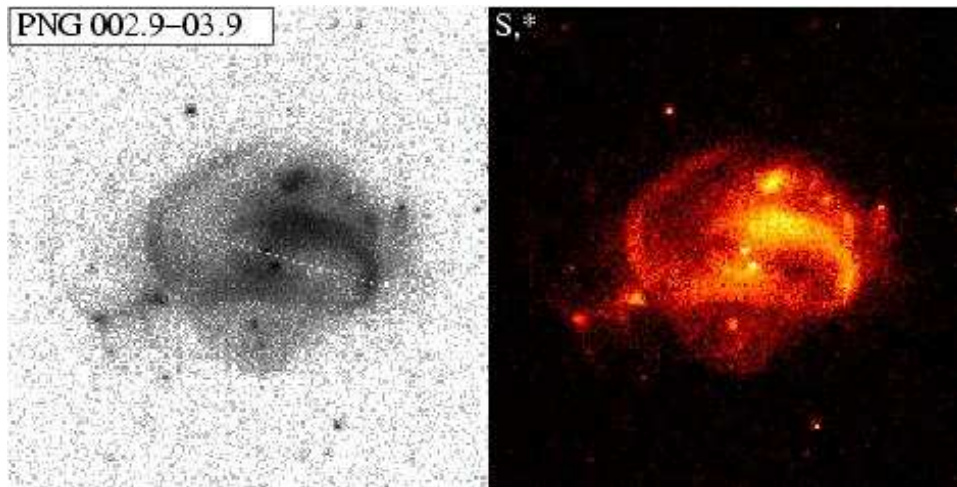
Fig. 108.— As in Fig 1., but for PNG002.9-03.9.
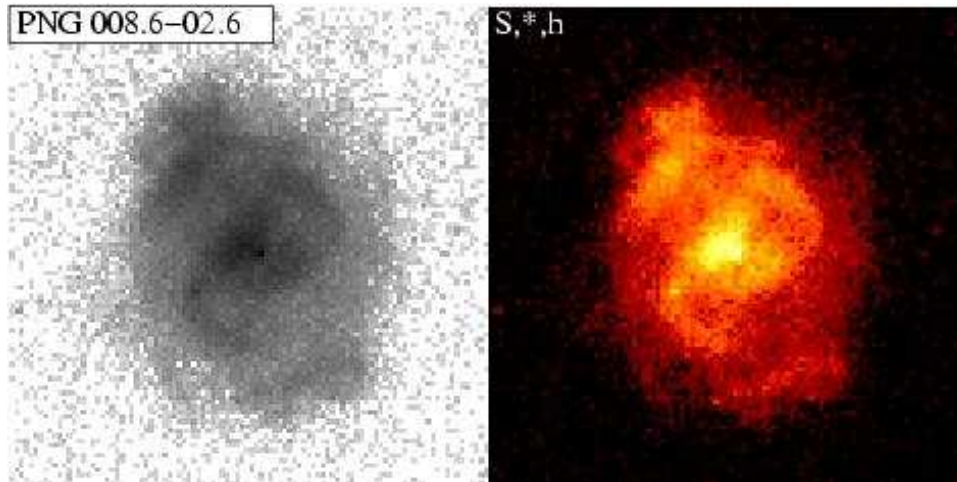
Fig. 109.— As in Fig 1., but for PNG008.6-02.6.
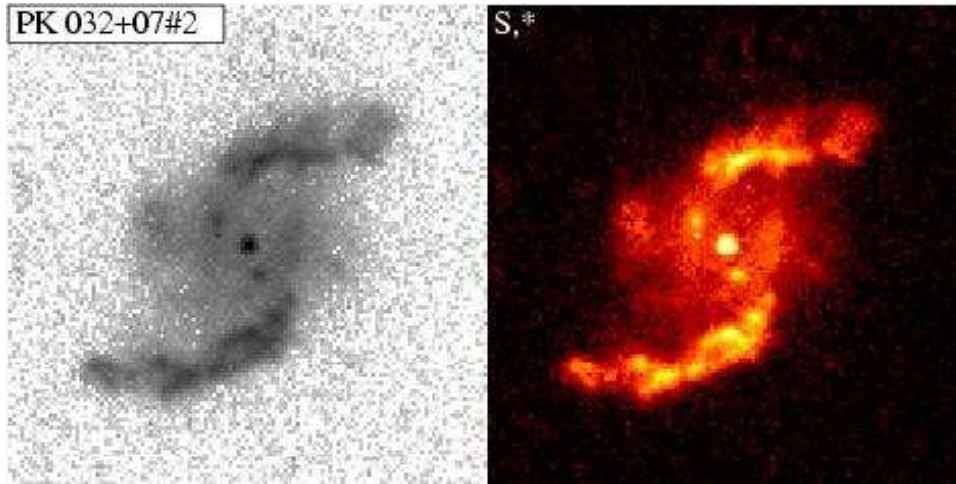
Fig. 110.— As in Fig 1., but for PK 032+07#2 and the F658N ([NII]) filter.
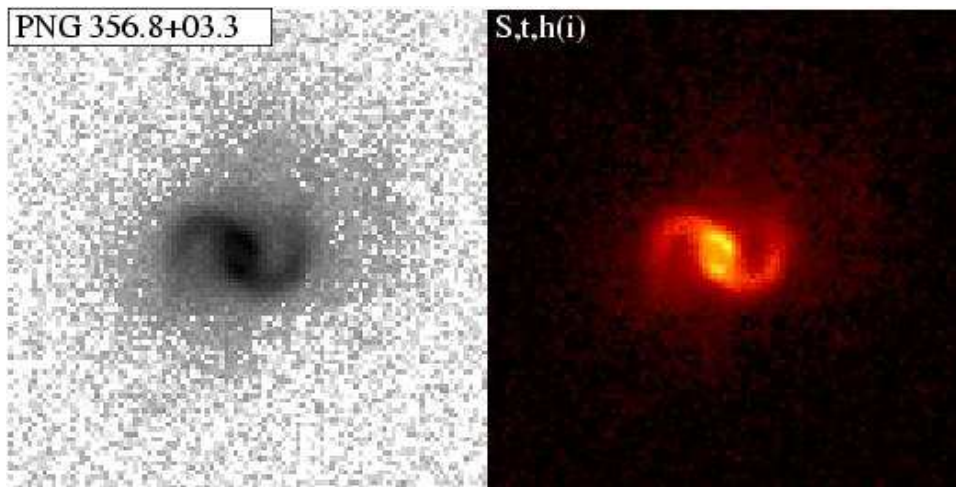
Fig. 111.— As in Fig 1., but for PNG356.8+03.3.
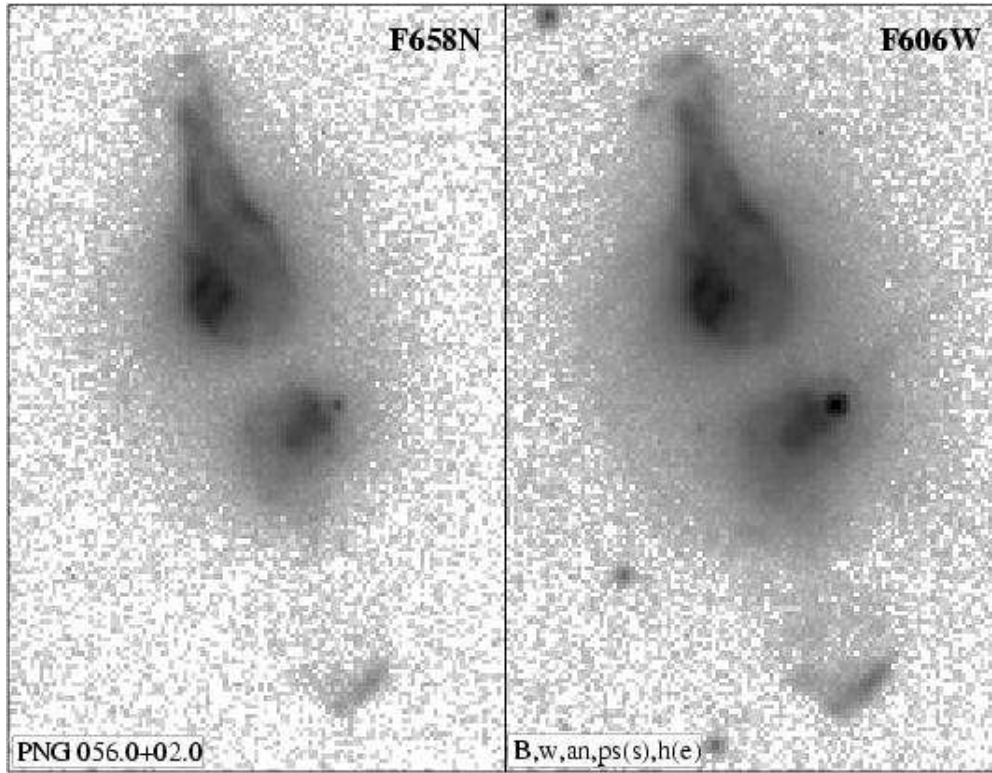
Fig. 112.— HST [NII] (F658N) and broad-band 0.6μm (filter F606W) (*log stretch*) images of the young planetary nebula PN G056.0+02.0, taken with the WFPC2/PC.
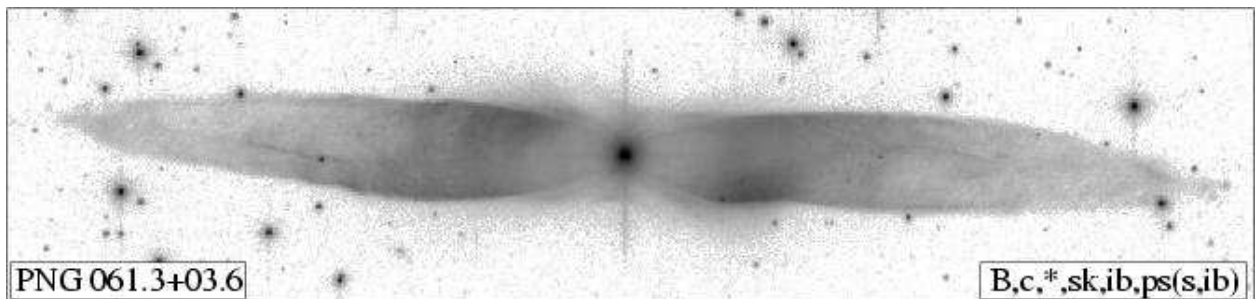
Fig. 113.— HST broad-band 0.6μm (filter F606W) (*log stretch*) image of the young planetary nebula PN G061.3+03.6, taken with the ACS/WFC.
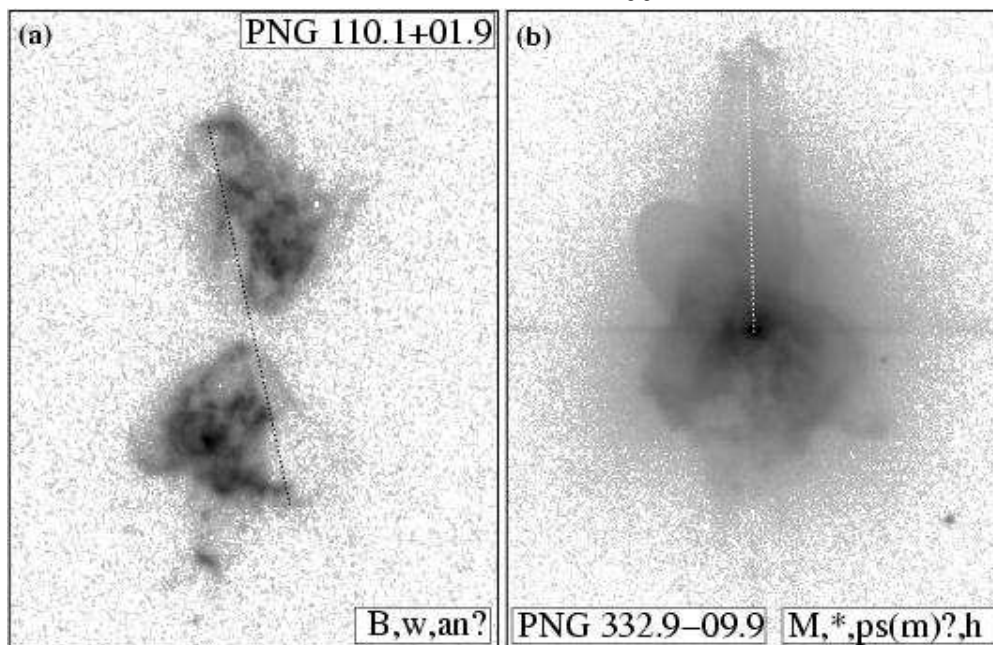
Fig. 114.— HST broad-band (*log stretch*) images, taken with the ACS/HRC, of two young planetary nebulae, (a) 0.6μm (filter F606W) image of PNG110.1+01.9 (also IRAS 22568+6141), and (b) 0.43μm (filter F435W) image of PNG332.9-09.9 (also IRAS 17047-5650).
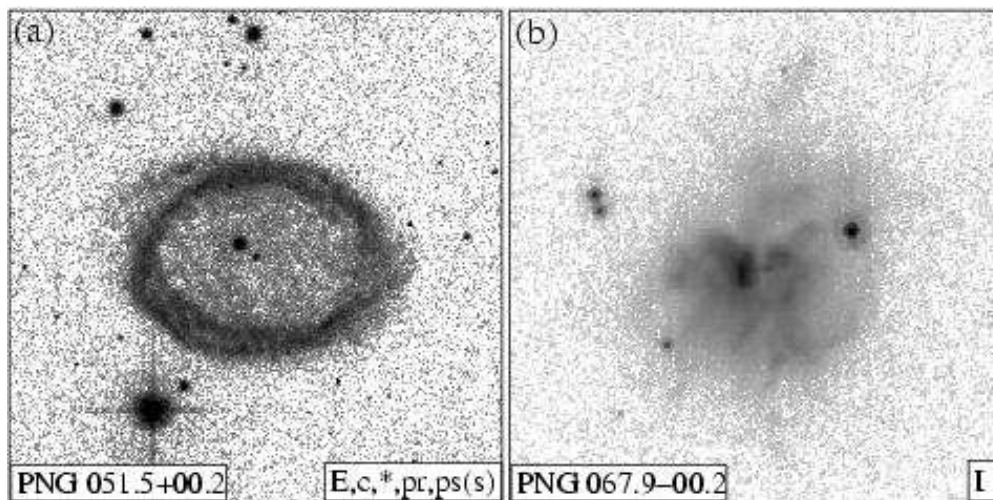
Fig. 115.— HST broad-band 0.6μm (filter F606W) (*log stretch*) images, of two young planetary nebulae, (a) PNG 051.5+00.2 (taken with ACS/WFC), and (b) PN G067.9-00.2 (taken with ACS/HRC).
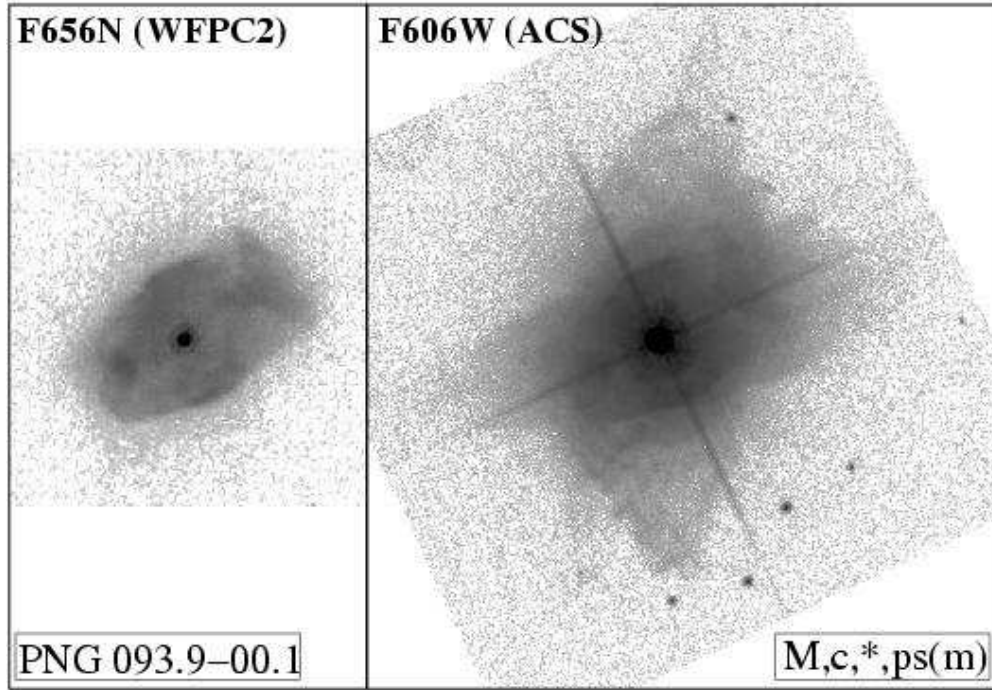
Fig. 116.— HST Hα and broad-band 0.6μm (filter F606W) (*log stretch*) images of the young planetary nebula PNG093.9-00.1 (IRAS 21282+5050). The morphological classification is based on the 0.6μm morphology.
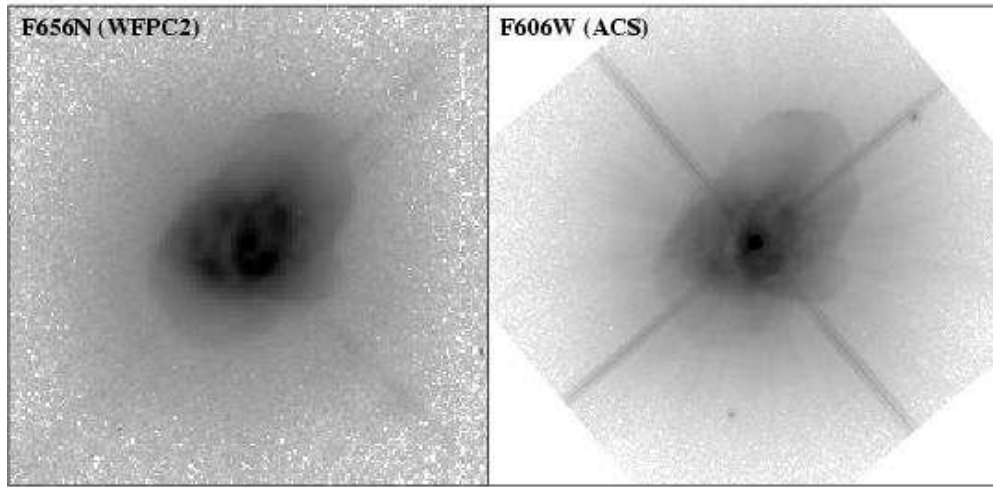
Fig. 117.— HST Hα and broad-band 0.6μm (filter F606W) (*log stretch*) images of the young planetary nebula PK321+03#1 (He 2-113) (adapted from Sahai et al. 2000)
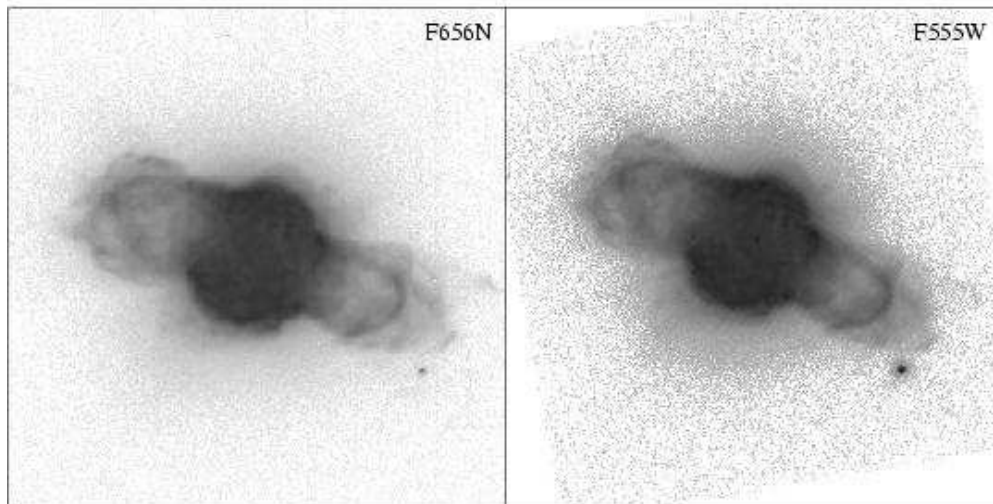
Fig. 118.— HST Hα and broad-band 0.55μm (filter F555W) (*log stretch*) images of the young planetary nebula PK 060-07#2, taken with the WFPC2/PC.
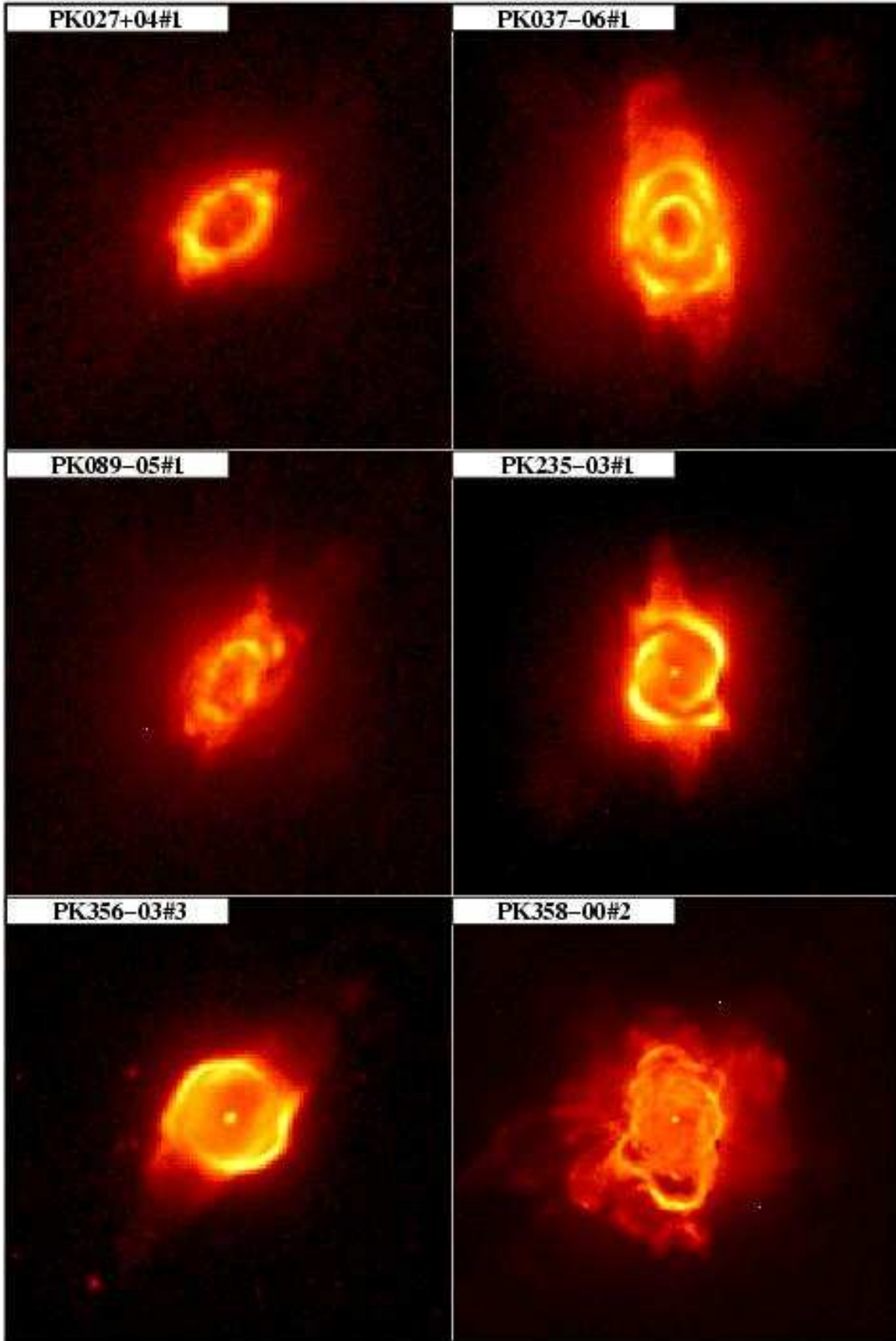
Fig. 119.— Young Planetary Nebulae with "barrel-shaped central regions" which appear to be closed at the barrel ends (bcr(c)).
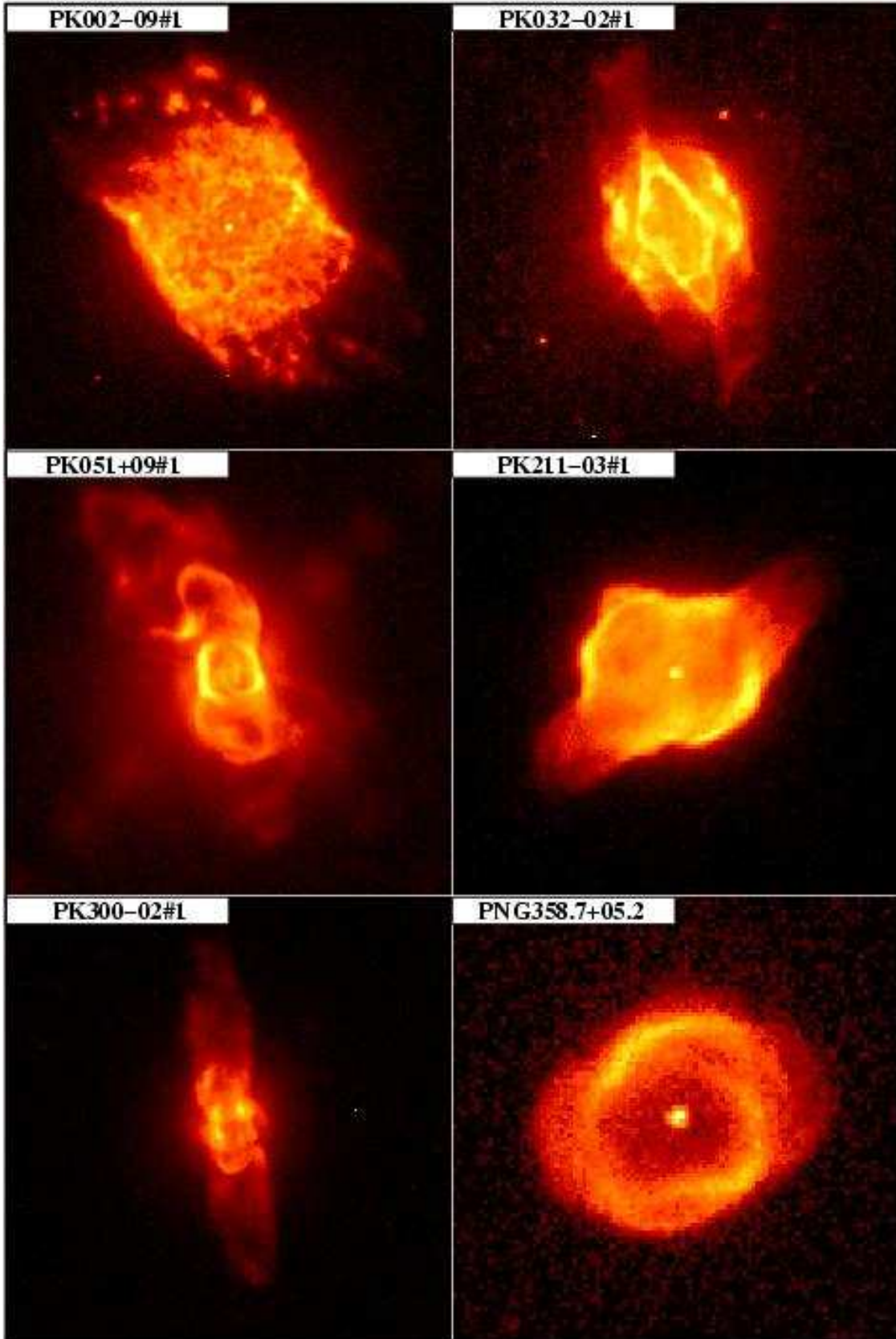
Fig. 120.— Young Planetary Nebulae with "barrel-shaped central regions" which appear to be open at the barrel ends $(bcr(o))$.

PK215−24#1

PK258−00#1

PK352−07#1

PK051−03#1

PK007−04#1

PK082+07#1
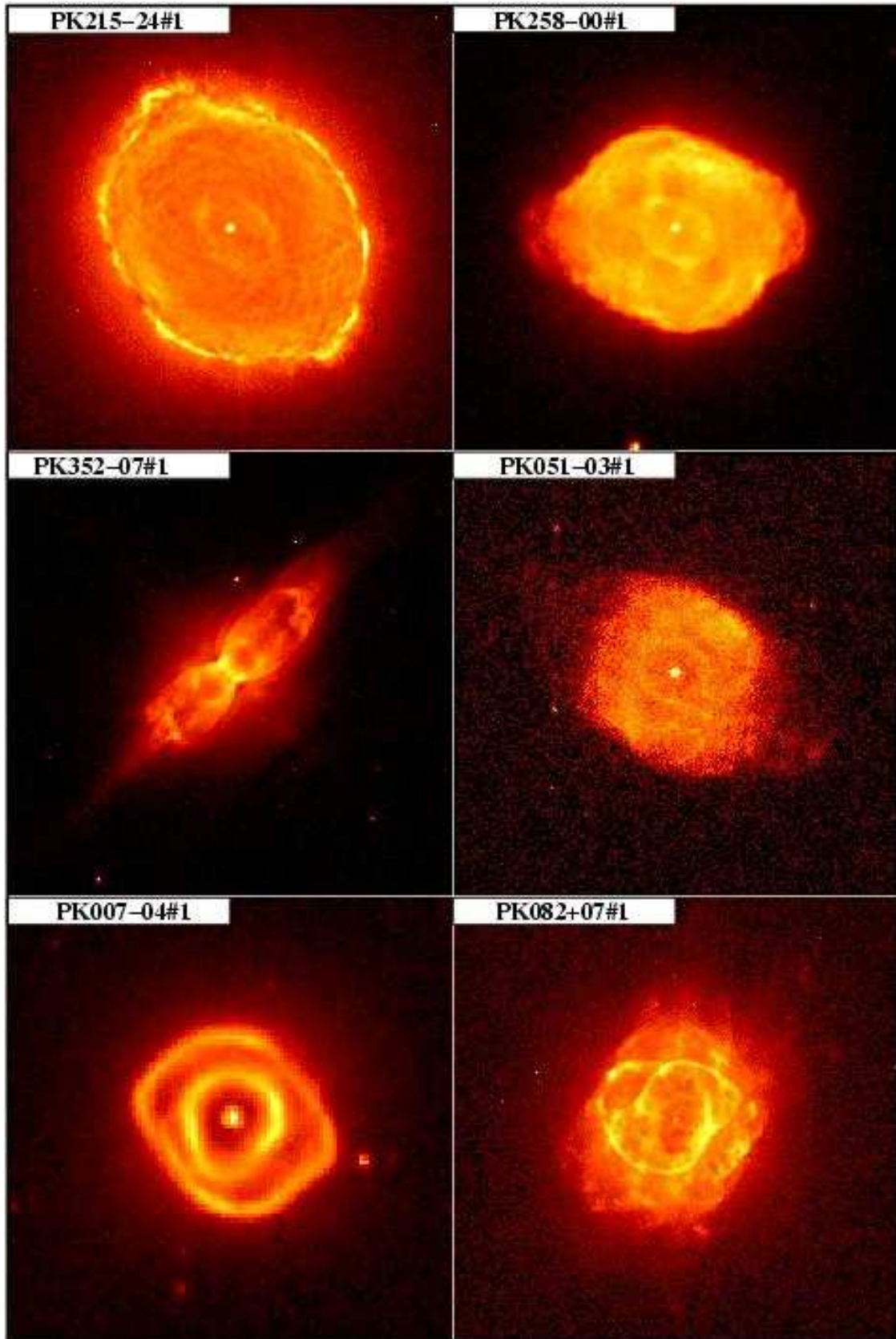
Fig. 121.— Young Planetary Nebulae with inner bubbles
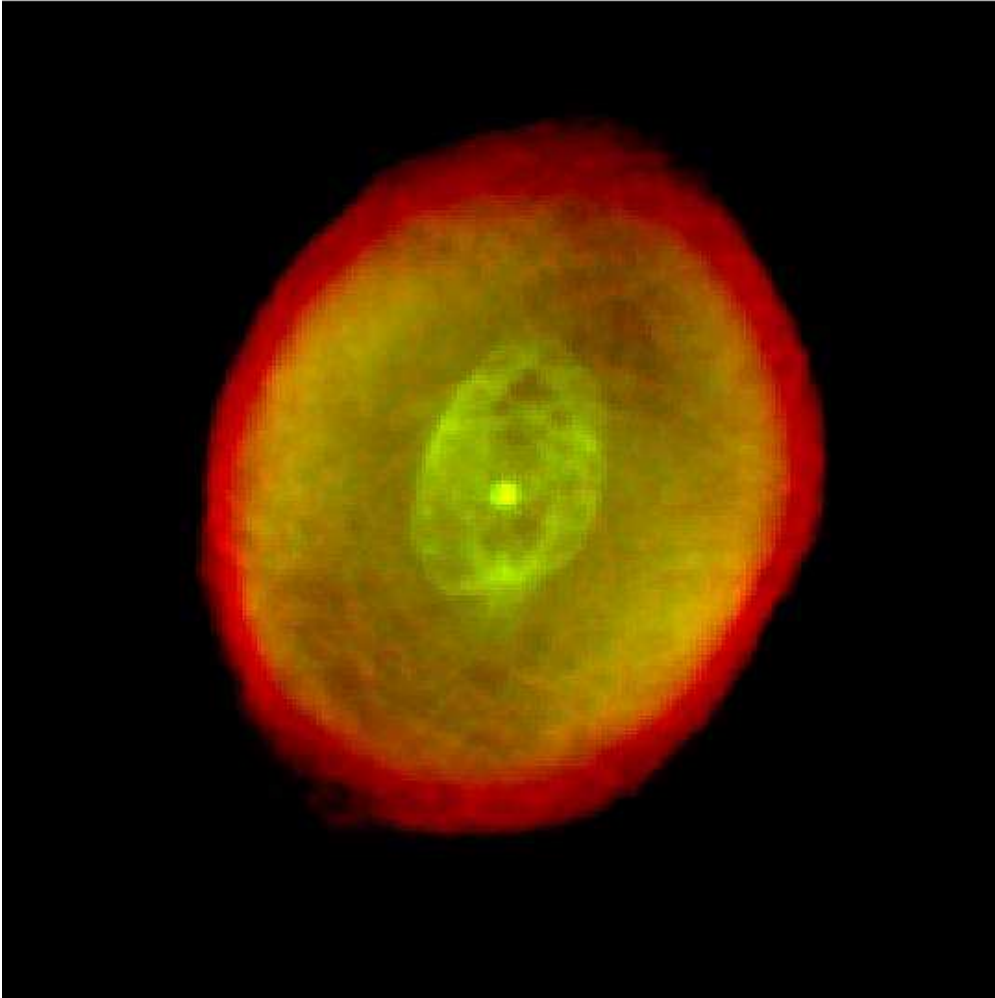
Fig. 122.— A composite image of PK215-24D1 (IC418) (Hα=red, [OIII]λ5007=green), showing the inner bubble
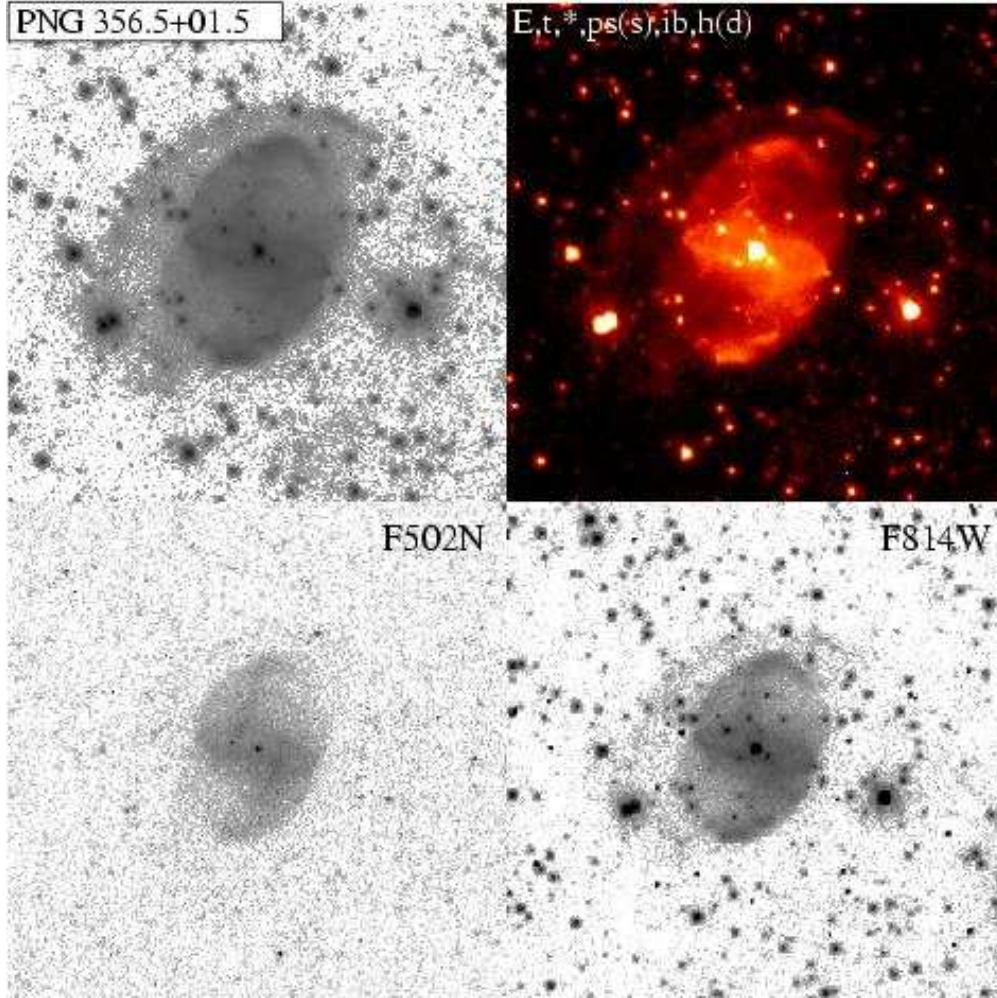
Fig. 123.— *top panel* As in Fig 1., but for PNG356.5+01.5 and the broad-band filter F200LP. *bottom panel* Log-stretch reverse-greyscale images of the same PN in the narrow [OIII]λ5007 (F502N) emission-line filter, and the broad-band 0.8μm F814W filter
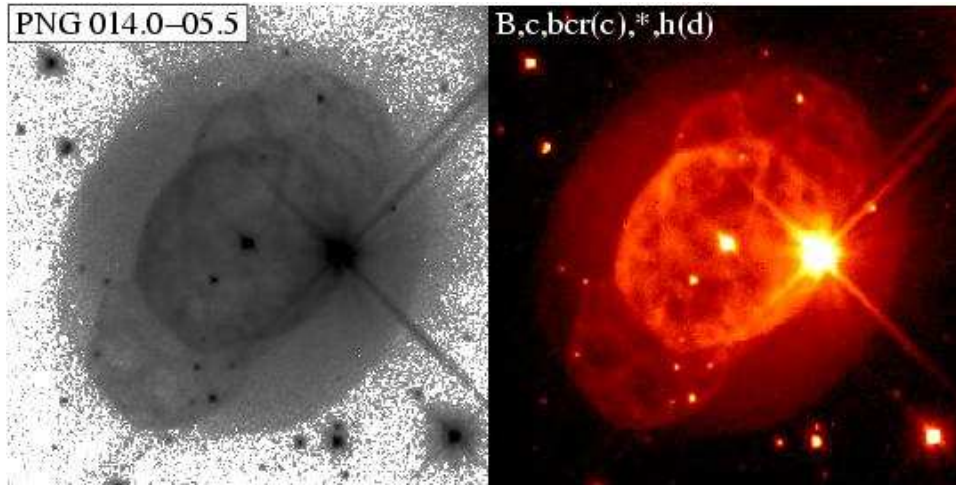
Fig. 124.— As in Fig 1., but for PNG014.0-05.5 and the broad-band filter F200LP
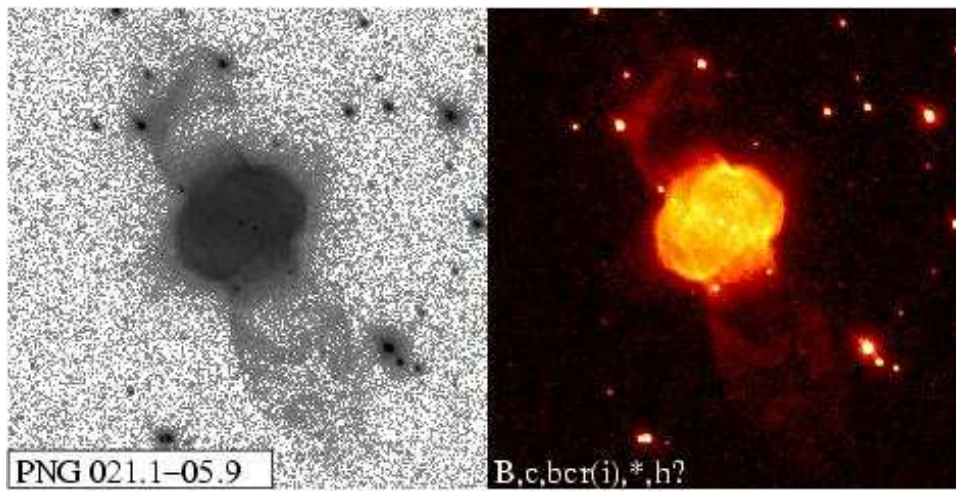
Fig. 125.— As in Fig 1., but for PNG021.1-05.9 and the broad-band filter F200LP
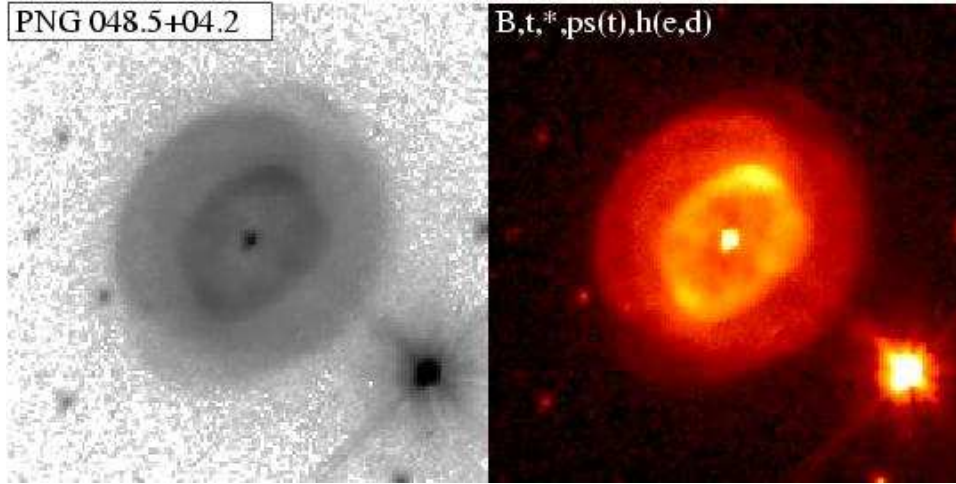
Fig. 126.— As in Fig 1., but for PNG048.5+04.2 and the broad-band filter F200LP
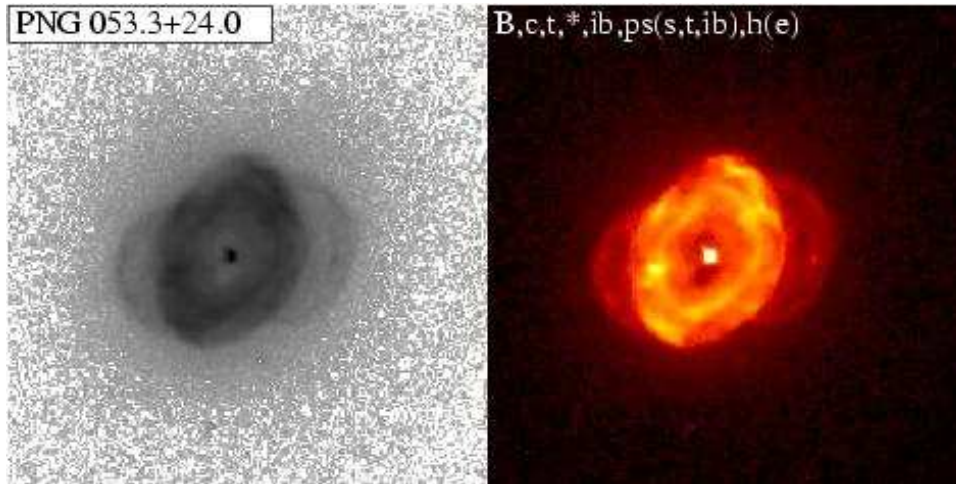
Fig. 127.— As in Fig 1., but for PNG053.3+24.0 and the broad-band filter F200LP
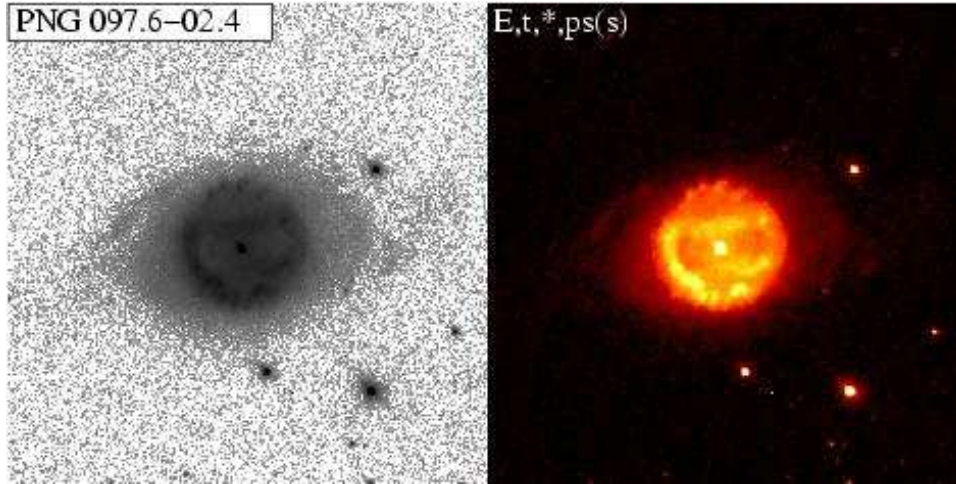
Fig. 128.— As in Fig 1., but for PNG097.6-02.4 and the broad-band filter F200LP
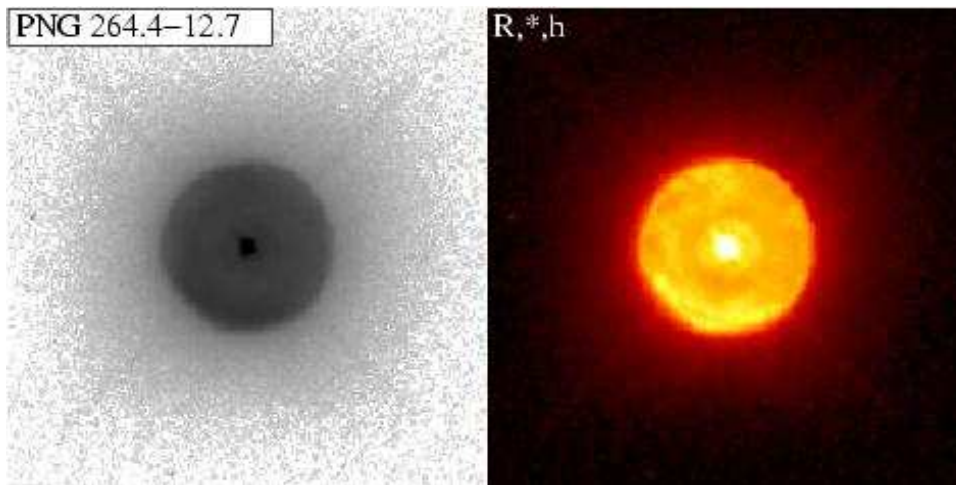
Fig. 129.— As in Fig 1., but for PNG264.4-12.7 and the broad-band filter F200LP
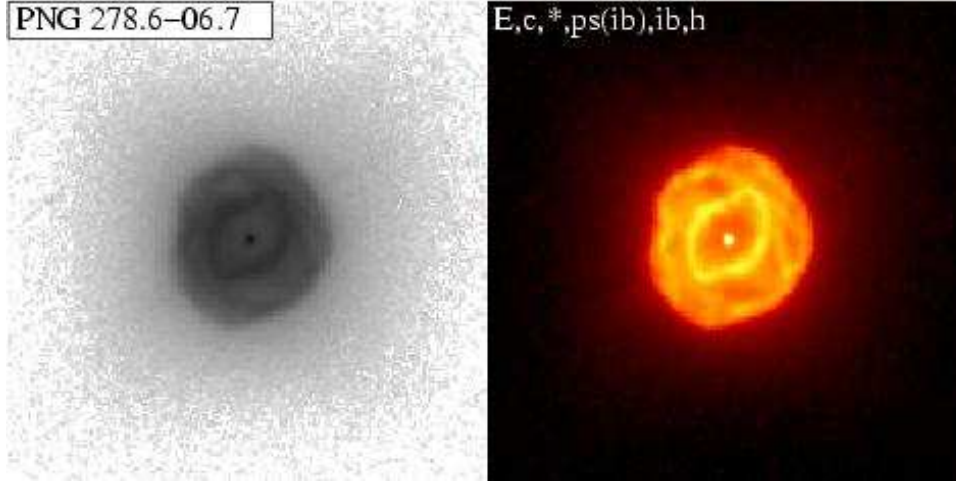
Fig. 130.— As in Fig 1., but for PNG278.6-06.7 and the broad-band filter F200LP
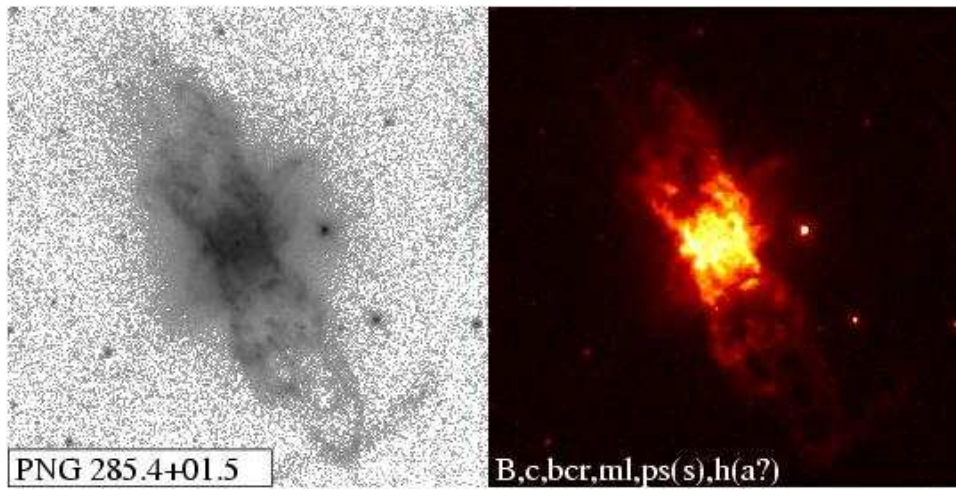
Fig. 131.— As in Fig 1., but for PNG285.4+01.5 and the broad-band filter F200LP
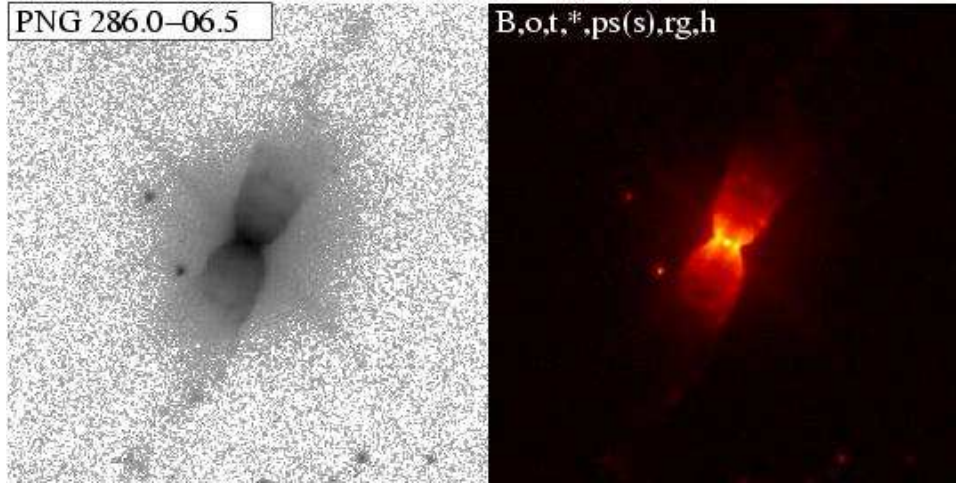
Fig. 132.— As in Fig 1., but for PNG286.0-06.5 and the broad-band filter F200LP
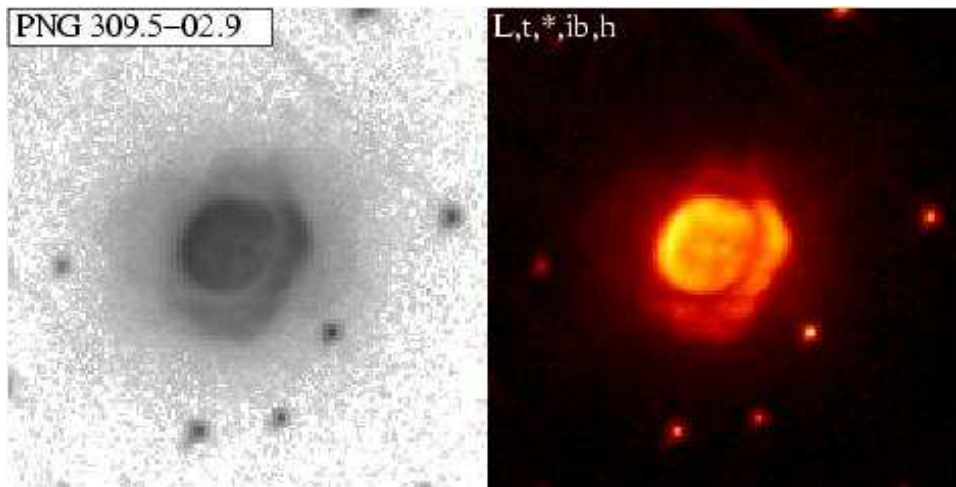
Fig. 133.— As in Fig 1., but for PNG309.5-02.9 and the broad-band filter F200LP
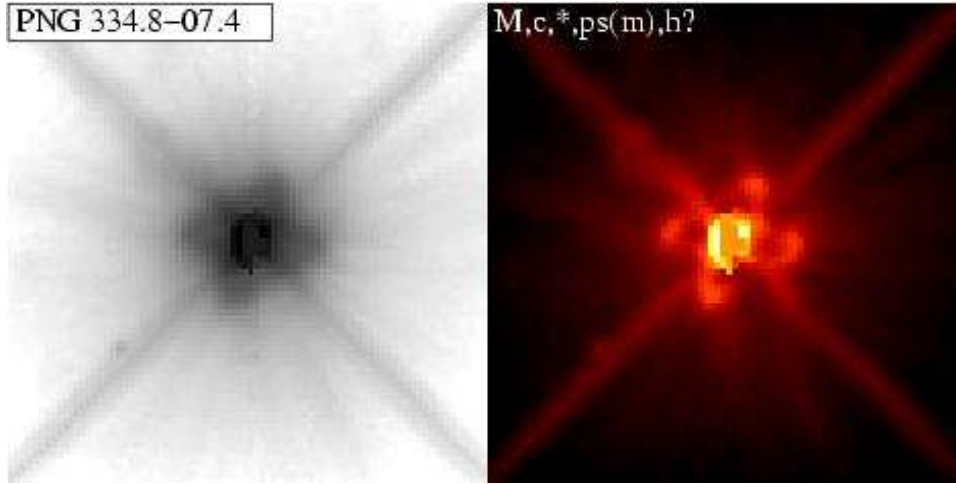
Fig. 134.— As in Fig 1., but for PNG334.8-07.4 and the broad-band filter F200LP
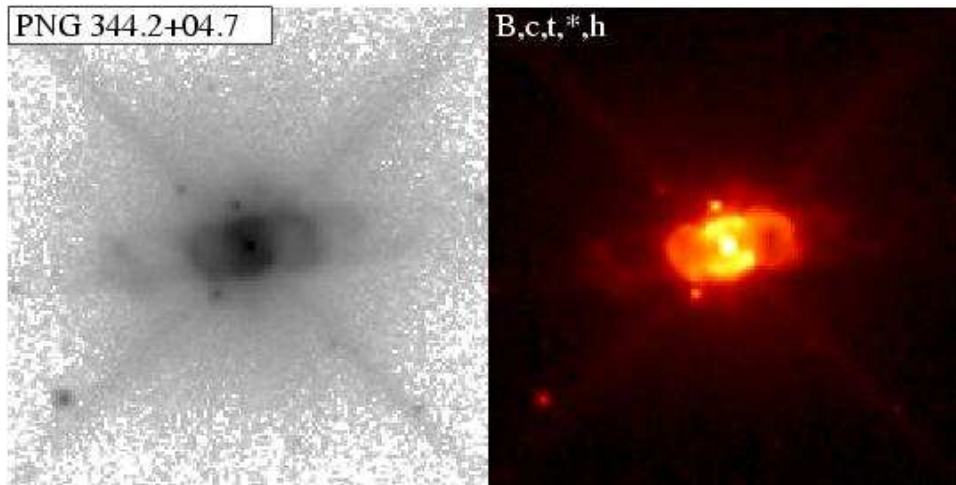
Fig. 135.— As in Fig 1., but for PNG344.2+04.7 and the broad-band filter F200LP
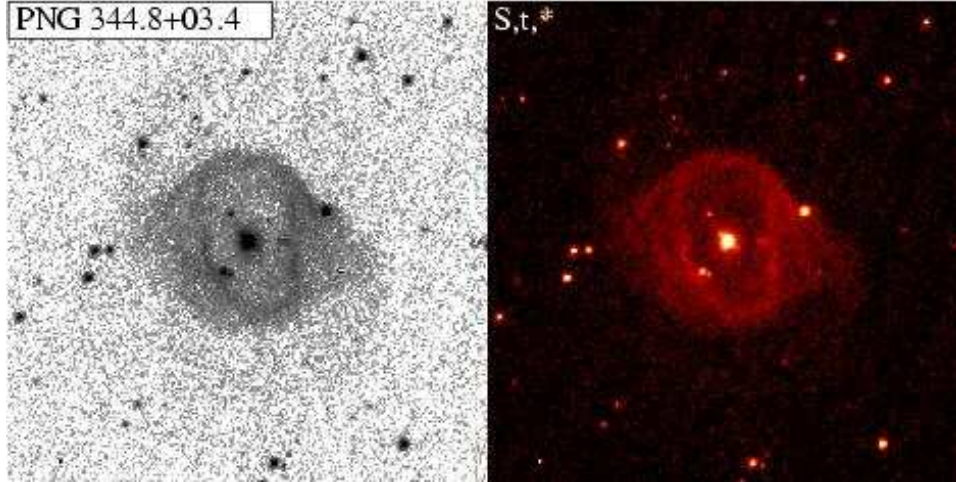
Fig. 136.— As in Fig 1., but for PNG344.8+03.4 and the broad-band filter F200LP
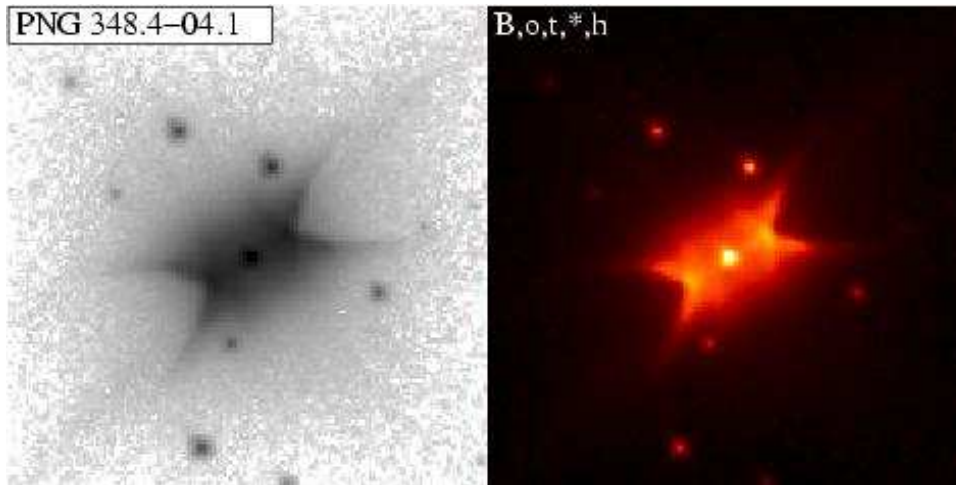
Fig. 137.— As in Fig 1., but for PNG348.4-04.1 and the broad-band filter F200LP
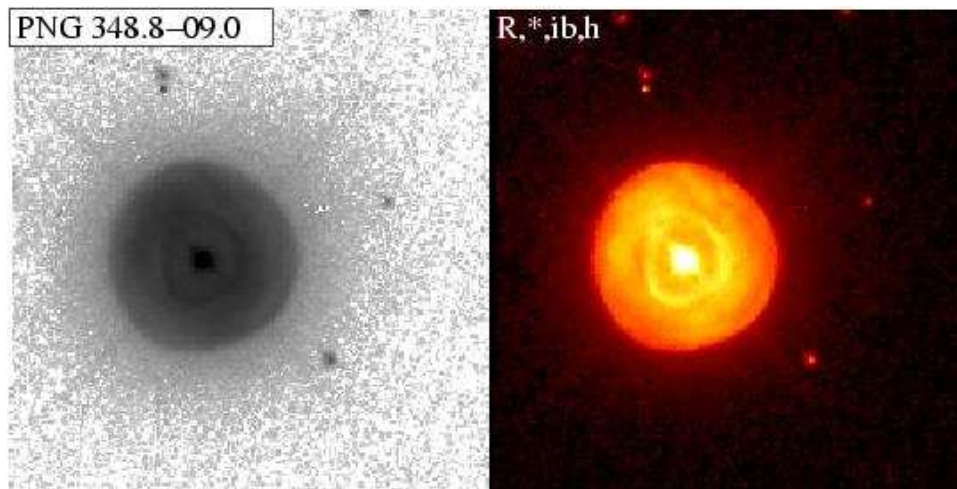
Fig. 138.— As in Fig 1., but for PNG348.8-09.0 and the broad-band filter F200LP

Table 1:: Log of Observations

Name[1]	Filter[2]	Exposure[3]	Date[4]	GO Prog[5]	dataset[6]
Objects	with	R_{exc}	≤ 1		
PK000+17D1	F656N	620	1999-08-12	8345	u5hh3102r
PNG001.2+02.1	F656N	280	2003-06-19	9356	u6mg1001m
PNG001.7-04.4	F656N	200	2002-08-12	9356	u6mg1301m
PNG002.8+01.7	F656N	280	2003-05-02	9356	u6mg0401m
PK002-03D3	F656N	1240	1999-02-12	6353	u35t2105r
PK002-04D1	F656N	1120	1999-08-21	8345	u5hh4103r
PK002-09D1	F656N	480	2000-02-27	8345	u5hh5602r
PNG003.1+03.4	F656N	280	2002-07-02	9356	u6mg1401m
PNG003.6+03.1	F656N	280	2003-04-27	9356	u6mg1501m
PNG003.9-03.1	F656N	280	2003-04-26	9356	u6mg1701m
PNG004.0-03.0	F656N	200	2003-05-20	9356	u6mg5901m
PNG004.8+02.0	F656N	400	2002-08-30	9356	u6mg1901m
PK004+04D1	F656N	620	2001-06-26	8345	u5hh4302r
PNG006.1+08.3	F656N	200	2002-07-06	9356	u6mg2201m
PNG006.8+04.1	F656N	200	2002-07-04	9356	u6mg2401m
PK006+02D5	F656N	620	1999-09-28	8345	u5hh6902r
PK007-04D1	F656N	620	1999-09-27	8345	u5hh0702m
PNG008.2+06.8	F656N	200	2003-03-18	9356	u6mg2601m
PNG008.6-02.6	F656N	280	2002-09-15	9356	u6mg4701m
PK010+00D1 (NGC6537)	F656N	1240	1997-09-12	6502	u42i0402b
PK010+18D2 (M2-9)	F658N	1300	2001-06-28	8773	u66b1405r
PK010-01D1 (NGC6578)	F658N	800	1999-10-23	8390	u5hc0605r
PNG012.2+04.9 (PM1-188)	F656N	1120	2000-02-25	8345	u5hh3003r
PK015+03D1	F656N	1120	1999-07-23	8345	u5hh2803r
PK016-01D1	F656N	620	1999-07-17	8345	u5hh0902r
PK024+03D1	F656N	1120	2000-02-26	8345	u5hh2303r
PK027+04D1	F656N	520	2000-02-20	8307	u59b0604r
PK038+12D1	F656N	1020	1999-02-08	6353	u35t1905r
PK043+03D1	F656N	1120	2000-02-20	8345	u5hh1003r
PK045-02D1	F656N	1920	1996-11-29	6353	u35t3005t
PK051+09D1	F656N	400	1996-10-17	6347	u39h0901t
PNG051.5+00.2 (IRAS19234+1627)	F606W	676	2003-03-12	9463	j8di68010

Continued on Next Page. . .

Table 1 – Continued

Name[1]	Filter[2]	Exposure[3]	Date[4]	GO Prog[5]	dataset[6]
PK051-03D1	F656N	21	1999-07-14	8345	u5hh1101r
PK057-01D1	F656N	520	1999-11-09	8307	u59b0704r
PNG056.0+02.0 (IRAS19255+2123)	F606W	400	2002-02-17	9101	u6fq0805r
PK058-10D1	F656N	1120	1999-11-02	8345	u5hh1403r
PNG061.3+03.6 (IRAS19309+2646)	F606W	600	2006-07-21	10536	j9fj9010
PNG067.9-00.2 (IRAS20011+3024)	F606W	1200	2006-03-29	10536	j9fj97071
PK064+05D1	F656N	1000	1994-06-03	5403	u27q0208t
PK068-02D1	F656N	1120	1999-11-06	8345	u5hh7303r
PK071-02D1	F656N	520	1999-11-04	8307	u59b0504r
PK082+07D1	F656N	1120	1999-08-11	8345	u5hh5203r
PK082+11D1	F656N	1240	1999-02-15	6353	u35t1005r
PNG093.9-00.1 (IRAS21282+5050)[2]	F656N	1080	1999-08-23	8345	u5hh7203r
	F606W	500	2002-12-07	9463	j8di76011
PK100-08D1	F656N	2040	1996-08-05	6353	u35t1105t
PNG110.1+01.9 (IRAS22568+6141)	F606W	800	2002-12-18	9463	j8di58051
PK107-13D1	F656N	1120	1999-08-19	8345	u5hh1603r
PNG332.9-09.9 (IRAS17047-5650)	F435W	450	2002-09-17	9463	j8di80081
PK111-02D1 (HB12-WFPC2)	F656N	400	2001-09-24	9050	u6ci0401m
PK130-11D1	F656N	1120	1999-08-23	8345	u5hh5303r
PK146+07D1	F656N	700	1996-04-18	6353	u35t2401t
PK147-02D1	F656N	1120	1999-10-03	8345	u5hh5403r
PK165-06D1	F656N	1120	1999-08-24	8345	u5hh0103r
PK167-09D1	F656N	700	1996-04-08	6353	u35t2301t
PK211-03D1	F656N	620	1999-08-20	8345	u5hh1802r
PK215-24D1	F656N	888	1999-02-16	6353	u35t0905r
PK226-03D1	F656N	1120	1999-09-27	8345	u5hh1903r
PK232-04D1	F656N	620	1999-08-16	8345	u5hh3902r
PK235-01D1	F656N	1120	1999-09-26	8345	u5hh5503r
PK235-03D1	F656N	620	1999-10-08	8345	u5hh0502r
PK258-00D1	F656N	1120	1999-10-03	8345	u5hh2003r
PK285-02D1	F656N	720	1999-02-14	6353	u35t1407r
PK296-06D1	F656N	1240	1999-02-20	6353	u35t2605r
PK300-02D1	F656N	620	1999-09-24	8345	u5hh5802r
PNG307.5-04.9 (MYCN18)	F656N	600	1995-07-30	6221	u2rc0101t

Table 1 – Continued

Name[1]	Filter[2]	Exposure[3]	Date[4]	GO Prog[5]	dataset[6]
PK315+09D1	F656N	2040	1996-08-11	6353	u35t2805t
PK315-13D1	F656N	322	1996-10-04	6353	u35t0705t
PK320-09D1	F656N	700	1996-04-04	6353	u35t1501t
PK321+02D1	F656N	2040	1996-09-23	6353	u35t2905t
PK321+03D1	F656N	1120	1999-09-20	8345	u5hh7103r
PK325-12D1	F656N	1240	1999-02-20	6353	u35t0605r
PK326-06D1	F656N	1240	1999-02-13	6353	u35t2705r
PK327-02D1	F656N	2040	1996-08-12	6353	u35t2205t
PK331-01D1 (MZ-3)	F656N	900	1998-06-30	6856	u47b0101b
PK331-02D2	F656N	1120	1999-06-06	8345	u5hh3303r
PK350+04D1	F656N	620	1999-08-29	8345	u5hh2502r
PNG351.1+04.8	F656N	160	2003-06-05	9356	u6mg2901m
PNG351.9-01.9	F656N	200	2003-05-26	9356	u6mg4801m
PNG352.6+03.0	F656N	200	2002-08-11	9356	u6mg3001m
PK352-07D1	F656N	480	1999-08-23	8345	u5hh1302r
PNG354.5+03.3	F656N	280	2003-05-04	9356	u6mg5001m
PNG354.9+03.5	F656N	280	2002-10-15	9356	u6mg4901m
PNG355.4-02.4	F656N	200	2002-08-11	9356	u6mg3101m
PNG355.9+03.6	F656N	280	2003-06-20	9356	u6mg3301m
PK355-03D3	F656N	1120	2001-06-26	8345	u5hh6503r
PK355-04D2	F656N	620	2000-02-23	8345	u5hh3702r
PNG356.5-03.6	F656N	360	2002-09-18	9356	u6mg4101m
PNG356.8+03.3	F656N	280	2002-07-16	9356	u6mg3501m
PK356-03D3	F656N	1120	2001-06-26	8345	u5hh7503r
PNG357.1-04.7	F656N	200	2003-06-19	9356	u6mg3601m
PNG357.2+02.0	F656N	280	2002-08-14	9356	u6mg4201m
PNG358.5-04.2	F656N	160	2003-06-19	9356	u6mg3801m
PNG358.7+05.2	F656N	280	2002-09-18	9356	u6mg3901m
PNG358.9+03.4	F656N	200	2003-06-19	9356	u6mg5301m
PK358-00D2	F656N	1720	1996-10-04	6353	u35t1807t
PNG359.2+04.7	F656N	280	2003-03-30	9356	u6mg5201m
Objects	with	R_{exc}	> 1		
PNG002.3-03.4	F656N	280	2003-04-26	9356	u6mg0501m
PNG002.9-03.9	F656N	280	2003-04-27	9356	u6mg0601m

Table 1 – Continued

Name[1]	Filter[2]	Exposure[3]	Date[4]	GO Prog[5]	dataset[6]
PNG003.8+05.3	F656N	280	2002-09-12	9356	u6mg1601m
PK003+02D1	F656N	600	1996-08-17	6347	u39h0401t
PNG004.1-03.8	F656N	280	2002-09-11	9356	u6mg1801n
PNG004.8-22.7 (HE2-436)	F656N	200	2003-05-03	9356	u6mg0201m
PNG005.2-18.6 (STWR2-21)	F656N	280	2003-03-16	9356	u6mg0301m
PNG006.8-19.8 (WRAY16-423)	F656N	200	2002-07-25	9356	u6mg0101m
PNG006.3+04.4	F656N	280	2003-04-02	9356	u6mg6001m
PK008-07D2	F656N	1120	2000-02-26	8345	u5hh4503r
PK010-06D1	F656N	1120	1999-08-26	8345	u5hh4603r
PK013+04D1	F656N	620	2001-06-25	8345	u5hh4702r
PK019-05D1	F656N	240	1999-11-08	8307	u59b0301r
PK023-02D1	F656N	620	1999-09-24	8345	u5hh4802r
PK027-09D1	F656N	1120	2001-06-25	8345	u5hh4903r
PK032+07D2	F658N	600	1999-06-29	6347	u39h2901r
PK032-02D1	F656N	600	1998-11-21	6347	u39h3201r
PK037-06D1	F656N	160	1999-10-31	8307	u59b0101r
PK060-07D2	F656N	1120	1999-07-13	8345	u5hh5003r
PK074+02D1	F656N	280	1999-11-01	8307	u59b0401r
PK089-05D1	F656N	240	1999-11-02	8307	u59b0201r
PK304-04D1	F656N	1120	2000-01-29	8345	u5hh5903r
PNG356.9+04.4	F656N	280	2003-04-18	9356	u6mg5601m

1 2 3 4 5 6 7

---

[1]Col. 1: Object name as defined in GO program; if this name was not in standard PK or PNG format, then it is provided in parenthesis, and the PK or PNG name is given

[2]Col. 2: The filter used for the images utilised for morphological classification. This is generally the narrow-band F656N filter (which covers the Hα line), but occasionally the F658N filter (which covers the [NII] line) has been used. For a few objects, only broad-band filter images (F435W or F606W) were available.

[3]Col. 3: The total exposure time of the image.

[4]Col. 4: The observation date (yyyy-mm-dd).

[5]Col. 5: The GO program ID number.

[6]Col. 6: the name for the image dataset as listed in the HST archive - when several exposures have been averaged, then it is the name of the last dataset.

[7]For this object, although both the F656N and F606W (broad-band) images are presented, only the latter has been used for the morphological classification (explanation in text).

Table 2:: Morphological Classification Codes

PRIMARY CLASSIFICATION: Nebular Shape

B	Bipolar
M	Multipolar
E	Elongated
I	Irregular
R	*Round*
L	*Collimated Lobe Pair*
S	*Spiral Arm*

SECONDARY CHARACTERISTICS

Lobes

o	lobes open at ends
c	lobes closed at ends

Central Region

w	central region is (relatively) dark, and shows an obscuring waist
t	*central region is bright and has a toroidal structure*
bcr	*central region is bright and barrel-shaped*
bcr(c)	*barrel has closed ends*
bcr(o)	*barrel has open ends*
bcr(i)	*irregular structure present in barrel interior*

Central Star

⋆	central star evident in optical images
⋆(nnn)	star is offset is offset from the center of symmetry of one or more nebular structures, *nnn* is maximum offset in milliarcsec

Table 2 – Continued

Other Nebular Characteristics

an   ansae

ml   minor lobes

sk   a skirt-like structure around the primary lobes

ib   an inner bubble inside the primary nebular structure

wv   a patterned structure, such as a weave or a mottling

rg   rings projected on lobes

rr   radial rays

pr   one or more pairs of diametrically opposed protrusions on the primary geometrical shape

ir   additional unclassified nebular structure lacking symmetry, not covered by

*   the primary or secondary classifications*

Point Symmetry

ps(m)   due to presence of two or more pairs of diametrically-opposed lobes

ps(an)   due to diametrically-opposed ansae

ps(s)   overall geometric shape of lobes is point-symmetric

ps(t)   waist has point-symmetric structure

ps(bcr)   barrel-shaped central region has point-symmetric structure

ps(ib)   inner bubble has point-symmetric structure

Halo

h   halo (relatively low-surface brightness diffuse region around primary nebular structure) is present

h(e)   halo has elongated shape

h(i)   halo has indeterminate shape

h(a)   halo has centro-symmetric arc-like features

h(sb)   halo shows searchlight-beams

h(d)   halo has a sharp outer edge, or shows a discontinuity in its interior

Table 3:: Properties of Young Planetary Nebulae

Name	Name			Morphology		R_{exc}	Size	V_1	V_2	D	Age	XBox	Fig #
(1)	(2)			(3)		(4)	(5)	(6)	(7)	(8)	(9)	(10)	(11)
PK	PNG	P	Cen	PS	Other		$''$	km s^{-1}		kpc	yr	$''$	
Objects	with	$R_{exc} \leq 1$											
000+17#1	000.1+17.2	B,c	t,*	...	h	0.31	6.02	22	...	6.16	3991	8.203	1
001+02#1	001.2+02.1	E	t,*	...	...	0.41	2.32	22	...	5.42	1356	6.836	52
001-04#1	001.7-04.4[12]	L	bcr(o),*	...	...	0.02	3.29	22	...	7.1	2514	5.013	98
002+01#1	002.8+01.7	E,c	t,*	ps(s)	...	0.01	3.89	22	...	4.28	1796	5.468	53
002-03#3	002.6-03.4	M,c	t,*	ps(m)	h(a)	0	4.33	22	...	4.2	1959	8.203	31
002-04#1	002.1-04.2	M	bcr(o)	ps(m)	h(a)	0.82	3.59	22	...	4.9	1895	5.468	32
002-09#1	002.2-09.4	B,o	bcr(o,i),*	ps(s)	h	< 1	10.74	...	18	4.93	6969	13.671	3
003+03#1	003.1+03.4	E,c	*	...	...	0	3.9	22	...	5.88	2471	6.836	54
003+03#2	003.6+03.1[13]	B,c	t	ps(s)	ml,h	0.19	5.4	22	...	8	4657	6.836	4
...	003.9-03.1	I	...	...	...	0.98	7.1	22	...	8	6118	9.57	88
004-03#1	004.0-03.0[14]	E	t,*	...	h(d)	0.98	4.83	22	...	4.04	2103	8.203	55
004+02#1	004.8+02.0	R	*	...	pr	0.04	3.55	22	...	5.23	2000	5.468	94
004+04#1	004.9+04.9[15]	E,c	*	...	h(e,d)	0.61	3.67	22	...	4.18	1651	11.38	58
006+08#1	006.1+08.3	E,c	...	...	ib,h	0.52	2.56	22	...	2.88	795	5.468	60
006+04#2	006.8+04.1	L,c	bcr(c),*	ps(s)	...	0.76	12.12	22	...	3.19	4157	13.671	100
006+02#5	006.4+02.0	M,c	t,*	ps(m)	h	0.71	4.09	22	...	4.22	1859	6.836	34
007-04#1	007.8-04.4	E,c	*	ps(s)	ib,h	0	2.04	22	...	6.46	1416	4.557	62
008+06#1	008.2+06.8	L	t,*	ps(s,t)	h	0	1.93	22	...	6.94	1442	4.557	101
...	008.6-02.6	S	*	...	h	0.63	3.37	22	...	8	2908	4.557	109
010+00#1	010.1+00.7	B,o	...	ps(s)	...	0.78	46.18	...	18	1.07	6507	68.28	5
010+18#2	010.8+18.0[16]	B,o	*	...	an,sk	0.11	61.3	...	31	0.64	3000	69.671	6

Continued on Next Page. . .

Table 3 – Continued

Name PK	Name PNG	P	Cen	PS	Other	R_{exc}	Size ''	V_1 km s^{-1}	V_2 km s^{-1}	D kpc	Age yr	XBox ''	Fig#
010-01#1	010.8-01.8	E,c	*	...	an,wv,ir,h(ir)	1.02	6.82	22	...	2.31	1697	15.932	63
...	012.2+04.9[17]	R	*	...	ib	< 1	14	22	...	1.6	2413	18.228	97
015+03#1	015.9+03.3	B,c	bcr(o),*	...	ib?	0.03	7.69	22	...	2.69	2229	11.39	8
016-01#1	016.4-01.9	R	t,*	...	ib,pr	0.09	11.09	...	7	2.3	8634	19.139	95
024+03#1	024.1+03.8	B,c	bcr(i),*	...	h	0.2	9.86	22	...	4.82	5120	11.393	10
027+04#1	027.6+04.2	L,c	bcr(c)	...	pr,h(e)	0.12	2.33	22	...	1.43	359	6.828	102
038+12#1	038.2+12.0	E,c	t,*	...	h	0.03	4.60	...	10	3.58	3900	7.972	64
043+03#1	043.1+03.8[18]	E,c	*	...	wv,h(a)	0.02	3.68	11.5	...	5.87	4453	13.671	65
045-02#1	045.4-02.7	I	...	...	...	0.59	3.24	25	17.5	2.03	624	8.203	90
051+09#1	051.4+09.6	B,c	bcr(o),*	ps(s)	ib,ir,h	< 1	10.34	9.5	17	1	1441	10.025	11
...	051.5+00.2[19]	E,c	*	ps(s)	pr	< 1	9.35	...	...	...	...	20	115
051-03#1	051.9-03.8	E	bcr,*	ps(s)	ib	0.56	8.76	...	11	3.88	7327	11.393	66
056+02#1	056.0+02.0	B	w	ps(s)	an,h(e)	0.62	6.72	22	...	3.98	2880	7.791	112
057-01#1	057.9-01.5	M,c	t,*?	ps(m,t)	h	0.25	4.36	22	...	2.87	1349	6.834	38
058-10#1	058.3-10.9[20]	B,c	t?,*	...	...	0.54	7.2	21.5	14.5	2.3	1825	9.114	12
061+03#1	061.3+03.6[21]	B,c	*	ps(s,ib)	sk,ib	0.18	44.08	22	...	1	4749	48.000	113
064+05#1	064.7+05.0[22]	E,c	*	...	rr,an?,h(e,d)	0	5.27	28	23	0.95	422	22.370	67
067-00#1	067.9-00.2[23]	I	...	...	...	0.35	3.17	22	...	2.46	841	7.500	115
068-02#1	068.3-02.7	I	t ,*	...	h(i)	0	3.35	22	...	3.35	1210	6.608	91
071-02#1	071.6-02.3[24]	M,c	bcr,*	ps(m)	h	0.73	2.89	30	17	1.76	402	5.924	39
082+07#1	082.1+07.0	M,o	t	ps(m,s,ib)	ib,h	0	9.59	...	23	1.7	1680	18.224	40
082+11#1	082.5+11.3	E	...	...	h	< 1	0.82	...	13	4.76	713	6.836	68
...	093.9-00.1[25]	M,c	*	ps(m)	...	0	9.56	22	...	3	3088	12.5	116
100-08#1	100.0-08.7	M,c	bcr(o)	ps(m)	h	< 1	3.02	15.5	8	3.45	1595	8.203	42

Table 3 – Continued

Name	Name		Morphology		R_{exc}	Size	V_1	V_2	D	Age	XBox	Fig#
PK	PNG	P	Cen	PS	Other	$''$	km s^{-1}		kpc	yr	$''$	
107-13#1	107.6-13.3	E,c	*	...	wv,h(d)	< 1	9.39	...	14	8.6	13676	13.668	69
...	110.1+01.9[26]	B	w	...	an?	0	5.48	...	70	6	1112	9.000	114
111-02#1	111.8-02.8	B,o	...	...	rg,h	< 1	10.12	...	14	2.05	3504	13.671	15
130-11#1	130.3-11.7[27]	I	*?	...	...	0.73	10.43	38	39	6.1	3968	13.671	92
146+07#1	146.7+07.6[28]	B,c	t,*	ps(s)	h	0	2.77	17	7.5	7.15	2763	5.468	16
147-02#1	147.4-02.3[29]	E,c	t,*	...	ib	0.68	7.36	...	13	2.3	3087	10.025	70
165-06#1	165.5-06.5	B,c	t	...	ir,h(i)	0.7	6.82	22.5	20.5	3.45	2476	8.201	17
167-09#1	167.4-09.1	B,o	t,*	ps(an,s)	an,	0.19	5.49	30.5	16.5	6.68	2852	6.836	18
211-03#1	211.2-03.5	L,c	bcr(o),*	...	h	0.1	5.76	22	...	2.65	1644	6.836	105
215-24#1	215.2-24.2	E,c	*	ps(s)	ib,wv,pr,h	< 1	16.87	12	< 6	0.8	2666	22.785	71
226-03#1	226.4-03.7	E,c	*	ps(s)	wv,h(e,d)	< 1	11.12	22	...	...	...	15.946	72
232-04#1	232.8-04.7[30]	E,c	t,*	...	h(e,d)	0.01	2.07	22	...	1.29	286	5.97	73
235-01#1	234.9-01.4	E,c	*	...	ib,wv,h	0.67	5.72	22	...	4.53	2791	10.025	74
235-03#1	235.3-03.9	L,c	bcr,*	ps(s,bcr)	h	0.03	4.35	22	...	3.75	1758	7.291	106
258-00#1	258.1-00.3	E,c	*	ps(s)	ib,wv,pr,h	0.55	6.37	22	...	1.52	1043	9.568	75
285-02#1	285.6-02.7	M,c	t,*	ps(t)	h(i)	0.02	8.81	22	...	3.58	3392	11.393	43
296-06#1	296.4-06.9[31]	E,c	bcr?	...	ir,h	0.17	1.6	22	...	7.8	1342	6.836	76
300-02#1	300.7-02.0[32]	M,c	bcr(o),*	...	ml,h(a)	0.74	10.69	22	...	2.31	2660	13.671	44
307-04#1	307.5-04.9[33]	B,o	t,*	ps(s,an)	an,ib,wv,rg	0.26	17.6	41	10	2.4	2530	...	...
315+09#1	315.4+09.4[34]	B,o	*	ps(an)	an,ib	0.35	37.32	22	...	0.8	3217	54.67	20
315-13#1	315.1-13.0	E,c	t,*	ps(s)	pr,h	< 1	6.64	11	12	0.87	1248	13.671	77
320-09#1	320.1-09.6	M,c	*	ps(s,m)	pr,h	0	6.67	...	11	5	8757	14.582	45
321+02#1	321.3+02.8	B,c	t,*	ps(s)	ib,h	0.41	5.87	9	...	2	3093	8.203	21
321+03#1	321.0+03.9[35]	M,c	w,*	...	h	0.02	4.03	22	...	1.5	651	8.201	46

Continued on Next Page. . .

Table 3 – Continued

Name PK	Name PNG	P	Cen	PS	Other	R_{exc}	Size $''$	V_1 km s^{-1}	V_2	D kpc	Age yr	XBox $''$	Fig#
325-12#1	325.8-12.8	E,c	...	...	h	< 1	1.58	...	21.5	7.4	1287	8.203	78
326-06#1	326.0-06.5	E	*	ps(s)	h	0	1.12	...	4	8	5303	6.836	79
327-02#1	327.1-02.2	E?,c	*	ps(s)	rr,h	0.01	3.59	22	...	3.7	1430	9.114	80
331-01#1	331.7-01.0[36]	B,o	w,*	...	ib,rr	0.02	48.87	22	...	1.34	7029	66.004	22
331-02#2	331.5-02.7[37]	E,o	t,*?	...	an	0.15	20.55	22	...	3.35	7418	27.342	81
...	332.9-09.9[38]	M	*	ps(m)?	h	0	12.24	22	...	1.5	1978	13.375	114
350+04#1	350.9+04.4[39]	I,c	t,*	...	ir,h(i)	0.11	4.93	...	13	4.6	4134	11.393	93
351+04#1	351.1+04.8	E,c	*	ps(s)	ib,pr,ir	0.78	3.24	22	...	5.54	1935	5.924	82
...	351.9-01.9	B,c?	t	...	ib	0.69	5.01	22	...	8	4317	6.836	23
352+03#2	352.6+03.0	M,c	bcr,*?	ps(m)	...	0.39	3.77	22	...	5.26	2136	5.013	47
352-07#1	352.9-07.5	B,o	t	...	an,sk,ib,h(e)	< 1	10.82	22	...	2.13	2478	15.95	24
354+03#1	354.5+03.3	B,c	t	...	...	0.86	2.4	22	...	8	2068	3.646	25
355+03#3	354.9+03.5	E,o	*?	...	...	0.13	5.87	22	...	8	5061	8.203	83
355-02#1	355.4-02.4[40]	B,o?	bcr(o)?	...	...	0.91	9.89	22	...	3.48	3706	12.76	26
355+03#2	355.9+03.6	E	...	ps(s)	h	0.29	0.66	...	40	4.36	170	2.279	84
355-03#3	356.5-03.9	B,c	bcr(o)	...	h	0.79	4.59	22	...	2.61	1289	6.836	27
355-04#2	355.9-04.2[41]	M,c	t,*	ps(m)	h(a)	0.25	4.73	22	...	3	1530	7.291	48
356-03#2	356.5-03.6[42]	B	t?	ps(s)	...	0.56	12.9	22	...	8	11119	14.127	28
356+03#1	356.8+03.3	S	t	...	h(i)	0.04	1.34	22	...	8	1156	4.557	111
356-03#3	356.5-03.9	L	bcr(c),*	ps(s,bcr)	ib?,h	0.02	5.21	22	...	7.53	4226	6.836	107
357-04#3	357.1-04.7	B	t,*	ps(s)	...	0	2.63	22	...	13.2	3739	4.557	29
357+02#6	357.2+02.0	R	...	...	h	1.04	2.67	22	...	8	2304	6.836	96
358-04#1	358.5-04.2	M,c	t	ps(m,an,s)	an,ml	0.6	8	22	...	3.92	3375	9.114	49
358+05#2	358.7+05.2[43]	E?	bcr(o),*	ps(s)	...	0	3.22	22	...	5.51	1910	4.557	85

Continued on Next Page. . .

Table 3 – Continued

Name	Name			Morphology		R_{exc}	Size	V_1	V_2	D	Age	XBox	Fig#
PK	PNG	P	Cen	PS	Other		″	km s^{-1}		kpc	yr	″	
358+03#4	358.9+03.4	M,c	t	ps(m)	...	0.22	3.21	22	...	4.9	1693	4.557	50
358-00#2	358.9-00.7[44]	M,c	bcr(c),*	...	ir,h(i)	0.07	5.13	5.5	13.5	1.51	3325	13.671	51
359+04#1	359.2+04.7[45]	E,c	*	...	...	0	1.81	22	...	5	974	3.646	86
Objects	with	$R_{exc} > 1$											
002-03#2	002.3-03.4	B	t	...	...	1.45	4.43	22	...	3.63	1731	6.836	2
002-03#6	002.9-03.9[46]	S	*	...	...	2	4.47	22	...	8	3852	9.114	108
003+05#1	003.8+05.3[47]	I	...	...	...	1.16	3.91	22	...	6.93	2920	6.38	87
003+02#1	003.1+02.9	M,c	bcr(i),*	ps(m,an)	an	1.14	30.05	...	23	2.15	6658	31.899	33
...	004.1-03.8[48]	E	t?	...	...	1.31	2.67	22	...	8	2304	4.557	56
004-22#1	004.8-22.7	E	...	...	h	1.87	0.61	22	...	4.76	314	2.279	57
...	005.2-18.6[49]	E,o	t	ps(t)	...	2.73	3.02	22	...	24.8	8078	3.646	59
...	006.8-19.8	E	...	ps(s)	...	3.64	1.62	22	...	24.8	4332	4.101	61
006+04#1	006.3+04.4	L,c	bcr,*	...	ir,h	1.91	5.13	22	...	5.8	3201	6.836	99
008-07#2	008.3-07.3[50]	M,c	bcr?,*	...	ib,h	4.0	7.72	22	...	2.67	2217	11.39	35
010-06#1	010.7-06.4[51]	I	*	ps(s)	h	2.9	2.04	22	...	4.9	1076	4.101	89
013+04#1	013.1+04.1[52]	B?,c	bcr?,*	ps(s)	h	1.13	5.29	...	12.5	3.41	1944	8.194	7
019-05#1	019.4-05.3	M,c	bcr,*	ps(s)	ml,ib,h	1.41	5.72	22	...	2.37	1460	8.203	36
023-02#1	023.9-02.3	B,c	bcr,*	...	ml,h	1.34	17.89	...	13	1.23	3996	21.874	9
027-09#1	027.6-09.6[53]	M,c	bcr(i),*	ps(m,an)	an,ib?,h(i)	2.8	9.36	...	13.1	6.5	6558	11.393	37
032+07#2	032.1+07.0	S	*	...	...	1.99	4.67	22	...	5.71	2871	5.468	110
032-02#1	032.7-02.0	L	bcr(o)	ps(ib)	an,ib,h(i)	2.01	7.13	22	...	3.44	2644	9.114	103
037-06#1	037.8-06.3	L,c	bcr(c)	...	ib,h	2.34	4.98	...	15	1.54	1213	7.291	104
060-07#2	060.1-07.7[54]	B,c	bcr(o,i),*	...	wv,h	3.9	11.12	25.5	20	1.7	1757	13.671	13
074+02#1	074.5+02.1	B,o	t	ps(s,t)	rg	1.88	17.09	...	16.5	3.2	7856	30.988	14

Continued on Next Page. . .

Table 3 – Continued

Name PK	Name PNG	P	Cen	Morphology PS	Other	R_{exc} $''$	Size $''$	V_1 km s^{-1}	V_2	D kpc	Age yr	XBox $''$	Fig#
089-05#1	089.8-05.1	M,c	bcr(c)	ps(m)	h(e,a)	3.8	4.16	21.5	16.5	2.1	964	9.114	41
304-04#1	304.5-04.8	B,c	bcr(o,i)?	ps(s)	an,ml,ir	4.5	19.59	...	12	2.1	8124	33.266	19
356+04#2	356.9+04.4	B	...	ps(an,s)	an	1.56	5.65	22	...	4.73	2878	6.836	30

1 2 3 4 5 6 7 8 9 10 11 12 13 14 15 16 17 18 19 20 21 22 23 24 25 26 27 28 29 30 31 32 33 34 35 36 37 38 39 40 41 42 43 44 45

---

[1]Col. 1: Object name in PK format

[2]Col. 2: Object name in PNG format

[3]Cols. 3,4,5,6: morphological classification, divided into 4 parts: (i) the primary classification and the secondary descriptor related to whether the lobes (or the shell in the case of an E primary classification) are open or closed, (ii) the secondary descriptors for the central region, (iii) the secondary descriptors describing point-symmetry, and (iv) all remaining secondary descriptors

[4]Col. 7: the [OIII]λ5007/Hα line flux ratio

[5]Col. 8: The angular size of the object in arcseconds

[6]Col. 9: The expansion velocity measured from the [NII]λ6583 as listed in the Acker et al. catalog

[7]Col. 10: The expansion velocity measured from the [OIII] line as listed in the Acker et al. catalog

[8]Col. 11: The distance to the object

[9]Col. 12: The derived expansion age

[10]Col. 13: The size of the panel (along the horizontal axis) in the figure of the object

[11]Col. 14: The number of the figure showing the object

[12]PNG001.7−04.4: *bcr* since major/minor axis ratio of central region not consistent with tilted torus

[13]PNG003.6+03.1, PNG003.9−03.1, PNG008.6−02.6, PNG326.0−06.5, PNG351.9−01.9, PNG354.5+03.3, PNG354.9+03.5, PNG356.5−03.6, PNG356.8+03.3, PNG002.9-03.9 and PNG004.1−03.8 are Galactic Bulge PNs, and their distance is taken to be 8 kpc

[14]PNG004.0−03.0: note the jet emanating at $pa \sim 30°$, a structure not covered in our morphological scheme. Making the assumption that the jet is launched roughly orthogonally to the waist of the nebula, the bright elliptical ring is identified as a tilted, toroidal waist (*t* descriptor) with its major axis along $pa \sim -55°$

[15]PNG004.9+04.9: the halo has an inner irregularly-shaped brighter component, with a discernible periphery, and an outer, more typical diffuse component with a surface-brightness limited size

[16]PNG010.8+18.0: the distance has been taken from Schwarz et al. (1997)

[17]PNG012.2+04.9: distance taken from Preite-Martinez (1988), and R_{exc} estimated from spectrum in Suárez et al. (2006); object is listed as IRAS 17514-1555 in these studies

[18]PNG043.1+03.8: the *h(a)* descriptor is used to denote the presence of the faint, somewhat irregular, but complete ring in the halo, which surrounds the central bright nebula

[19]PNG051.5+00.2: R_{exc} estimated from spectrum in Kerber et al. (1996); no distance estimate available, hence no estimate of age possible. Note that finding chart in Kerber et al. (1996) incorrectly points to a star 11.5" west of the PN, and the coordinates given in Table 1 are incorrect. The J2000 SIMBAD coordinates of this source, RA=19h25m40.68s +16d33m05.6s, however, are consistent with the coordinates derived for the central star, from the HST image, RA=19h25m40.48s +16d33m05.4s

---

[20]PNG058.3−10.9: the bipolar lobes can be seen very faintly along $pa \sim 25°$; the t denotes the bright region with its major axis orthogonal to the lobe axis

[21]PNG061.3+03.6: the distance has been taken from Dobrinčić et al.(2008)

[22]PNG064.7+05.0: the [OIII]/Hα ratio is much less than unity; since the Hα line is saturated in Acker et al, we have set the ratio to 0

[23]PNG067.9−00.2: the object may be bipolar (with lobes aligned along $pa \sim 90°$), with an obscuring waist and irregular structure, i.e., B,w,ir; however we have conservatively chosen I as the primary classification for this object

[24]PNG071.6-02.3: the elongated structure at $pa \sim 60°$ is considered to be a second lobe pair, leading to its primary classification of M

[25]PNG093.9-00.1: the [OIII]/Hα ratio is much smaller than unity, based on spectroscopic data described in Sanchez Contreras et al. 2008; distance is taken from Meixner et al. (1997)

[26]PNG110.1+01.9: the [OIII]/Hα ratio has been set to zero based on the non-detection of [OIII]λ5007 by Garcia Lario et al. (1991), and the distance has been taken from the same reference

[27]PK130−11#1: we use "*?", since given the diffuse, irregular shape of this object, and the presence of additional stars in the vicinity, we cannot be certain that the star near the center of this object is really the CSPN

[28]PNG146.7+07.6: because of the apparent large tilt of the nebular axis towards the line-of-sight, the lobes may also be open structures

[29]PNG147.4−02.3: the primary PN shape is assumed to be defined by the outer periphery in this image; the inner bright structure is an inner bubble (i.e., ib)

[30]PNG232.8−04.7: the halo has an inner irregularly-shaped brighter component, with a discernible periphery, and an outer, more typical diffuse component with a surface-brightness limited size

[31]PNG296.4−06.9: the central region is described as "bcr?" because its extent and structure are not well resolved

[32]PNG300.7−02.0: this object shows a dusty structure which produces obscuration as it cuts across the lower lobes, which is not captured in our primary and secondary descriptors

[33]PNG307.5−04.9: we have adopted values of the size and distance for this object (also known as MyCNn 18), from Sahai et al. (1999). The radially-varying [NII] expansion velocity, V_1, is estimated from eqn. (4) of Dayal et al. (2000) using a radius R set to half the size of the object. A ground-based image (Bryce et al. 1997) shows distant ansae on both sides of the center

[34]PNG315.4+09.4: distance from Schwarz, Aspin & Lutz (1989), note that the long-slit spectra in Corradi & Schwarz (1993) suggest much higher expansion velocities ($\gtrsim 100\,\mathrm{km\,s^{-1}}$), who derive a smaller expansion age, $\lesssim 920\,\mathrm{yr}$

[35]PNG321.0+03.9: distance from Sahai et al. (2000b)

[36]PNG331.07−01.0: the w descriptor is used to denote the belt of obscuration (oriented along the minor axis of the object) that cuts across the inner regions of the bright bipolar lobes

[37]PNG331.5−02.7: we use "*?", since the "central" star is noticeably offset from the geometric center of the toroidal waist,

and since there are many additional stars visible in its vicinity, we cannot be sure that this star is really the CSPN

[38]PNG332.9−09.9: the [OIII]/Hα ratio has been set to zero based on the non-detection of [OIII]λ5007 by De Marco & Crowther (1998), and the distance has been taken from the same reference. The object most likely possesses point-symmetry by virtue of having at least two pairs of diametrically-opposed lobes, but we assign it "$ps(ml)$?" because the $pa = 180°$ counterpart of the $pa = 0°, 180°$ is only partially visible

[39]PNG350.9+04.4: the t descriptor is used to describe bright inner ring structure, which is most likely a torus seen nearly face-on

[40]PNG355.4−02.4: we assign "$bcr(o)$?" to the central region, because although its extensions along the polar direction cannot be separated unambiguously from the low-latitude regions of the bipolar lobes

[41]PK355−04#2: the lobe at $pa \sim 0°$ has a complex, "layered" periphery, with 3 layers

[42]PNG356.5−03.6: we desribe the central region as "t?" because it appears to be somewhat less extended along the polar axis than along the equatorial plane; however its structure makes this assessment a bit uncertain

[43]PNG358.7+05.2: We have assigned this "E?", but, like PNG013.1+04.1, it may be a bipolar object with its major axis oriented at a small angle to the line-of-sight, since a slight "pinching-in" of the primary shape can be seen along $pa \sim 55 \deg$

[44]PNG358.9−00.7: the central region is described as $bcr(c)$, even though its shape is almost spherical, not barrel-like; the plethora of protrusions emanating from the main nebula body represent structures not covered in our morphological scheme

[45]PNG359.2+04.7: distance from Gesicki and Zijlstra (2007)

46 47 48 49 50 51 52 53 54

---

[46]PNG002.9−03.9: since there are two stars near the center, we speculate that these may represent a binary CSPN responsible for the spiral structure

[47]PNG003.8+05.3: although classified as I, faint nebulosity can be seen extending along $pa \sim 170°$ and possibly $pa \sim -15°$, suggesting that this may be really a B or L object with very faint lobes

[48]PNG004.1−03.8: the curved bright structure seen near the waist may represent a partial torus structure

[49]PNG005.2−18.6 & PNG006.8-19.8: based on their radial velocities, these PNs are believed to belong to the Sagittarius dwarf spheroidal galaxy (Zijlstra et al 2006) at a distance of 24.8 kpc (Kunder & Chaboyer 2009)

[50]PNG008.3−07.3: this object is clasified as multipolar (M) because it has two pairs of lobes at slightly different orients (in projection), i.e., at $pa \sim 5°$, $17°$. We assign "*bcr*?" to the central region because the structure seen there could result from a pair of lobes projected almost directly towards the line-of-sight

[51]PNG010.7-06.4: inspite of its primary classification as I, there are two parallel, almost linear features on the left and right sides of the central star which motivate including the ps(s) descriptor

[52]PNG013.1+04.1: we have assigned this "B?", because it is quite possibly a bipolar object with its major axis oriented at a small angle to the line-of-sight. For the same reason, although the central region appears extended along the major axis, it is difficult to assess this extent, hence we use "*bcr*?" to describe this region

[53]PNG027.6−09.6: we assign the secondary descriptor "*ib*?" to this PN because although there appears to be an elliptical shaped structure in the center, the additional structure within the central region makes its identification somewhat ambiguous

[54]PNG060.1−07.7: the central star and round halo are seen clearly in the F555W image, and are therefore included in the morphological classification

Table 4:: Statistics

Classification	Number[1]	Fraction[1]	Number[2]	Fraction[2]
	$\mathbf{R}_{exc} \leq 1$		All Objects	
B	27	0.28	33	0.28
M	18	0.19	23	0.20
E	32	0.34	37	0.31
I	6	0.063	8	0.068
R	4	0.042	4	0.034
L	7	0.074	10	0.085
S	2	0.021	4	0.034
Point Symmetry				
B, ps[3]	12	0.44	14	0.45
M, ps[4]	15	0.83	19	0.83
E, ps[5]	13	0.41	15	0.42
ps[4]	42	0.44	53	0.45

1 2 3 4 5 6

[1]Number of objects in given class, and as a fraction of the total (96) for which the [OIII]λ5007/Hα flux ratio, $R_{exc} \leq 1$,

[2]Number of all objects in given class, and as a fraction of the total sample (119)

[3]Number of point-symmetric objects in class B, and as a fraction of the total in class B

[4]Number of point-symmetric objects in class M, and as a fraction of the total in class M

[5]Number of point-symmetric objects in class E, and as a fraction of the total in class E

[6]Total number and fraction of point-symmetric objects, including objects of the S primary class, which is point-symmetric by definition

Table 5:: Morphological Classification for PNs from HST program GO 11657

Name			Morphology		R_{exc}	Fig#
PNG	Prim	Cen	PS	Other		
Objects	with	R_{exc}	≤ 1			
014.3-05.5	E,c	bcr(c),*	...	h	0	...
059.9+02.0	B,c	t,*	...	h	0	...
063.8-03.3	E,c	t?,*	...	h	0	...
079.9+06.4	R	*	...	h	0.68	...
098.2+04.9	E,c	*	...	h	0.88	...
104.1+01.0	E,c	*	...	h	0.57	...
107.4-02.6	E,c	*	...	h	0.72	...
294.9-04.3	E,c	*	...	h	0.16	...
309.0+00.8	B	bcr(i),*	...	h(e)	0.86	...
324.8-01.1	E,c	*	ps(s)?	ib,ml,h	0.37	...
327.1-01.8	E,c	*	...	pr,h	0.036	...
334.8-07.4	M,c	*	ps(m)	h?	0.36	134
344.2+04.7[1]	B,c	t,*	...	h	0.59	135
344.8+03.4	S	t,*	...	...	0.22	136
356.5+01.5	E	t,*	ps(s)	ib,h(d)	0.18	123
184.0-02.1	E,c	*	...	pr,h	< 1	...
Objects	with	R_{exc}	> 1			
000.8-07.6	B,o	t,*	...	h(i)	2.6	...
014.0-05.5	B,c	bcr(c),*	...	h(d)	1.5	124
021.1-05.9	B,c	bcr(i),*	...	h?	3.1	125
025.3-04.6	E	bcr(o),*	ps(an,bcr)	an,h	3.2	...
026.5-03.0	B,c	*	ps(s)	h(d)	1.4	...
042.9-06.9	L	t,*	...	ir,h	3.0	...
048.5+04.2[2]	B	t,*	ps(t)	h(e,d)?	1.3	126
052.9-02.7	E,c	*	ps(s)	h	2.1	...
053.3+24.0[3]	B,c	t,*	ps(s,t,ib)	ib,h(e)	3.4	127
068.7+14.8	R	*	...	h	1.2	...
068.7+01.9[4]	E	t,*	...	ib,h(a?)	1.2	...
097.6-02.4	E	t,*	ps(s)	...	2.1	128
205.8-26.7	R	*	...	ib,h	4.0	...
263.0-05.5	E,c	*	...	ib,h	2.3	...

Continued on Next Page. . .

Table 5 – Continued

Name			Morphology		R_{exc}	Fig#
PNG	Prim	Cen	PS	Other		
264.4-12.7	R	*	...	h	1.7	129
275.3-04.7	E,c	*	...	h(d)	2.5	...
278.6-06.7	E,c	*	ps(ib)	ib,h	1.1	130
285.4+02.2	I	*	...	h(i)	2.4	...
285.4+01.5[5]	B,c	bcr	ps(s)	ml,h(a?)	1.1	131
286.0-06.5	B,o	t,*	ps(s)	rg,h	2.1	132
289.8+07.7	R	*	...	h	3.1	...
295.3-09.3	B	bcr,*	...	h	2.4	...
296.3-03.0	B,c	bcr(o)	ps(s,ib)	ib,h	2.3	...
309.5-02.9[6]	L	t,*	...	ib,h	1.2	133
336.9+08.3	E,c	*	...	h(e,d)	1.2	...
340.9-04.6	E	*	...	ib,h	1.5	...
343.4+11.9[7]	E	*	...	h	3.7	...
348.4-04.1	B,o	t,*	...	h	1.5	137
348.8-09.0	R	*	...	ib,h	1.2	138
351.3+07.6	E	*	ps(s)	h	1.3	...
358.6+07.8	E	*	...	h(d)	1.4	...

1 2 3 4 5 6 7

---

[1]PNG344.2+04.7: Although we assign B as the primary class, this object may be intrinsically multipolar (M), with the inner bright lobe pair component having its axis projected along the axis of the larger, faint primary lobe pair

[2]PNG048.5+04.2: The axis of the bipolar lobes, which are apparently inclined at a relatively small inclination to the line-of-sight, is oriented at $pa \sim 50°$. An elongated diffuse nebulosos structure can be seen with its major axis at $pa \sim 140°$, but gives its rather limited radial extent, we tentatively classify it as a halo, i.e., as h(e,d)?

[3]PNG053.3+24.0: The "t" descriptor refers to the bright structure oriented with its long axis along $pa \sim -20°$; however, it is possible that this structure is actually a lobe structure, similar to that seen in the multipolar PPN, IRAS19475+3119 (Sahai et al. 2007b), suggesting the alternative classification M,c,*,ib,ps(m,ib),h(e)

[4]PNG068.7+01.9: We use "a?" for the qualifier in the halo descriptor, since only a single, partial arc-like feature is seen

[5]PNG285.4+01.5: We assign the feature at $pa \sim -50°$ the minor lobe descriptor ml, but it is possible that this is a planar structure whose radial density distribution has a sharp outer edge, in which case it would be better described by the $w(b)$ descriptor used for PPNs (SMSC07). We use "a?" for the qualifier in the halo descriptor, since only a single, partial arc-like feature is seen

[6]PNG309.5-02.9: We assign this a primary class L; the collimated lobes are seen weakly at $pa \sim 70°$. The bright structure surrounding the central star is an inner bubble, and the torus is the ring-like structure which is brightest on the right side of the central star in the image

[7]PNG343.4+11.9: A well-defined nebular shell is not seen in this object; we assume that the inner bright region oriented at $pa \sim -15°$ represents the primary nebula, and the surrouding diffuse structure is the halo